Optical Properties of Metal Nanostructures as Probed by Photosensitive Molecules

Claire Deeb

A Dissertation

presented to the University of Technology of Troyes

by

Claire Deeb

In Partial Fulfillment of the Requirements for the Degree

Doctor of Philosophy in Physics

Discipline: Optics and Nanotechnology

Optical Properties of Metal Nanostructures as Probed by Photosensitive Molecules

---

08 October 2010

Approved by

Dr. Fabrice Charra
Researcher HDR and Group Leader at CEA Saclay

Dr. Gérard Colas Des Francs
CNRS Researcher HDR at the University of Burgundy

Dr. Nordin Felidj
Professor at University of Paris 7

Dr. Loic Mager
CNRS Researcher at the Département d'Optique Ultrarapide et de Nanophotonique

Dr. Jérôme Plain
Associate Professor HDR at the Laboratory of Nanotechnology and Optical Instrumentation ICD-LNIO

Dr. Renaud Bachelot
Professor at the Laboratory of Nanotechnology and Optical Instrumentation ICD-LNIO (Supervisor)

Dr. Gary Wiederrecht
Chemist and Group leader at ANL Chicago

Acknowledgement

This thesis arose in part out of years of research that has been done since I came to Bachelot's group. By that time, I have worked with a great number of people whose contribution in assorted ways to the research and the making of the thesis deserved special mention. It is a pleasure to convey my gratitude to them all in my humble acknowledgment.

In the first place I would like to record my gratitude to Renaud Bachelot for his supervision, advice, and guidance from the very early stage of this research, as well as giving me extraordinary experiences through out the work. Above all and the most needed, he provided me unflinching encouragement and support in various ways. His truly scientist intuition has made him as a constant oasis of ideas and passions in science, which exceptionally inspire and enrich my growth as a student, a researcher and a scientist want to be. I am indebted to him more than he knows.

I gratefully thank Dr. Gérard Colas des Francs and Dr. Fabrice Charra for their constructive comments on this thesis. I am deeply thankful that in the midst of all their activity, they accepted to be members of the reading committee. I would like to thank the rest of my thesis committee: Prof. Nordin Felidj, Dr. Loic Mager, Dr. Jérôme Plain, and Dr. Gary Wiederrecht, for their encouragement, insightful comments, and questions.

I gratefully acknowledge Pascal Royer who accepted me to be a member of his lab. It is also a pleasure to pay tribute to the collaborators. To Alexandre

Bouhelier, Libai Huang, Prashant K. Jain and Olivier Soppera, I would like to gratefully acknowledge you.. Your involvement with its originality has triggered and nourished my intellectual maturity that I will benefit from, for a long time to come. Your participation in "Photohybrid" was the backbone of the project and so to this thesis. I am grateful in every possible way and hope to keep up our contact in the future. To Lavinia Balan, Anne-Laure Baudrion, Davy Gérard, Safi Jradi, Daniel Lougnot, Jérôme Plain, Carole Ecoffet, thanks for all of you for the fruitful discussions we had.
I would also acknowledge the exceptionally experienced Veeco team..To Emmanuel Paris, Mickaël Febvre, Rafaël Barbattini and Yann Gilbert, thank you for the advice and the willingness you had to share your bright thoughts with me, which were very constructive during the AFM and SNOM sessions.

To the role model for hard workers in the lab, Régis Deturche and Sergei Kostcheev, I would like to thank you both for the sessions of electron beam lithography and metal evaporation. It is really a pleasure to work with persons like you who are always ready to lend a hand.
Collective and individual acknowledgments are also owed to my colleagues at LNIO whose present somehow perpetually refreshed, helpful, and memorable. Many thanks go in particular to Antoine, Christophe, Hélène, Hicham, Jérôme M., Julien, Grégory, Mathieu, Merlin, Mohamed, Montacer, Pascale, Thomas, Xuan, Zohreh for giving me such a pleasant time when working and discussing science together with them.

Where would I be without my family? My parents deserve special mention for their inseparable support and prayers. My Father, Khalil, in the first place is the person who put the fundament "my learning character", showing me the joy of intellectual pursuit ever since I was a child. My Mother, Fakhrié, is the one who sincerely raised me with her caring and gently love. Zaher, Ghazal, and little one Sahar, thanks for being supportive and caring siblings.
Words fail me to express my appreciation to my second half, Rida, whose dedication, love and persistent confidence in me, has taken the load off my shoulder. I owe him for being unselfishly let his intelligence, passions, and ambitions collide with mine.
I am extraordinarily fortunate in having mates in my life..Though they are few, yet they are too precious to me..To Ali, Fatima, Jad and Prash. I could never have embarked and started all of this without your prayers. Thank you.

Finally, I would like to thank everybody who was important to the successful realization of thesis, as well as expressing my apology that I could not mention personally one by one.

Contents

List of Figures

Nomenclature

2-D	two-dimensional
AFM	atomic force microscopy
Ag	silver
Ag NPs	silver nanoparticles
Al	aluminum
ANR	Agence Nationale de la Recherche
Ar:Kr	argon:krypton
DDA	discrete dipole approximation method
DNA	deoxyribonucleic acid
EBL	electron beam lithography
EELS	electron energy loss spectroscopy
EGFR	epidermal growth factor receptor
Eosine-Y	2',4',5',7'-tetrabromofluorescein disodium salt
FDTD	finite-difference time-domain
FTIR	fourier transform infrared spectroscopy

FWHM	full-width at half-maximum
IPA	isopropanol
LNP	lithographic nanoparticles
LSP	localized surface plasmon
LSPR	localized surface plasmon resonance
MDEA	methyldiethanolamine
MIBK	methyl isobutyl ketone
NA	numerical aperture
NP	nanoparticle
NPGS	nanometer pattern generation system
PEEM	photo-emission electron microscopy
PETIA	pentaerythritol triacrylate
PMMA	polymethyl methacrylate
SEM	scanning electron microscope
SNOM	scanning near-field microscopy
SPR	surface plasmon resonance

DRIVEN by the search for new materials with interesting and unique properties and also by the study of the accompanying changes in the physical chemistry of nanoscale material compared with the bulk or to individual atoms, the field of nanoparticle research has grown immensely in the last two decades.
From a technological standpoint, the reason for studying nanostructured materials is mainly the anticipated applications in optical systems and catalysis. In particular, in the fields of optical data communication and optical data storage, the need for new materials with high nonlinearities is driving nanoparticle research. The ease of tuning the optical properties gradually with particle size and shape have made nanoparticles very interesting compared with organic dye molecules.

Semiconductor nanoparticles have already been successfully used in solar cells converting sunlight into electricity. Moreover, currently used optical probes, including markers attached to antibodies, provide precise information about the presence of specific molecules. Quantum dots are widely used and studied for this application due to their unique size-dependent fluorescence properties. However, potential human toxicity and cytotoxicity of the semiconductor material are two major problems for its in vitro and in vivo application. Colloidal gold nanoparticles have become an alternative consideration due to their ease of preparation, ready bio-conjugation, and potential non-cytotoxicity. Immuno-gold nanoparticles conjugated to antibodies have provided excellent detection qualities for cellular labeling using electron microscopy.

Compared with other nanostructures, metallic nanoparticles have proven to be the most flexible nanocrystals owing to the synthetic control of their size, shape, composition, structure, assembly and encapsulation, as well as the resulting tunability of their optical properties. On that account, the tunable photophysical attributes of metal nanocrystals, their efficient addressability via optical and spectroscopic techniques, and rapid advances in nanoparticle synthesis and fabrication have brought these nanostructures to the forefront of nanotechnology research directed toward applications ranging from photonics to biomedicine.

The unique optical attributes of noble metal nanoparticles can be elucidated as follows. When matter is exposed to light, a number of processes can occur:

- The light can be scattered at the same frequency as the incoming one (Mie

or Rayleigh Scattering).
- The light can be absorbed.
- The absorbed light can be re-emitted (i.e, fluorescence).
- The local electromagnetic field of the incoming light can be enhanced, thus enhancing any spectroscopic signal from the molecules at the material surface, that is, surface-enhanced spectroscopy, such as surface-enhanced Raman scattering.

In the case of noble metal nanoparticles, all these processes are strongly enhanced owing to the unique interaction of light with the free conduction-band electrons in the metal particles. This implies that when noble metal nanoparticles are exposed to light radiation, the electric field of the light causes the collective oscillation of the conduction-band electrons at the surface of the particle, with respect to the ionic core of the nanoparticle. The coherent oscillation of the metal free electrons in resonance with the electromagnetic field is called the surface plasmon resonance. The excitation of the surface plasmon resonance results in the enhancement of the photophysical properties of metal nanoparticles.

So far, several functional structures taking advantage from the unique peculiarities of localized surface plasmons have been designed. Furthermore, hybrid structures consisting of metal nanoparticles and other systems such as fluorescent molecules, photosensitive molecules, quantum dots, liquid crystal molecules, have been also developed. These types of structures are of great interest since they combine the respective attributes of the constituent components, as well as manifest unique properties arising from the mutual coupling between the components.

While past research has considered the interaction between metal nanoparticles and photosensitive molecules, especially the possibility of initiating nanoscale photopolymerization based on the localized surface plasmons of such particles, this thesis describes the in-depth characterization and optimization of such interactions that result in nanoscale photopolymerization, and further demonstrates the ability to use the nanophotopolymerization process to *quantitatively* map with unprecedented resolution (better than 5 nm) both, the near-field of metallic nanoparticles associated with their localized surface plasmons, and the local electric fields resulting from surface charge densities at metal/dielectric interfaces.

Furthermore, this work will prove that the nanoscale photopolymerization approach does not only map the near-field of metal nanoparticles, yet it constitutes, from a more fundamental point of view, a unique opportunity to investigate

nanophotochemistry.

The first Chapter of this PhD dissertation will describe the optical characteristics of noble metal nanostructures. A special accentuation is placed on the tunability of such properties by change in the size, shape, composition, and environment of the nanoparticle. An overview on the hybridization achieved worldwide by other groups will be narrated, then the expertise of our group in structuring hybrid nanosystems, made of metal nanoparticles and polymer lobes, will be detailed. As it will be shown along this Chapter, our approach will serve as a technique to better understand the near-field response of metal nanoparticles and their field distribution, and it will be compared to the main approaches used to characterize the metal structures and their optical response.

In Chapter two, we present the methods utilized along this thesis, including the developments and the innovations brought by this work. The aim of this Chapter is to familiarize us with the several types of metal nanostructures and photosensitive systems. In its first part, the elaboration of different types of noble metal nanoparticles and the multiple ways used to characterize them will be discussed. Additionally, the influence of different parameters on the position of the plasmon resonance is detailed. The preparation and the photopolymerizable mechanism of different photosensitive solutions will be discussed in the second part of the Chapter. Moreover, the characterization of the different types of molecular systems, using an interferometric and a focalized laser spot experimental setups, is realized.

The accomplished results are presented in Chapters three, four and five.

In Chapter three, we start by showing our preliminary results performed on lithographic nanoparticles in presence of photopolymerizable solutions. Then, we report our used approach for imaging and quantifying both the depth and the strength of the optical near-field, of a single colloidal metal nanoparticle, associated with localized surface plasmons. We will emphasize that our technique relies on a nanoscale molecular molding of the confined electromagnetic field of metal colloids, irradiated at their resonance, by a photo-activated polymer, which enabled us to directly image the dipolar profile of the near-field distribution with an unprecedented resolution, better than 10 nm. We were also able to quantify the near-field depth and its enhancement factor. Moreover, and by means of our

approach, we show our capability to realize a near-field spectrum corresponding to the response of localized surface plasmons of a single metal nanoparticle.

In Chapter four, we report on the direct imaging of the non-resonant field on a metal/dielectric interface on a gold nanorod. By means of the same approach detailed in Chapter three, we embody the profile of non-vanishing components of the electric field held at the interface gold metal/photopolymerizable solution, where the gold nanoparticles were irradiated off-resonance. By means of the surface charge densities which are proportional to the discontinuity of the normal components of the electric field at the interface metal/dielectric, we demonstrated that the effective dose at some precise positions overcome the threshold dose of the solution, and hence polymerization process is initiated. Finally, we demonstrate that the sensitivity of the photopolymer is high enough to imprint the non-resonant field with nanoscale resolution, thus allowing a direct visualization of the surface charge density distribution with a 2-nm resolution.

In the last Chapter of this work, we will take a nanometric look at the photochemical system. In particular, we will study its behavior as a function of the diffusion of the constituent reactive species, namely dye and oxygen, in response to different irradiation parameters. Indeed, we will show results demonstrating that our near-field photopolymerization approach will serve as a tool to understand some events that are only valid at the nanoscale. In this regard, we have determined the physico-chemical parameters and phenomena controlling the spatial extend of the photopolymerization process. We will surprisingly perceive that the dye diffusion plays a crucial role at the nanometer scale, as opposed to previous studies at the micrometer level where its role was fairly neglected.

A conclusion will end up this dissertation where future outlooks and some perspectives will be discussed.

Chapter One

Plasmonics and Hybridization

1.1 Introduction

Noble metal nanoparticles have attracted considerable attention since historical times for their unique and optical properties that are distinct from metallic clusters or metals at the bulk scale, and characteristic of the intermediate size regime of the particles. [1, 2] The decorative pigments in some historical artworks like the Roman Lycurgus cup [3] from the 4th century are now known to be composed of tiny amount of colloidal gold, silver, copper and their alloys, which give them these unusual optical properties. This extraordinary cup is the perfect example of a very special type of glass, known as dichroic, which changes color when held up to the light. The opaque green cup turns to a glowing translucent red when light is shone through it. As it can be noticed, colloidal gold has been used as a coloring pigment dating back to the middle ages; Nevertheless it took the scientists longer time to analyze and understand the characteristics of these colloids. After the work of Faraday, the interest in noble metals has evolved from artistic and empirical to scientific and technological.

Around the turn of the twentieth century, the field of the nanotechnology has undergone tremendous growth due to the pioneering contributions from Mie, Faraday and many others. The one thing that all these pioneers had in common was the fact that they realized how dramatically the ratio of surface atoms to interior atoms changes if one successively divides a macroscopic object (a cube for example) into smaller parts. The study of the accompanying changes in the physical chemistry of nanoscale material compared with the bulk or even to individual atoms was their goal then, as it still is today.
As an example of how drastically the number of surface atoms increases when we decrease the particle size, let us consider the case of an iron cube of 1-cm of edge.

The percentage of surface atoms would be only 10^{-5}%. [4] Dividing the same cube into smaller cubes with an edge of 10 nm results in a percentage of surface atoms of 10%; Moreover, in a cube of 1-nm edge, every atom will be a surface atom. This might illustrate why changes in the size range of a few nanometers are expected to lead to great changes in the nanoparticle physical and chemical properties.

Unique optical attributes of noble metal particles are due to their plasmon resonance, which is the collective coherent oscillation of the nanoparticle free electrons. Recent studies seek to identify the characteristics of these nanoparticles, [2, 5, 6] contributing to the basic science in a manner that creates the ability to use nanoparticles for many applications including energy, [7] nanoscale trapping, [8] light generation, [9] nanosensing, [10] and data storage, [11, 12]. So far an important number of plasmon-based nanostructures have been developed. But it turns out that hybrid plasmonics, meaning metal/other material hybrid systems, including dielectric/metal nanoshell configuration, [13] electrically addressable active plasmonic structures, [14] molecular/plasmonic systems, [15, 16] and semiconductor/metal structures, [17, 18] are likely to constitute the most promising solution because they can take advantage of the respective properties of the different components and benefit from their mutual coupling.

In this chapter, we introduce the status of scientific understanding of the optical properties of noble metal nanostructures. We place especial emphasis on the localized surface plasmons and the applicable ways used to get them excited. This is followed by an overview on the hybridization of metal nanostructures which has been realized by other groups, then we will present the recent expertise of the laboratory of Nanotechnology and Optical Instrumentation (LNIO), which consists on structuring metal/polymer hybrid nanoparticles, [19, 20] and we will detail our approach. The last section of this chapter discusses the three main approaches that are used for characterizing plasmonic structures and their limitations. We will end up this chapter by setting the motivation for the work described in this thesis.

1.2 Optical radiative properties of noble metallic nanoparticles: Surface Plasmon Resonance

1.2.1 The Mie Theory

It has been shown by Gustave Mie in 1908 that the optical properties of noble metal nanoparticles depend strongly on divers parameters [21] , namely the size, the metal nature, the shape, and the surrounding medium of the metal nanoparticle. Mie has solved Maxwell's electrodynamic equations for an electromagnetic light wave interacting with small spheres having the same macroscopic frequency-dependent dielectric constant as the bulk metal. The solution of this calculation with appropriate boundary conditions for a spherical object leads to an electromagnetic waves having different orders, ranging from the lowest dipolar order to the higher order multipoles, depending on the size of the nanoparticle relative to the wavelength of the incident light.

If we consider the case of a metallic sphere placed in an external electric field, the latter pushes the positively charged nuclei in one direction and the negatively charged electron cloud in the other, causing a polarizability of the sphere. When the electron cloud is displaced relative to the nuclei, a restoring force arises from Coulomb attraction between electrons and nuclei that results in oscillation of the electron cloud relative to the nuclear framework. The collective oscillation of the electrons is called the dipole plasmon resonance of the particle, sometimes denoted as "dipole particle plasmon resonance". [22]

To relate the dipole plasmon frequency of a metal nanoparticle to the dielectric constant, we consider the interaction of light with a spherical particle that is much smaller than the wavelength of light. Under these circumstances and by assuming the electric field of light to be constant, the interaction light/particle is governed by electrostatics rather than electrodynamics. [22] Indeed, for a nanoparticle in the size range of few tens of nm, it is fairly sufficient to take only the dipolar mode of interaction into consideration (that is what we call the "dipolar approximation") and to assume that the electric field of light is constant (called "quasistatic approximation"). In the dipolar-quasistatic approximation, the extinction cross-section for a metal sphere with radius R, such that the wavelength of light λ is $\gg$2R, is given as:

$$\sigma_{ext}(\omega) = 9\frac{\omega}{c}\epsilon_m^{3/2}V\frac{\epsilon_i(\omega)}{[\epsilon_r(\omega)+2\epsilon_m]^2+\epsilon_i(\omega)^2} \tag{1.1}$$

Where $V = \frac{4\Pi}{3}R^3$, ω is the angular frequency of the exciting radiation, ϵ_m is the dielectric constant of the surrounding medium. ϵ is the dielectric function of the metal which has a real part and an imaginary one, and is expressed as: $\epsilon(\omega) = \epsilon_r(\omega) + i\epsilon_i(\omega)$.

When shone with an incident field, the metal sphere of volume V absorbs light and hence the conduction band electrons start oscillating in phase, relative to the

nuclei, with the interacting electromagnetic field. As we said previously, this will induce two poles at the end of the sphere. We talk then about "polarizability" of the sphere which may be expressed as shown in Eq. (1.2):

$$\alpha = 3\epsilon_0 V \frac{\epsilon - \epsilon_m}{\epsilon + 2\epsilon_m} \tag{1.2}$$

Where ϵ_0 is the permittivity of vacuum.
According to Eq. (1.2), the resonance condition of the particle is fulfilled whenever the relation:

$$\epsilon_r(\omega) = -2\epsilon_m \tag{1.3}$$

is satisfied. Note here we assume that $\epsilon_i(\omega)$ is too small or/and weakly frequency dependent. [23] To satisfy the relation (1.3), it is required that the real part $\epsilon_r(\omega)$ be negative which is possible for some metals at optical frequencies. At the light frequency ω_{SP} for which the relation (1.3) is satisfied, the metal nanoparticle interacts very strongly with incident light, resulting in a collective coherent oscillation of the conduction electrons, in resonance with the electromagnetic field of light. This oscillation is known as surface plasmon resonance (SPR), which occurs in the visible frequency region for noble metal (gold, silver, and copper) nanoparticles, making them optically interesting metals.

As a result of the plasmon resonance, the electromagnetic fields are drastically enhanced around the nanoparticle. These fields, of evanescent nature, are strongly confined to the nanoscale size of the nanoparticle, meaning that we could consider the plasmons oscillations as confined photons and the nanoparticle as a nanosized lens. According to the diffraction's limit, the confinement of light to a size smaller than roughly the half of its wavelength is forbidden. Here lies the particularity of localized surface plasmon (LSP) in metal nanoparticles since they give the opportunity to confine the electromagnetic field of incident light to a nanosized volume. The potential for achieving interesting optical effects using these strongly confined photons is tremendous, the most important lies in using the largely enhanced scattering and absorption cross-sections of the nanoparticle.

Scattering of light results from the decay of oscillating plasmons by delivering their energy to the surrounding environment. On the other hand, the collisions of plasmons with many features, such as nanoparticle surface, lattice phonons, defects, and surface ligands, increase the damping and the dephasing processes which result in the generation of heat and constitutes the amount of light dissipated by the nanoparticle. Absorption and scattering together compose the extinction of

the particle. These processes are strongly enhanced at the surface plasmon resonance frequency. As a matter of fact, these are the precise properties which have prompted the ongoing intense interest in LSP and fueled the construction of LSP-based sensors and devices in ever increasing variety.

1.2.2 Tuning the surface plasmon resonance using the nanoparticle properties

Various parameters can strongly affect the optical properties of noble metal nanoparticles, namely the composition of the nanoparticle, its size, its surrounding medium, and its shape/geometry. The variation in these parameters allows tunability of both the plasmon resonance frequency as well as the strength of the plasmonic enhancement.

- Influence of the metallic nature of the nanoparticle

The dependence of the surface plasmon resonance on the dielectric function of the metal is pointed out in Eq. (1.2). The real part of the dielectric function determines the position of the frequency as mentioned in Eq. (1.3). If we assume free electron behavior for the metal, in which the conduction electrons can move freely independent from the ionic background and the ions act only as scattering centers, the real part can be described by the Drude model [21] as:

$$\epsilon_r = 1 - \frac{\omega_p^2}{\omega^2 + \gamma^2} \tag{1.4}$$

Where ω_p is the frequency of bulk plasma oscillations in the metal and γ is the electron collision frequency. Since we are assuming a free electron behavior, meaning $\gamma \ll \omega$, Eq. (1.4) can be reduced to:

$$\epsilon_r = 1 - \frac{\omega_p^2}{\omega^2} \tag{1.5}$$

The bulk plasma frequency ω_p is expressed, in terms of the free electron density N of metal, the electron charge e and the effective mass of the electron m_e, as: [24]

$$\omega_p = \sqrt{\frac{Ne^2}{\epsilon_0 m_e}} \tag{1.6}$$

Gold and silver have the same bulk plasma frequencies due to their similar electronic densities, i.e. $N = 5.90 \times 10^{22}$ and $5.86 \times 10^{22}/cm^3$, respectively. [24] However, their surface plasmon absorption band is different, around 390 nm for a

silver colloidal nanoparticle and 520 nm for a gold one. [25, 26] This difference is due to the fact that Drude model does not take into account the inter-band absorption transitions; in reality, real metals have considerable deviations from free electron behavior, except at low frequencies. To include the effect of inter-band transition and the collisions between electrons, an imaginary part must be taken into consideration for describing the dielectric function of the metal, so that Eq. (1.5) is written as:

$$\epsilon_r = \epsilon_\infty - \frac{\omega_p^2}{\omega^2} \tag{1.7}$$

ϵ_∞ describes the significant effect of the core electrons and depends on the metal electronic structure, meaning the response of 5d electrons.

Combining Eqs. (1.6), (1.7) and (1.3), we get the surface plasmon resonance frequency of a spherical particle:

$$\omega_{SP} = \sqrt{\frac{Ne^2}{\epsilon_0 m_e(2\epsilon_m + \epsilon_\infty)}} \tag{1.8}$$

Thus the real part of the dielectric function determines the frequency position of the plasmon resonance [24] and the imaginary part incorporates the plasmon dephasing and damping processes.

The line width and absorption contribution of the plasmon resonance of a metal nanoparticle is given by: [24]

$$\triangle\omega = \frac{2\epsilon_i(\omega_{SP})}{\frac{d\epsilon_r}{d\omega}|_{\omega_{SP}}} \tag{1.9}$$

This equation clearly shows that for smaller values of the imaginary part of the dielectric function of the metal and steeper values of the gradient of the real part with the frequency, the bandwidth gets narrower. [24] While the slope of $\frac{d\epsilon_r}{d\omega}$ is similar for both gold and silver, yet silver has a much lower ϵ_i as compared to gold which gives it a narrower plasmon linewidth as well as a higher scattering-to-absorption ratio. [24]
By combining together the effect of the real part and imaginary part of the dielectric function on the plasmon resonance, we can introduce the concept of "plasmonic quality" which is specified by the energy position of the plasmon resonance divided by its line width. Thus, while comparing silver and gold, we notice that silver has a higher plasmon quality; This is due to the proximity of the plasmon resonance energy to the inter-band absorption edge in case of gold which make the plasmonic fields relatively damped. However, from the practical standpoint gold is

much more resistant to oxidation as compared to silver, which makes it the metal of choice in many cases.

- Sensitivity to the outer medium

The plasmon resonance frequency of metal nanoparticles is also sensitive to the dielectric constant of the medium surrounding them. Eq. (1.3) reveals the relationship of the nanoparticle's dielectric function's (real part) at the SPR condition to the dielectric constant of the outer medium. Any increase in the refractive index of the surrounding environment requires an increase in the negative value of ϵ_r to satisfy the plasmon resonance condition. The increase in the negative value of the dielectric function induces a lowering in energy (red-shift) as illustrated in Figure 1.1 which shows the dispersion relation of the dielectric function of silver as a function of the photon energy. This is confirmed by Drude Model which is represented by the blue curve, and by Johnson and Christy represented in black curve. [1]

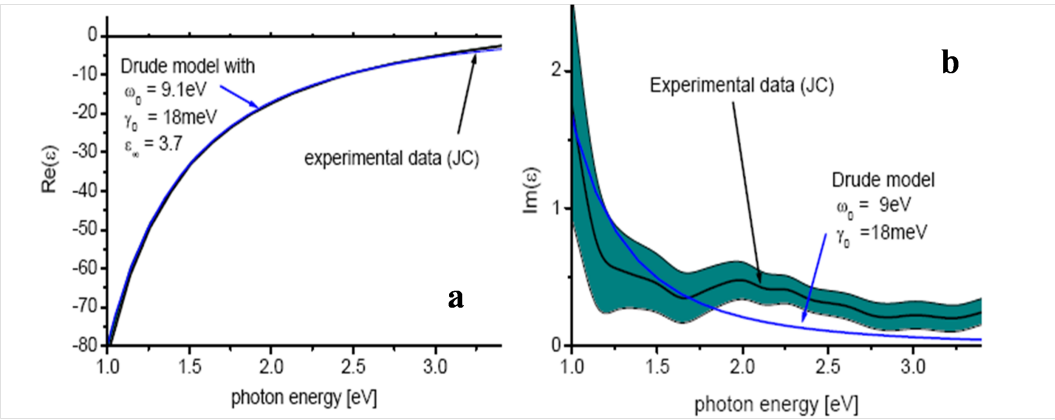

Figure 1.1: Dependence of the dielectric function of silver on the photon energy. (a) Real part; (b) Imaginary part. In both panels, Drude model is represented by the blue curve and the experimental data of Johnson and Christy [1] are represented by the black curve. (Reprinted with permission from Johnson, P. B. *et al.*, Phys. Rev. B. 6(12), 4370-4379 (1972). Copyright 1972 American Physical Society).

Moreover, the dependence of the plasmon resonance frequency of metal nanoparticles on the dielectric constant of the outer medium can be also understood as follows. The increase of the refractive index of the medium results in an increase of its resistivity; This means that the oscillating electrons will suffer more collisions with the molecules of the surrounding environment, resulting in an increase in the electromagnetic retardation, damping and multipolar effects, and significant broadening of the plasmon resonance.

- Influence of the nanoparticle size

As the size of the nanoparticle approaches the wavelength of light, it can no longer be homogeneously polarized by the light, resulting in the excitation of higher-order oscillation modes. The dipolar approximation is no longer valid in this case and it turns out that this approximation is no more sufficient to explain the observed phenomena because other processes should be taken into account. Higher-order oscillations have a resonance at progressively higher resonance frequencies, i.e. lower wavelengths. The general resonance condition for a mode of order l is given as:

$$\epsilon_r = -\frac{l+1}{l}\epsilon_m \tag{1.10}$$

For the dipolar mode l=1, meaning that Eq. (1.10) becomes same as Eq. (1.3). Higher-order modes significantly broaden the plasmon resonance due to a reduction in the phase coherence. In addition, as the particle size increases, there is increased radiative damping, i.e. emission of radiation by the plasmon oscillations, which results in an increase in the scattering contribution, but also reduces the plasmon lifetime. [27] Another effect comes from electromagnetic retardation, which results from the depolarization of the light field across the particle surface resulting in both the red-shift and broadening of the plasmon resonance band. [28]

It must be noted that, due to the retardation-induced red-shift of the nanosphere plasmon resonance, the size tunability is very limited.

- Dependence on the nanoparticle shape

While size and environment effects are very important as mentioned in the previous sections, shape effects seem to be more pronounced on the optical absorption spectrum of gold nanoparticles. [4, 29] The plasmon resonance absorption splits into two bands as the particles become more elongated along one axis. [21] The aspect ratio is the value of the long axis (length) divided by the short axis (width) of a cylindrical or rod-shaped particle. As the aspect ratio increases, the energy separation between the resonance frequencies of the two plasmon bands increases. [21] The high-energy band absorbing at around 520 nm corresponds to the oscillation of the electrons perpendicular to the major (long) rod axis and is referred to as the transverse plasmon absorption. This absorption band is relatively insensitive to the nanorod aspect ratio and coincides spectrally with the surface plasmon oscillation of the nanodots. [4] The other absorption band at lower energies is caused by the oscillation of the free electrons along the major (long) rod axis and is known as the longitudinal surface plasmon absorption.

Quantitatively, the polarizability of a spheroid is given as:

$$\alpha = \frac{\epsilon_0 V}{L}\left(\frac{\epsilon - \epsilon_m}{\epsilon + (\frac{1-L}{L})\epsilon_m}\right) \tag{1.11}$$

Where L is a depolarization factor that depends on the shape. For a sphere, which is isotropic in all three dimensions, L=1/3, which reduces Eq. (1.11) to Eq. (1.2). The plasmon resonance condition from Eq. (1.11) is given as: [21]

$$\epsilon_r = -\left(\frac{1-L}{L}\right)\epsilon_m \tag{1.12}$$

Where, for instance, the "shape parameter" L for a prolate spheroid can be written as: [30]

$$L = \frac{1-e^2}{e^2}(\frac{1}{2e}\ln\frac{1+e}{1-e} - 1) \tag{1.13}$$

With e related to the prolate spheroid aspect ratio (AR) by $e = \sqrt{1-(\frac{1}{AR})^2}$. This condition summarizes the effect of the nanoparticle shape (through L given by Eq. 1.13) on the surface plasmon resonance frequency.

1.2.3 Applications on the radiative properties of noble metallic nanoparticles

Noble metal nanocrystals are one of the most promising labels for enhanced optical detection. As already mentioned, in a metal nanoparticle, incident light can couple to the plasmon excitation of the metal, which involves the light-induced motion of all the conduction electrons in phase. Thus, the cross section for elastic light scattering from a 50-nm gold nanocrystal can be a million-fold larger than the cross section for absorption or emission of electromagnetic radiation from any molecule or even quantum dot chromophore. [31] At the same time, metal nanoparticles are photostable, unlike dyes that photobleach. Although these objects are somehow large for use inside cells, they nonetheless provide a powerful and evolving toolkit for optical imaging, especially biological detection.

As a typical example, it has been shown by Halas and colleagues that it is possible to alternately design metal and dielectric materials radially in shells, providing a high degree of control over plasmon resonances and over raman scattering

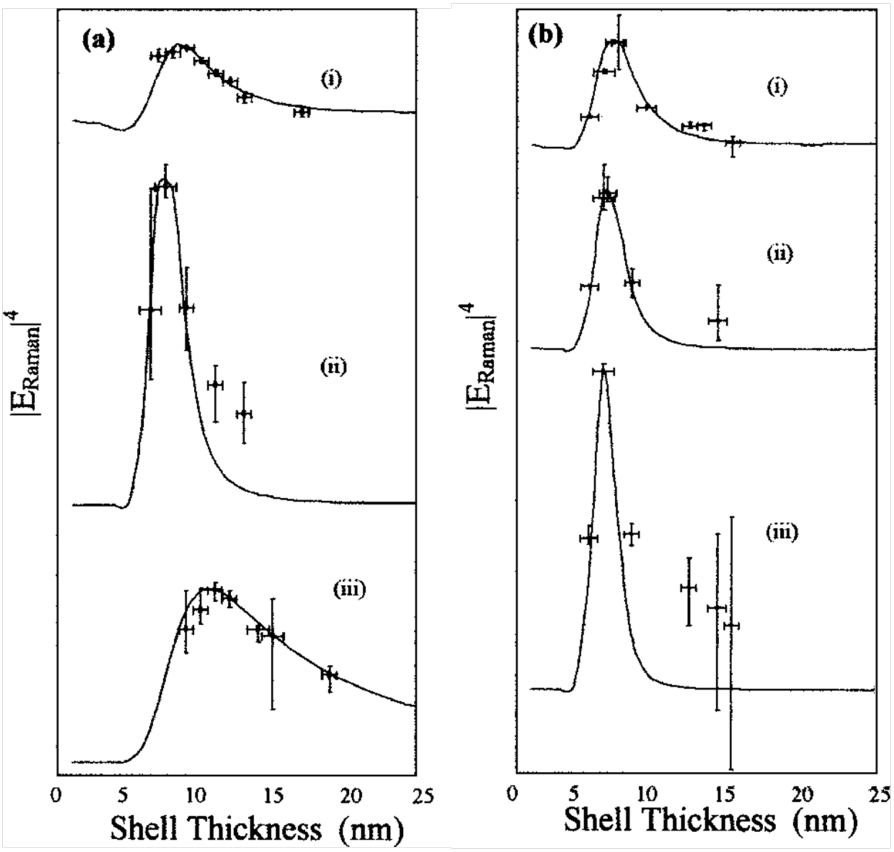

Figure 1.2: Raman spectra of pMA adsorbed on silver nanoshells as a function of the shell thickness for two values of the silica core radius. Calculated $/E_{Raman}/^4$ for (i) 390, (ii) 1077, and (iii) $1590cm^{-1}$ pMA modes (solid lines) and the measured magnitude of the mode as a function of shell thickness for (a) 79 and (b) 65 nm silica cores. (Reprinted with permission from Jackson, J. B. *et al.*, Appl. Phys. Lett. 2, 257-259 (2003). Copyright 2003 American Institute of Physics).

process [32] and also offering an important tool for biological detection. [33]

It was reported that variation of the core diameter and the metal shell layer thickness tune the local surface electromagnetic field of the nanoparticle; this electromagnetic field is monitored by measuring the Raman scattering signal from a layer of non-resonant adsorbate molecules, para-mercaptoaniline pMA, bound to the nanoparticle surface. [32] The maximum enhancements measured using this core-shell geometry correspond to a 10^6 effective enhancement in solution. The surface enhancement raman scattering (SERS) appears to be directly and exclusively due to nanoparticle geometry. Raman spectra of adsorbed molecules on

silver nanoshells were obtained for a 65-nm and a 79-nm radius silica core for a range of shell thicknesses varying from 5 to 20 nm.
In Figure 1.2, the Raman signal as a function of shell thickness is shown for each core. The solid curves for each Stokes mode (390, 1077, and 1590 cm^{-1}) of the molecule are the theoretically obtained values while the intersection between the error bars represent the experimentally obtained values. [32]

Also, El-Sayed et *al.* diagnosed cancer by using gold nanoparticle bioconjugates to image the cancer biomarker, epidermal growth factor receptor (EGFR), present in significantly higher amounts on cancer cells. [34, 35] Gold nanospheres conjugated to anti-EGFR antibodies specifically target the cancer cells and homogeneously bind to their surface with an affinity rate 600% greater than to the noncancerous cells, as shown in dark-field microscopy in Figure 1.3.

As a result, the cancer cells showed strong Mie scattering from the gold nanoparticles bounded specifically to the EGFR and therefore cancer cells could be easily identified from the healthy cells, in which case the gold nanoparticles were dispersed randomly due to non-specific binding. This imaging-based diagnostic approach is quite general since gold nanoparticles can be conjugated to a variety of proteins, antibodies, and small molecules. The targeting ligands can be chosen depending on the disease biomarkers to be targeted.

1.3 Non-radiative properties of noble metal nanoparticles

There has been also a great interest in the non-radiative processes of electronic relaxation in noble metal nanoparticles since these pathways of relaxation govern the damping and dephasing of the plasmon resonance. These processes also constitute the absorption part of the plasmon resonance.

The dynamics of non-radiative electron relaxation processes has been studied by femtosecond time-resolved laser techniques. [5, 36, 37, 38, 39] Femtosecond pulses can be used to create a non-equilibrium excitation of the metal electrons following which they relax via non-radiative processes. The femtosecond pump-probe transient absorption spectroscopy technique has become very useful in following the dynamics of the relaxation processes in plasmonic nanoparticles.

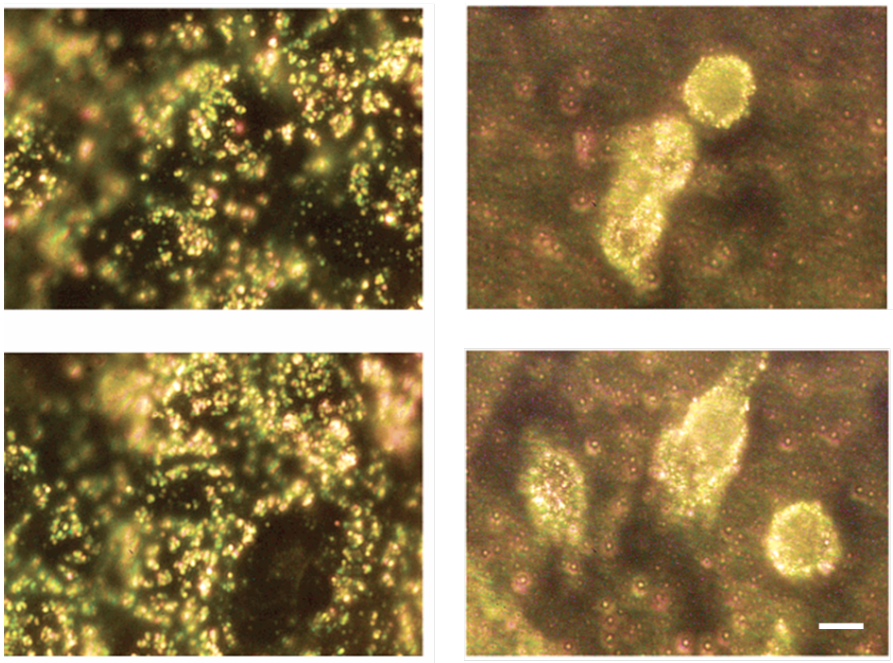

Figure 1.3: Molecular-specific imaging of cancer using gold nanoparticle/anti-EGFR conjugates. Dark-field microscopy shows, in the right panel, HSC cancerous cells clearly defined by the strong SPR scattering of gold nanospheres (top) and gold nanorods (bottom); In the left pannel, HaCat healthy cells are shown with gold nanospheres (top) and gold nanorods (bottom) randomly dispersed without specific binding. Scale bar = 10μm for all images. (Reprinted with permission from El-Sayed, I. H. *et al.*, Nano Lett. 5, 829-834 (2005). Copyright 2005 American Chemical Society).

Electrons of noble metal particles, and using pulses generated by a near-UV pump laser, can be excited through either intra-band or inter-band transitions. [36] The energy of the excited electrons is rapidly (a few hundred fs) spread over the entire electron distribution via electron-electron scattering. The exact timescale depends on the initial energy of the electrons and, therefore, which type of transition was excited. Recent results also show that the initial electron thermalization time depends on the particle size, decreasing as the size decreases. [40] However, because these initial scattering events are so fast, the essential result is the creation of a hot electron distribution just after the pump pulse. The increase in the electronic temperature can be very large, due to the very small heat capacity of electrons. Hence, the increase in the electron temperature changes the occupation of the electronic states near the Fermi level of the particles, which consequently

changes the dielectric constant of the metal and, therefore, the extinction coefficient. [41] The main result is a broadening of the plasmon band of the particles, which yields a bleach signal at the maximum of the plasmon band and absorption signals in the wings. [36] Then the kinetic traces recorded near the plasmon band maximum show an initial fast decay, which is due to energy flow from the hot electrons into the phonon modes (electron-phonon coupling), followed by a slower decay from heat dissipation to the environment, and hence the plasmon resonance absorption is recovered. The timescales for electron-phonon coupling and heat dissipation are 5 ps and $\sim$ 100 ps, respectively. [5, 36] A second femtosecond pulse overlapping with the maximum of the surface plasmon absorption of the nanoparticles is used as a probe to follow the recovery of the plasmon resonance absorption (or decay of the transient bleach) with sub-picosecond resolution, thus yielding the kinetic trace of the hot electron relaxation.

In fact, pump-probe studies have established that the electron cooling following thermalization involves an initial fast decay component, which is attributed to the exchange of the hot electron energy with the nanoparticle lattice through electron-phonon scattering. As we already mentioned, this relaxation is followed by phonon-phonon coupling processes during which the hot lattice cools and proceeds to equilibrium by transferring energy to the medium, on a timescale of hundred of ps, corresponding to a slower component of the decay. [5, 36] Thus, the light absorbed by the electrons is converted into heat within the nanoparticle, subsequently leading to the heating of the local medium that surrounds it. Perner *et al.* proved that the time evolution of the damping rate follows that of the electron temperature, showing that the damping rate is strongly influenced by transient variations in the electronic scattering rate. [38]

It must be noted that the electron-phonon relaxation time is laser pump energy dependent and it increases with increasing pump energy due to the linear increase in the electronic heat capacity. [5, 38] The consequently slower electron-phonon relaxation also mixes with the phonon-phonon relaxation rate, which is generally dependent on the thermal properties of the medium.
The absorbed light by a gold nanoparticle, smaller than 25 nm, is efficiently converted to heat on a pico-second time domain by rapid electron-phonon and phonon-phonon processes. This strong SPR absorption followed by fast energy conversion and dissipation was used for heating the local environment by using light at a frequency overlapping the nanoparticle SPR absorption band. The highly efficient and localized light to heat conversion by gold nanoparticles made them very useful for the photothermal therapy of cancers and other diseases, [42, 43] and for drug delivery .

In 2003, Pitsillides *et al.* first reported on the photothermal therapy of lymphocytes in vitro using gold nanoparticles immunoconjugates coupled with a nanosecond Nd:YAG pulsed laser at 532 nm, which induced solvent bubbles around the particles that imposed enough mechanical stress to cause cell destruction. [42]

Recent studies by El-Sayed and colleagues demonstrated the selective photothermal therapy of cancer cells in vitro by using 40-nm gold nanoparticles conjugated to anti-EGFR antibodies. [43] The cancer cells, following labeling by the antibody-conjugated nanospheres, were exposed to a visible laser. The selectivity of the method was demonstrated by the fact that the malignant cells required less than half the laser energy to be killed as compared with the benign cells. [43] The selective photodamage of the cancer cells is clearly a result of the gold nanoparticle, loaded on the cancer cells by means of the EGFR-antibodies, that has efficiently converted light into heat which has been dissipated towards the local environment. This method can be used for a variety of cancers by integrating the nanoparticles with an immunotargeting strategy specific to the particular cancer. [43]

1.4 Hybridization of metal nanoparticles

As pointed out in previous sections, noble metal particles have long fascinated scientists because of their intense color and their tremendous optical properties, which have led to various applications in different domains, namely biology, chemistry, physics and medicine. The recent resurrection of colloidal and cluster chemistry has brought about the strife for new materials that allow a bottom-up approach for building new devices with metal nanoparticles.

Nowadays, many studies are aiming to fabricate hybrid plasmonics, which means metal/other material hybrid systems, such as dielectric/metal nanoshell configuration, [13, 44, 45] electrically addressable active plasmonic structures, [14] molecular/plasmonic systems, [15, 16] and semiconductor/metal structures. [17, 18, 46] These newly introduced structures constitute the most promising solution in plasmonics because they can take advantage of the respective properties of the different components, but also can benefit from the mutual coupling between these components.

1.4.1 Configurations: dielectric/metal nanoshell, molecular/plasmonic systems, semiconductor/metal, etc.

In 2006, Halas *et al.* designed and fabricated a new hybrid nanoparticle that combines the intense local fields of nanorods with the highly tunable plasmon resonances of nanoshells. The fabricated dielectric core-metallic shell prolate nanoparticle bears a remarkable resemblance to a grain of rice, inspiring the name "nanorice". Studies on the new hybrid nanoparticle show that this geometry possesses greater structural tunability than either a nanorod or a nanoshell, along with much larger local field intensity enhancements and greater sensitivity as a SPR nanosensor. [44]

In 2008, the same group showed that the plasmonic properties of metal-dielectric nanoparticles exhibit a highly sensitive dependence on geometry, due to the interaction between the plasmon modes associated with the surface of the nanoparticle. [13, 45] Changes in nanoparticle geometry that reduce symmetry alter the interactions between plasmon modes and give rise to modified, and altogether new, plasmonic features. By examining the near- and far-field optical properties of three variants of a core-shell nanoparticle, nanoshells, nanoeggs and nanocups, [13, 45] Halas and colleagues noticed that the absorption and scattering spectra of a nanoegg reveal the emergence of multipolar peaks strongly red-shifted relative to those of nanoshells and larger near-field enhancements. The wavelength of maximum field enhancement increases with increasing core offset, distinct from the dipole resonance of the nanoparticle. For larger nanoeggs beyond the dipolar regime, it has been shown that the variations in the relative contribution of scattering and absorption to the nanoparticle extinction depend upon both the core-shell offset and the overall particle size. [13, 45] These observations may lead to new opportunities to tailor near- and far-field properties of plasmonic nanoparticles for specific applications, such as high performance surface-enhanced spectroscopy, bioimaging and nanoparticle-based therapeutics.

To increase solar cell efficiency, Hägglund *et al.* also introduced in 2008 a new type of hybrid configuration: molecule/plasmonic structure that lies on utilizing the surface plasmons of nanoparticles to enhance charge carrier generation in dye sensitized solar cells. [15] So the group has used localized surface plasmons of elliptical gold disks to improve the conversion and cost efficiencies of photovoltaic solar cells by enhancing the photon capture cross-section. Photoconductivity measurements were performed on flat TiO_2 films, sensitized by a combination of dye molecules and arrays of nanofabricated elliptical gold disks. [15] The electromagnetic coupling between the noble metal disks and the dye molecules amplifies the excitation of these molecules which enhances the generation of charge carrier and leads to an exceptionally fast charge separation. Then photoexcited dye molecules inject electrons into the photoactive region (semiconductor TiO_2) of the solar cell at a rate much greater than that needed to decay to background state. [15] Finally,

the injected electrons are extracted as a photocurrent provided that the circuit is closed.

In 2007, Ginger and colleagues used deoxyribonucleic acid (DNA) as a biological linker to attach fluorescent dyes at a fixed distance from single silver nanoprisms. [16] They have shown that the dye-functionalized nanoprisms are highly fluorescent, and their fluorescence intensity is a sensitive function of the degree of spectral overlap between the nanoparticle localized surface plasmon resonance (LSPR) and the absorption and emission spectra of the dye. [16] As a typical example, for dyes attached to a 5.5-nm thick DNA layers, the brightest fluorescence is usually obtained near nanoparticles with LSPR peaks that are only slightly blue-shifted from the dye emission peak. These results provide concrete empirical guidelines for selecting the best metal colloids as supports for particular fluorescence applications. These results will benefit attempts to use metal-enhanced fluorescence in both biosensing and thin-film optoelectronics applications. This type of hybridization is wide spread and widely studied.

Semiconductor/metal hybrid structures have been developed by Woggon *et al.* in 2007. [17] The group has introduced an experimental realization of a 1-D plasmonic nanocavity consisting of a single silver (Ag) nanowire functionalized with CdSe nanocrystals on top of a 15-nm thin SiO_2 layer. The prototype structure is optimized to study cavity quantum electrodynamics phenomena (exciton-photon coupling, atom-photon entanglement, photon statistics, ...) by varying the nanocrystal CdSe-Ag nanowire distance d and the cavity length L; thus, from the modulation of the nanocrystal emission by the cavity modes, it has been able to derive a plasmon group velocity. [17] Despite the very low and far from being optimized quality factor of this plasmonic nanocavity, efficient exciton-plasmon-photon conversion and nanoscale guiding were demonstrated along with a modification in the spontaneous emission rate of the coupled exciton-plasmon system.

Berthelot *et al.* demonstrated in 2009 an active control over individual antenna performances by an external electrical trigger. [14] The group found an electrical means to control the interaction strength between two metallic nanoparticles forming an optical dimer antenna. The control is obtained by modifying the dielectric medium surrounding the dimer antenna through the adjustment of the in-plane orientation of liquid crystal molecules. The response of the antennas was found to be strongly dependent on the polarization of the light and the orientation of the controlled electric field lines with respect to the antenna axis.

Indeed, Berthelot and colleagues demonstrated an increased optical interaction if the antenna, the field lines and the polarization were collinear. They found that under a bias condition, dimer antenna behaves like a disk antenna if the geometric axis of the antenna is perpendicular to the field lines and polarization. [14]

1.4.2 Hybrid nanostructures of our group: metal/polymer

A couple of years ago, our group at LNIO has developed a new way of hybridization [19, 20, 47] consisting of metal/polymer nanostructures. Our approach is based on nanoscale photopolymerization initiated by the enhanced near-field of noble metal nanoparticles, which leads to the production of metal/polymer hybrid nano-systems with novel optical properties.

The sample of metal nanoparticles, namely commercial colloidal silver nanoparticles, chemically synthesized gold colloids, and lithographic nanoparticles, is firstly fabricated. These structures are then characterized by extinction and/or scattering spectroscopy to identify their spectral response and by atomic force microscopy (AFM) or scanning electron microscopy (SEM) to check their size and form.

In parallel, a photosensitive formulation consisting of dye molecules, amine molecules and an acrylate monomer is prepared and characterized by means of far-field studies. [48] Indeed, the threshold condition of the photosensitive formulation for which the chemical process is initiated should be precisely determined. This photosensitive system is utilized to characterize the optical near-field of the metal structures.

After formulation deposition on the metal nanoparticles, the sample is illuminated in normal incidence by a plane wave of controlled linear polarization. Irradiation intensities below the threshold are performed so that the photopolymerization can only occur in close proximity of the metallic nanoparticles due to their enhanced dipolar mode of the optical near-field. After this procedure, we end up with a hybrid metal/polymer structure consisting of the metal nanoparticle and two photopolymer lobes formed only on the end of the optical nanosource and directed along the polarization of impinging field.

The experimental details of our approach are presented in the coming section.

1.5 Presentation of our approach

As we already mentioned, the nanoscale polymerization is triggered by locally enhanced fields of metal particles resulting from their dipolar plasmon resonance. [19] As a result, a polymer mold is obtained around the silver nanoparticles, clearly reflecting the dipolar near-field pattern. Precise characterization by AFM allows us to extract quantitative values that are characteristics of the plasmonic response of the silver structures. In other words, the photosensitive molecules act as near-field molecular probes allowing for near-field quantitative characterization and photography with sub-10-nm resolution.

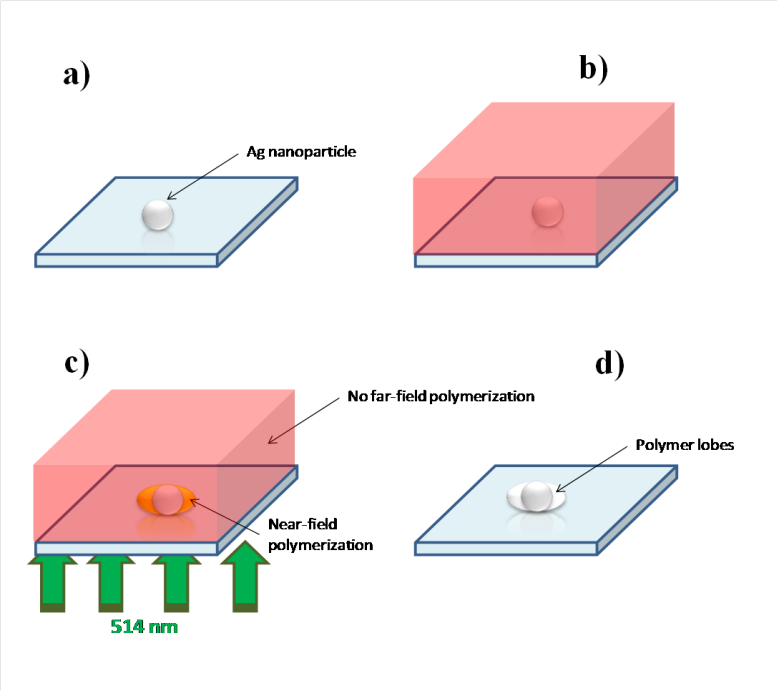

Figure 1.4: Scheme of the approach. a) Ag NP deposited on a functionalized glass substrate. b) Deposition of the photopolymerizable formulation. c) Plasmon based near-field photopolymerization of the photosensitive solution leading to two wings corresponding to the dipolar LSP resonance. d) The resulting hybrid nanoparticle is revealed by rinsing procedure.

Typically, colloidal silver nanoparticles (Ag NPs) are deposited on a functionalized glass surface, as shown in Figure 1.4 (a). They consist mainly of single particles and dimers whose diameter varies between 40 nm and 80 nm. An aminosilane surface functionalization, [49] which will be discussed in details in Section 2.2, allows them to stay firmly attached to the glass plate and, in particular, to resist the various stages of rinsing. Lithographic particles (LNP) are also used as

nanosources of light as it will be seen in Chapter 3 Section 2. Silver was chosen to achieve mutual spectral overlapping between photopolymer absorption and SPR of the metal nanoparticles embedded in liquid polymer. The Ag NPs and the LNP can be viewed as plasmonic nanoantennas that enable nanoscale coupling between the free space and photosensitive molecules, through local field confinement and energy transfer.

After characterizing the Ag NPs by AFM, a drop of liquid of a free-radical photopolymerizable formulation is deposited onto the sample, as illustrated in Figure 1.4 (b). The chemical system is characterized by a threshold dose E_{th} below which no polymerization can occur, that is systematically quantified by far-field pre-studies. The non-linear threshold behavior of the formulation allows for high resolution patterning under evanescent illumination. The sample is then illuminated, as shown in Figure 1.4(c), in normal incidence with a 1-cm wide linearly polarized laser beam issued from an Argon Krypton (Ar:Kr) laser source, with a dose that is below E_{th} to avoid any far-field polymerization. Only locally enhanced near-fields can prompt the polymerization (see Figure 1.4 (c). After rinsing procedure, we end up with two lobes of polymer corresponding to the dipolar localized surface plasmons response of the Ag NPs, as represented in Figure 1.4(d). The hybrid "metal/polymer" structure is finally re-characterized by AFM. The whole procedure is applied to labeled metal nanoparticles, which allows us to investigate single Ag NPs. [19]

1.6 Characterization of the optical properties of noble metal nanoparticles

The hybridization approach of our group presented in the previous section consists not only on the fabrication of hybrid nanoparticles metal/polymer, but also on a quantitative characterization of the near-field of noble metal nanoparticles. It will be shown in Chapter 3 our ability to directly image the dipolar profile of the near-field distribution with a resolution better than 5 nm and to *quantify* the near-field depth and the near-field enhancement factor. We were also able, as it will be demonstrated in Chapter 3, to achieve a near-field spectral signature of the metal nanosource.

Currently, three main approaches are used for characterizing plasmonic structures:

- Approach 1: Far-field spectroscopy and microscopy.
- Approach 2: Near-field optical microscopy.
- Approach 3: Approaches based on electron microscopy such as photo-emission electron microscopy (PEEM) and electron energy loss spectroscopy (EELS).

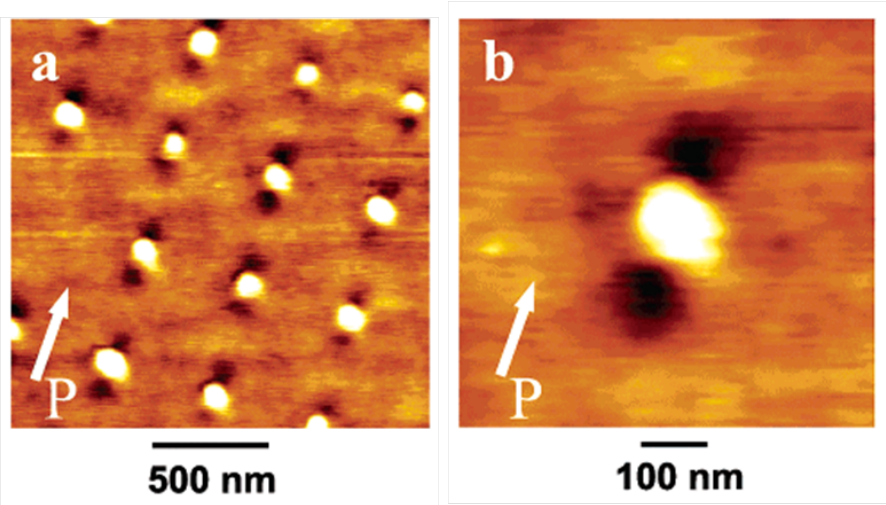

Figure 1.5: Topographic images of optical near-fields around silver nanoparticles. (a,b) AFM images recorded after irradiation of silver particles covered with azobenzene. Irradiation wavelength, time, and intensity were, respectively, 532 nm, 20 min and 50 mW/cm^2. The light polarization direction is indicated within the AFM images. The silver particles have a diameter of 75 nm, a height of 50 nm, and a periodicity of 500 nm. MIBK was used as the solvent. (Reprinted with permission from Hubert, C. *et al.*, Nano Lett. 5, 615-619 (2005). Copyright 2005 American Chemical Society).

Far-field spectroscopy and microscopy are diffraction-limited. In fact, at the end of the nineteenth century, Abbe and Rayleigh derived a criterion for the minimum distance Δx between two point sources at which they can still be unambiguously distinguished as two separate sources. Abbe's criterion reads as: [50]

$$\Delta x = \frac{0.61 \times \lambda}{NA} \tag{1.14}$$

Here, $NA = nsin\theta_{max}$ is the numerical aperture, a property of the optical system. n is the index of refraction of the surrounding medium and θ_{max} is the maximum collection angle of the optical system. The best possible NA is NA=n which, for optical glasses, is NA$\approx$1.5 and hence $\Delta x \approx \frac{\lambda}{3}$. Below the criterion

introduced in Eq. (1.14), two point sources can not spatially resolved.

Near-field optics has its origin in the effort of overcoming the diffraction limit of optical imaging. While scanning near-field microscopy (SNOM) offers a lateral resolution down to tens of nanometers (20-100 nm), [51, 52, 53] the measurement proceeds by the insertion of a probe in the immediate vicinity of the object under study, to locally either detect or excite the evanescent field. The presence of the probe generally perturbs the physics of the sample to be characterized and the effective object becomes a complex probe-sample nanosystem whose physics strongly depends on probe features (geometry, material, etc.). Additionally, producing high quality SNOM probes in a reproducible way remains a critical issue.

The use of localized surface plasmons of metal nanoparticles as a source of lithography in near-field, was developed at our university in the LNIO. It has been shown by Bachelot and coworkers that it is possible to structure a photosensitive layer using the localized surface plasmons of noble metal nanoparticles to end up by mapping the distribution of the near-field intensity around these nanoparticles. [54, 55] The technique is based on irradiation of a homogeneous layer of azobenzene based copolymer at a wavelength corresponding to the resonance of surface plasmon of silver metal nanoparticles covered with the photopolymer.
Figure 1.5 shows AFM images recorded after irradiation. [54] This approach helped to highlight the dipolar field of metal nanoparticles through its signature on the resin. The two holes parallel to the direction of incident polarization are due to the movement of azobenzene molecules escaping the near-field excited by the surface plasmons in the vicinity of metal nanoparticles.
Although this imaging technique constitutes a powerful way to map the near-field of noble metal nanoparticles by means of photosensitive molecules, which replaces the perturbative probe used in SNOM; yet this technique does not quantify the near-field.

Photoemission electron microscopy (PEEM) was recently developed as a tool for characterizing plasmonic structures. [56, 57] Indeed, photoemission can be strongly enhanced upon excitation of surface plasmons. By collecting the photoemitted electrons, two-dimensional intensity maps reflecting the actual distribution of the optical near-field can be obtained. Although this imaging technique involves no physical probe which may alter the measure and provides full field spectroscopic images with a routine spatial resolution of the order of 20 nm (down to 3 nm with recent aberration corrected instruments), it is of indirect nature.

As a matter of fact, PEEM relies on the photoelectric effects converting photons into electrons. This is also true in the case of electron energy-loss spectroscopy technique (EELS), [58] which is an analytical technique that measures the change in kinetic energy of electrons after they have interacted with a specimen. This type of microscopy is sensitive to electronic energy loss with no photons involved. Despite their power, these approaches listed under 3) are of indirect nature.

Consequently, we perceive, after the description of the three main approaches used to characterize plasmonic structures, that a real quantification of LSP of metal nanostructures still constitutes a key challenge in the near-field optics community. In this dissertation, we demonstrate a novel method that addresses this challenge by utilizing near-field photopolymerization to quantitatively characterize the optical near-field of silver nanoparticles. This technique was presented in Section 1.5 and will be detailed in Chapter 3.

1.7 Conclusions

In this chapter, a brief history about optical properties of noble metal nanostructures has been given. We differentiated between radiative properties of metal nanoparticles mainly resulting from the decay of oscillating plasmons by radiating their energy to the surrounding environment, and between the non-radiative properties of these particles which constitutes the amount of light absorbed by the nanoparticle caused by the collisions of the oscillating plasmons with other electrons, nanoparticle surface, lattice phonons, defects, etc.
Some applications on the radiative and non-radiative properties of noble metal structures were also presented to highlight the difference between these two types of properties and their potential. Then, an overview on the hybridization of metal nanostructures achieved by other groups around the world was given, followed by the description of the hybridized "metal/polymer" structures of our group. The detailed description of our approach was then presented. The last section of this chapter has detailed the different approaches that are used for characterizing plasmonic nanostructures. The weakness of these approaches in quantitatively imaging LSP was highlighted in this section.

The motivations of this thesis work are numerous. The first one lies in the implementation of hybrid nanoparticles with new features for nanophotonics. The optical near- field generated by metal nanoparticles will be used as an energy source to induce local photopolymerization, thus creating new hybrid metal/polymer nanoobjects. The innovative point of this approach is the use of confined and

intense energy sources to alter and structure matter at the nanoscale. Hence, the spatially inhomogeneous electromagnetic intensity distribution enhanced by the underlying surface plasmons leads to an anisotropic structuring of the two lobes of polymer, in the same direction as the polarization of the incident field, providing a hybrid structure with unique optical properties. Introducing a controllable degree of surface plasmon resonance tunability constitutes the first motivation of our approach.

This approach has been developed primarily as a new method for direct imaging the spatial profile of the near-field of metal nanoparticles. As a matter of fact, several efforts have been made to better understand the near-field of noble metal nanostructures and to probe its characteristics, such as its enhancement factor and its depth. So far, experiments in this area have mainly relied on scanning probe microscopy [6, 59] to achieve such near-field characterization. However, these methods are limited in applications and suffer from low throughput and the complications of the probe material effects and artifacts. Thus, our second motivation comes from the need to develop a powerful method to image the near-field of nanoparticles and to quantify it without being limited by the complications of scanning near-field microscopy.

Besides structuring the polymer at the nanometric scale, which may interest the polymer community, several properties and processes involved in polymer science may be coupled to, or assisted by, metal nanostructures at the nanoscale. These include nonlinear or electro-optical properties and possible doping of the chemical solution with luminescent organic materials or quantum dots. Furthermore, different degrees of symmetry could be achieved by using high order plasmon modes selected by proper incident polarization and wavelength. All these ideas constitute additional motivations behind this work.

As we have seen during the presentation of our approach (see Section 1.5) that metal nanostructures as well as photosensitive chemical solutions are used during our experiments. Many preliminary studies reveal of great importance to correctly chose the metal nanoparticle, as a function of its nature, shape, size, and to efficiently understand the photopolymerizable system. These studies are shown in the following Chapter.

Thus, in Chapter two, the different types of metal structures that have been used during this work will be discussed. We will also detail the techniques used to fabricate them and the different methods followed for their characterization. The different types of photochemical formulations employed during the thesis will also be detailed in this chapter, along with the far-field studies used to characterize

them.

Chapter three is dedicated to the interaction metal/photopolymerizable solutions. Firstly, we will show the different achieved experiments in nanophotopolymerization. Then, and based on these manipulations, we will elucidate the reason for which we decided to work with a precise type of chemical solution and metal structures.
Our experimental approach that is capable of quantitatively image LSP with sub-wavelength resolution will be therefore detailed in Chapter three. Indeed, the quantitative parametric analysis performed on the surface plasmons of metal nanoparticles using molecular probes will be shown and the usage of this technique for reliable and comprehensive characterization of plasmonic near-fields will be reported.

In Chapter four, we will study the local surface charges distribution on the surface of metallic nanoparticles irradiated off their resonances. For this purpose, nanoscale resolution maps of the spatial distribution of the surface charge density created by the electric field discontinuity at a non-resonant metal/dielectric interface will be shown.
As a final touch in this work, Chapter five will prove that the nanoscale photopolymerization approach does not only map the near-field of metal nanoparticles, yet it constitutes, from a more fundamental point of view, a unique opportunity to investigate nanophotochemistry.

Chapter Two

Experiment: Development and Innovations

2.1 Introduction

The selection of nanoparticles for achieving efficient contrast for biological and cell imaging applications, for photothermal therapeutic applications, as well as for interaction with molecular systems, is based on the optical properties of the nanoparticles. [60, 61, 62] A quantitative study revealing the influence of different parameters on the particle plasmon resonance turns out to be highly needed, in order to chose the right nanoparticle for a specific application. In the present chapter, such quantitative study, including the fabrication and the characterization of noble metal nanoparticles, without any interaction with molecular systems, is presented. The composition, the chemical mechanism, and the characterization of the different photopolymerizable solutions, used during this PhD work, will be also discussed in this chapter. The achieved studies allowed us to be more familiar with the physics of the different types of nanostructures used along this work. We became also aware of the interaction of the photosensitive molecules with light. The interaction between the metal nanoparticles and the molecular systems will be the subject of the 3th, 4th and 5th chapters.

The elaboration of different types of noble metal nanoparticles will be discussed in the second section of this Chapter; the different ways used to characterize the fabricated particles and to highlight the influence of different parameters on the position of the plasmon resonance are detailed in section three. In section four, we present the optimum parameters to produce lithographic nanoparticles. The preparation and the photopolymerizable mechanism of different photosensitive solutions will be discussed in section five. Then, sections six and seven will be dedicated to the characterization of the different types of molecular systems, using

an interferometric and a focalized laser spot experimental setups, respectively. A conclusion will end up this chapter.

2.2 Elaboration of samples

Synthesis techniques to generate metal nanoparticles depend on isolation of small amounts of a material. There are two general strategies to obtain materials on the nanoscale. [63] The bottom-up method is one where the atoms, produced from reduction of ions, are assembled to generate nanostructures. The top-down method is where material is removed from the bulk, leaving only the desired nanostructures. To elaborate our samples, we referred to two techniques: one bottom-up by using silver colloidal nanoparticles synthesized commercially [64] and one top-down by using electron beam lithography method. In this section, we propose to present the methods of preparation of metal nanoparticles.

2.2.1 Lithographic particles

The electron beam lithography technique (EBL) lies on steering a beam of electrons so that it can address specifically the different areas we want to insole. This nanofabrication technique was developed in our laboratory since more than ten years. [55, 65, 66, 67] The principal manufacturing steps are illustrated in Figure 2.1.

Cleaning substrate and spin-coating an "electron-sensitive" polymer

On a cleaned glass substrate, we deposit by spin-coating a film of "electron-sensitive" polymer: polymethyl methacrylate (PMMA) whose molecular weight is equal to 950 k, as it is schematized in Figure 2.1. The PMMA is already dissolved in a solvent, the methyl isobutyl ketone (MIBK) at a concentration of 30 g/l. An acceleration of 4000 round.min^{-1}.s^{-1} and a speed of 3000 round.min^{-1} give a PMMA layer of 150-nm thick.

Actually by spin-coating the glass substrate, we are applying to it a centrifugal force which enables a uniform distribution at the polymer surface. The thickness of resin depends on both the speed rotation of the sample, the amount of resin deposited on its surface, and on the viscosity of the solution of PMMA/MIBK. Typically, we used in our studies a thickness of 150 nm. As a matter of fact, the choice of the thickness deposited depends on the height of structures that we want to achieve. A ratio of 3 to 1, between the thickness of the polymer layer and the height of the metal nanostructures, must always be taken into consideration.

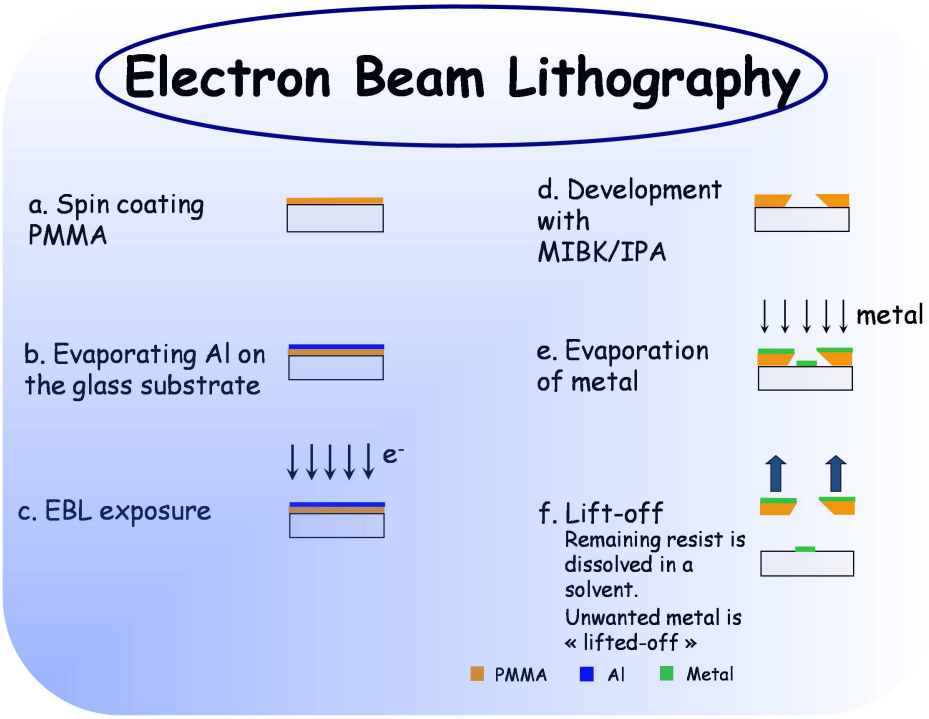

Figure 2.1: Scheme representing the most principles steps needed to fabricate metal nanoparticles using EBL

Thus, the PMMA film must have a thickness of 150 nm to produce nanoparticles of 50-nm height. The resin is then annealed for 3 hr in an oven at 160°C in order to evaporate the solvent.

Evaporation of a thin layer of Aluminum

In order to avoid accumulation of charges on the glass substrate during EBL exposure, which may causes a disruption of the incident electron beam, we used to evaporate 10-nm aluminum (Al) on the layer of PMMA. The deposited Al layer is shown in Figure 2.1 (b).

EBL exposure

Irradiation, illustrated in Figure 2.1 (c), is then performed using a SEM, Hitachi S-3500N, associated to a beam control system, nanometer pattern generation system (NPGS). The geometry of the needed nanostructures is precisely controlled by various parameters: current intensity, magnification of microscope, etc. Typically, we used a current intensity of 10 pA and a magnification of 1000. We must note that the exposure parameters such as the time of insolation, the accelerating

voltage, the dose of irradiation, in addition to the beam alignment and the correction of astigmatism are all set up and checked by the user of the microscope before each lithography.

Development of sample with KOH then with MIBK/IPA

After irradiation, the aluminum layer is removed by immersing the sample in KOH solution for about 15 s. The exposure of the resin to electrons change its chemical composition by breaking its chains, making it soluble in a solution of MIBK. The solution used is a mixture of MIBK and isopropanol (IPA) in a volume proportion of 1 to 3. After this development step followed by rinsing the substrate with IPA, we end up with a pattern lithographed sample, as seen in Figure 2.1 (d). In other words, the substrate is a mask outlining the resin desired patterns.

Metal evaporation

To obtain a low surface roughness, evaporation of metal must be made at low pressure and low deposition rate. Moreover, for optical applications that are highly dependent on the dielectric function of material and on the thickness of the layer as in our case, it is necessary that the method is reliable and reproducible. All metal deposits have been made through an evaporator society PLASSYS, equipped with thermal crucibles as well as electron gun ones. The quality and stability vacuum within the enclosure are provided by a cryogenic pump. The thickness of the deposited material is precisely controlled by a quartz balance. Using this evaporator, the deposition of the desired thickness of metal, 50 nm for most of our samples, is done as schemed in Figure 2.1 (e).

Lift-off

The last step of the manufacturing process is to dissolve the unexposed zone of the PMMA film in acetone (Figure 2.1 (f)). This is the stage of development or " lift-off ". A SEM image showing the shape of the obtained nanoparticles is presented in Figure 2.2.

The ability to control the geometry of the structured nanoparticles achieved by EBL is actually of great importance because their surface plasmon resonances can then be tuned in the desired range of wavelength, which is rarely the case with other techniques.

2.2.2 Chemically synthesized particles

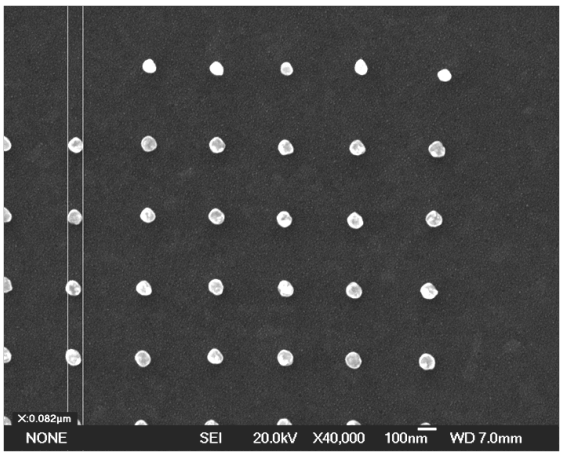

Figure 2.2: SEM image, done at the "laboratoire Interdisciplinaire Carnot de Bourgogne" at Dijon, showing cylindrical silver nanoparticles,

The glass slide is firstly functionalized to create an amine-terminated self-assembled monolayer on which silver nanoparticles, stabilized by citrate groups, are strongly bounded to the glass surface. This enables a well dispersed configuration of commercially synthesized [64] colloidal nanoparticles on the substrate surface.
The overall procedure to functionalize the glass slides [49, 68] is described in detail as follows and schematized in Figure 2.3.

Activation of the susbtrate

The slide is soaked in a freshly prepared piranha solution (2/3 of H_2SO_4 and 1/3 of H_2O_2) at ambient temperature for 2 hr to remove organic impurities and to create silanol groups on the surface, then it is rinsed thoroughly with water.

Aminezation of the slide

The cleaned slide is then submerged in a 0.8 % amino-silane solution of anhydrous toluene ($<$ 20 ppm of H_2O) for 24 hr. Then, the substrate is removed and rinsed with toluene and acetone to remove unbound materials from the surface. This treatment allows us to obtain a monolayer of amine grafted to the surface. This layer is believed to have a thickness of $7A^0$. [68] Finally, the slide is dried in a stream of dry air. An amine-coated slide is thus acquired.

Attachment of silver nanoparticles to the slide

The amine-coated substrate is immersed in the silver colloidal solution [64] for 12 hr at room temperature in order to form a monolayer of silver nanoparticles.

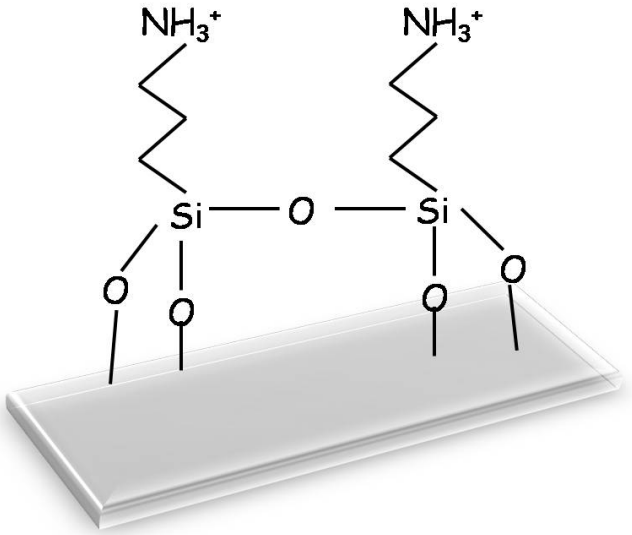

Figure 2.3: Scheme showing the result of the glass slide's functionalization

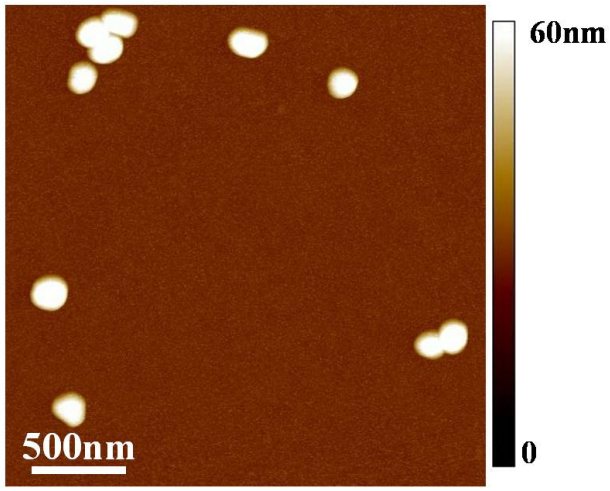

Figure 2.4: AFM image showing silver colloidal nanoparticles grafted to the amino-silane functionalized surface.

Then the sample is rinsed with water and dried with air.
An AFM image showing the colloidal nanoparticles grafted to the surface of the amino-silane functionalized glass sheet is shown in Figure 2.4.

2.3 Optimizing the fabrication of nanoparticles by e-beam lithography

Before going into the section in which we optically characterize the elaborated lithographic and colloidal samples, we suggest to go a bit through the details of the problems we had while fabricating particles using EBL. We believe that, in this way, readers of this manuscript will learn more about this point.
During the manufacture of lithographic metal nanoparticles, we faced two problems:
1. The plasmons resonance of silver nanoparticles was shifted toward the red region, almost in the range of 700 nm, although we do expect this resonance to be in the green region.
2. Rest of PMMA on and between metal particles.
Fronting the first problem, we have decided to test the purity of the metal, the crucible of the evaporator in which the silver metal is deposited and that of the enclosure in which the metal is evaporated. After several tests, we managed to find the problem: the crucible was contaminated since it was used to evaporate different types of metals.

Figure 2.5 illustrates the relationship between the position of resonance depending on the diameter of silver particles, evaporated using the contaminated crucible and a new one. The positions of the resonances of gold particles are shown for comparison. This figure shows clearly the contamination of the crucible, which is most likely a contamination by gold, by comparing the results of silver with those for gold: the positions of the resonances of the silver nanoparticles are obviously shifted toward the red due this contamination.

To remove the rest of PMMA from the top of patterns and in between metal particles, we rinsed the samples with toluene after the lift-off with acetone; this post-rinsing procedure has been adopted for the first time. Figure 2.6 shows the same pattern before and after rinsing with toluene: the presence of residual PMMA in Figure 2.6 (a) is clear, despite the lift-off procedure.

For a good comparison, we have represented in Figure 2.7 the change in position of resonance depending on the diameter of silver particles, before and after rinsing with toluene. The green curve in Figure 2.7 confirms the presence of residual PMMA between the particles after the lift-off procedure because the values of wavelength are slightly shifted toward the red. After toluene rinsing procedure, the particles are surrounded by air that has a refractive index smaller than that of PMMA; Thus, we see this blue-shift for the values of resonance illustrated by the blue curve.

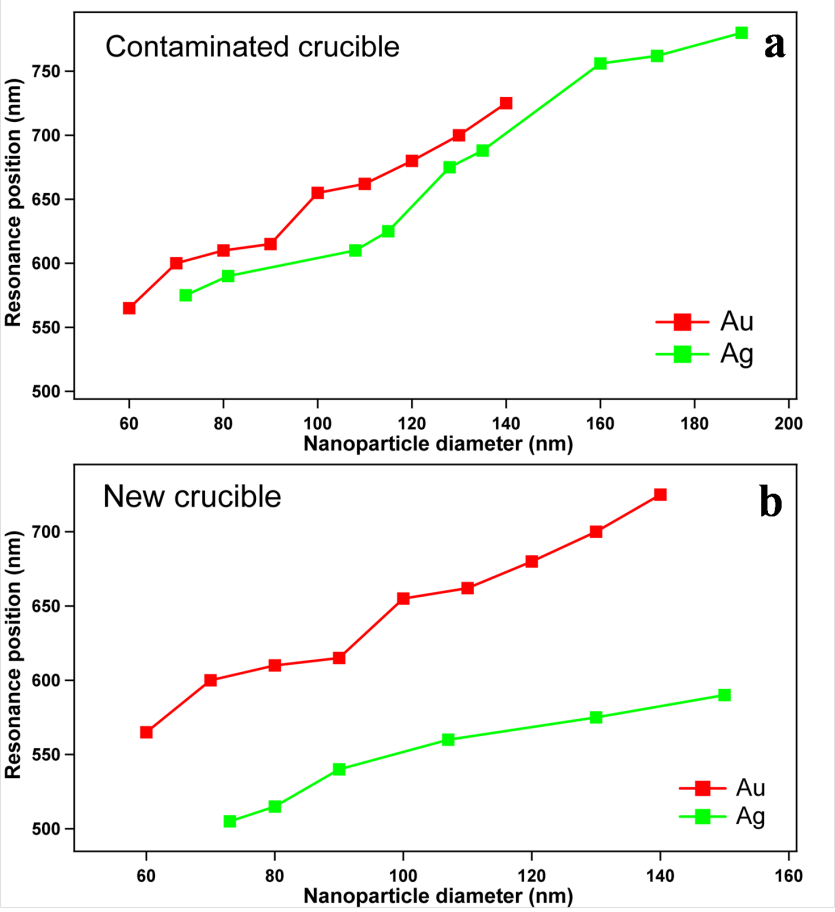

Figure 2.5: Resonance position as a function of the nanoparticle diameter. (a) using contaminated crucible. (b) using a new crucible.

2.4 Characterization of the fabricated samples

As already shown in Figures 2.2 and 2.4, the fabricated samples have been characterized by different techniques: SEM and AFM were used to check the shape and size of the elaborated particles and extinction and scattering spectroscopy were also carried to determine the plasmons resonance position. In the following sub-sections, we present the methods handled to characterize the metal particles elaborated by EBL, as well as the commercial colloidal nanoparticles.

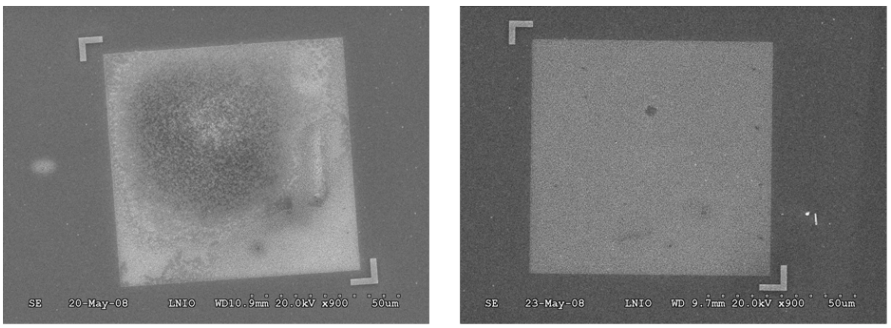

Figure 2.6: Evidence of the residual PMMA on the nanoparticles pattern: SEM images for the same pattern of silver nanoparticles before rinsing with toluene (left) and after rinsing with toluene (right).

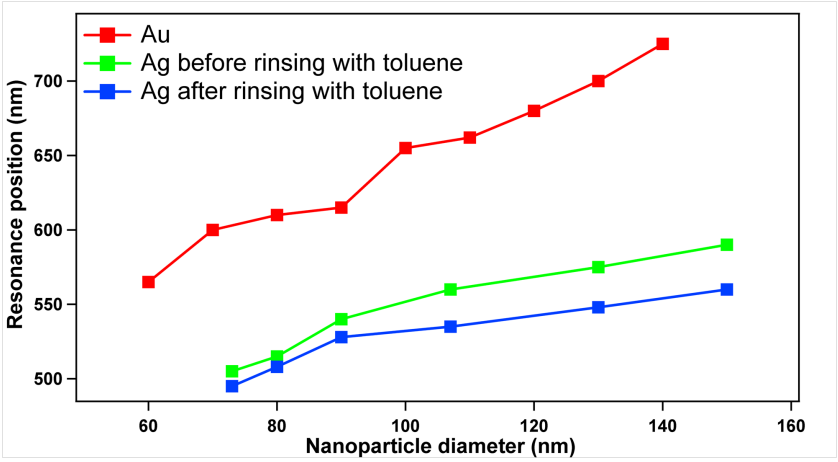

Figure 2.7: Comparison of the resonance position for the same pattern before rinsing (green curve) and after being rinsed with toluene (blue curve).

2.4.1 Characterization of lithographically fabricated nanoparticles

SEM Characterization

After EBL technique, the size and shape of the particles has been checked by SEM. Typical SEM images are presented in Figure 2.8. Both panels in this figure shows silver nanoparticles of 50-nm height and 300-nm edge-to-edge distance between two successive particles. The only difference is the diameter of the nanoparticles: 87 nm in panel (a) and 63 nm in panel (b).

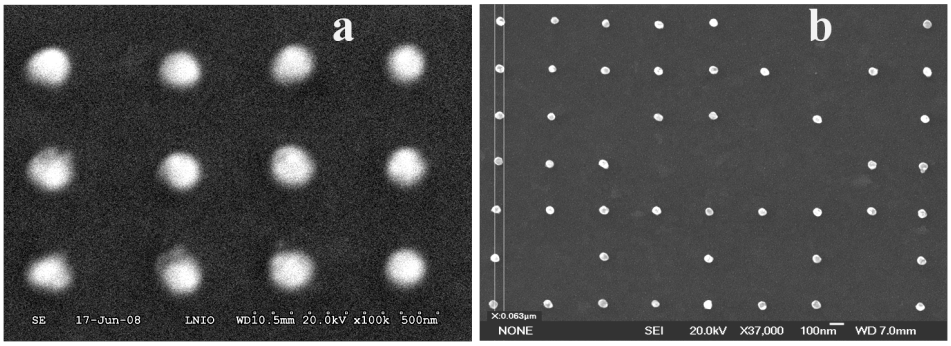

Figure 2.8: SEM image for a pattern of silver nanoparticles. (a) SEM image at LNIO. (b) SEM image at the "laboratoire Interdisciplinaire Carnot de Bourgogne" at Dijon.

Characterization by means of extinction spectroscopy

These particles have been also characterized by extinction spectroscopy in order to determine the position of the plasmons resonance. To be more familiar with the effect of various parameters, namely the nanoparticle size, the nanoparticles distribution, the nature of metal, the index of refraction of the outer medium, on the resonance position, several studies have been made. In the following, we highlight the effect of these parameters on the resonance position by means of extinction spectra.

- Effect of the nanoparticle size

As predicted by Mie theory and discussed in Chapter 1, the increase of the nanoparticle size leads to a broadening and a red-shift in the LSPR. These predictions were confirmed by many experiments along the last decades. [69] Furthermore, our experiments confirmed the forecasts of Mie theory.

Figure 2.9 shows the extinction spectra for an ordered pattern of silver nanoparticles. In this parametric study, the diameter of the particle was the varying parameter; all other parameters were kept constant. While the diameter has been varied between 87 nm and 130 nm, the thickness of the particles was 50 nm and the distance edge-to-edge was 300 nm. Extinction spectrum for the 87-nm diameter silver nanoparticles corresponds to the particles shown in the SEM image in Figure 2.8 (a). Figure 2.9 confirms the red-shift of the resonance position as the diameter of the nanoparticle increases. Increasing the nanoparticle diameter results in increasing its volume; The increased volume results in an increase in the particle polarizability, thereby increasing the value of the optical extinction.

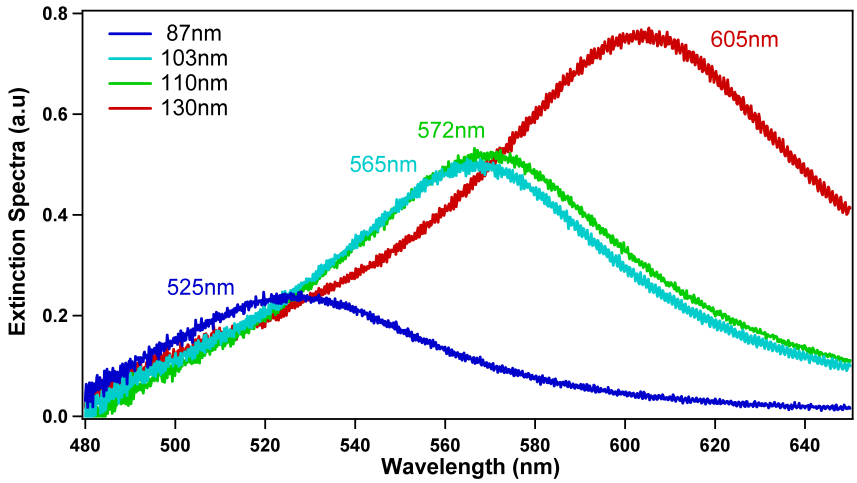

Figure 2.9: Extinction spectra of ordered arrays of silver nanoparticles.

- Effect of the nanoparticle distribution

EBL technique has been also used to fabricate patterns of random/disordered metal nanoparticles. The aim of the "random" distribution is to overcome the interaction that may occur in case of patterned nanoparticles. [70] A SEM image showing a "random" distribution of particles is presented in Figure 2.10.

The effect of the random distribution of particles on the resonance position has been studied for metal nanoparticles and is illustrated in Figure 2.11. Our study was done on silver cylindrical nanoparticles of 50-nm thickness and with diameter varying from 85 nm to 130 nm. In this way, the result of the present study can be compared to the one done in Figure 2.9, since all parameters were kept constant and the distribution of particles was the only varying parameter. Thereby, the difference in the resonance positions between Figures 2.9 and 2.11 is only due to the distribution of the particles in the pattern. We believe that since the distance between particles is different in both distribution, so particles do interact differently resulting in a different position of the resonance. [70]

- Effect of the nature of metal

The metal nature has been also studied to see its influence on the resonance position. To do this, the parameters have been chosen to be the same as for the study shown in Figure 2.9, meaning that the thickness of the particle was 50 nm, the side-to-side distance between two successive particles was 300 nm and the nanoparticle diameter was varied between 90 nm and 130 nm. The only difference

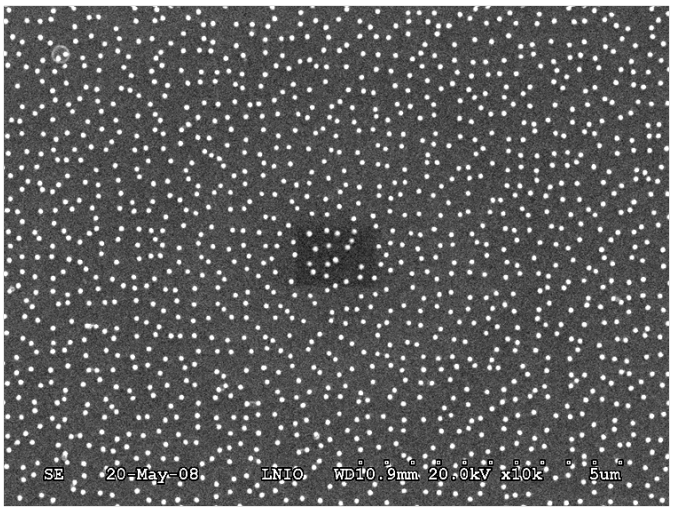

Figure 2.10: SEM image showing a random distribution of silver metal nanoparticles.

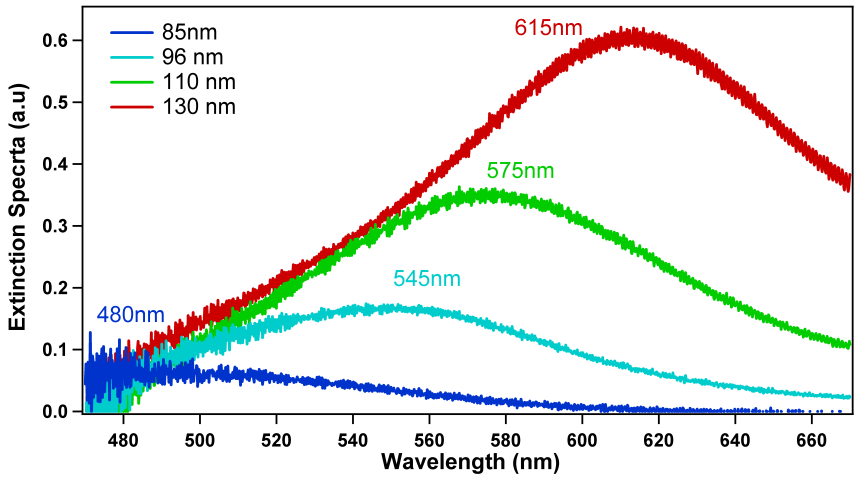

Figure 2.11: Extinction spectra of random arrays of silver nanoparticles.

between the present study and the one presented in Figure 2.9 is the nature of metal. Figure 2.12 shows the extinction spectra of gold cylindrical particles. Our results in Figure 2.12 confirms the literature [71] since the resonance of our fabricated particles lies in the red region compared to silver metal. While comparing the results of Figure 2.12 to those of Figure 2.9 where the resonances present peaks in the green region of the spectrum, we can obviously see the effect of the metal nature.

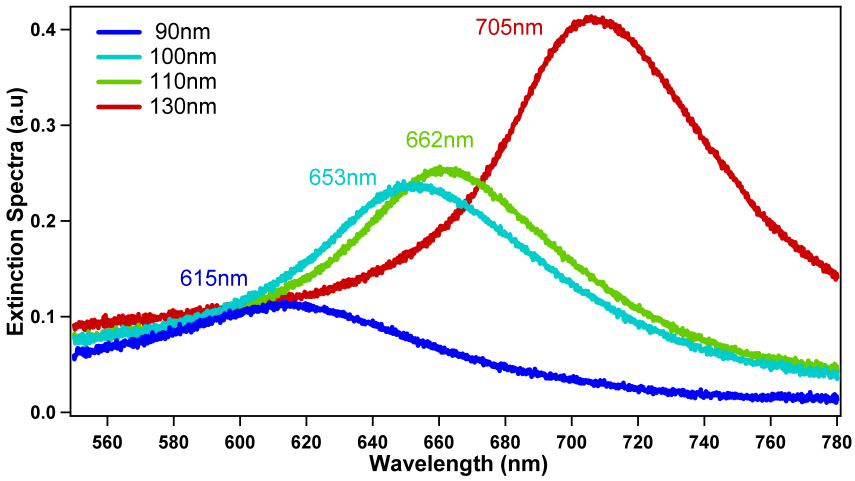

Figure 2.12: Extinction spectra of ordered arrays of gold nanoparticles.

Characterization by means of single particle scattering spectroscopy

Scattering spectra for single nanoparticles were also achieved on particles fabricated by EBL. These spectra were done at Dijon based on a collaboration with Alexandre Bouhelier at the "laboratoire Interdisciplinaire Carnot de Bourgogne". While extinction spectra give an average answer of the absorbed and scattered cross-sections of all particles in a pattern, scattering spectra of single particles highlight the response of each particle apart. This response is quite different depending on the chosen particle, that is why we expect a difference in the resonance positions of the particles even if they were fabricated during the same EBL technique. An example of single particle scattering spectra is shown in Figure 2.13 (a) and a typical SEM image, done at Dijon, is presented in Figure 2.13 (b). This figure illustrates the scattering spectra of ten different nanoparticles belonging to the same pattern. We believe that this difference is due to the disability to reproduce the exact shape, diameter, crystalline nature, etc. for all the particles on the substrate using EBL technique. This point is of great importance and must be taken into consideration, in the case we wish to address single nanoparticles.

2.4.2 Characterization of commercial colloidal nanoparticles

AFM Characterization

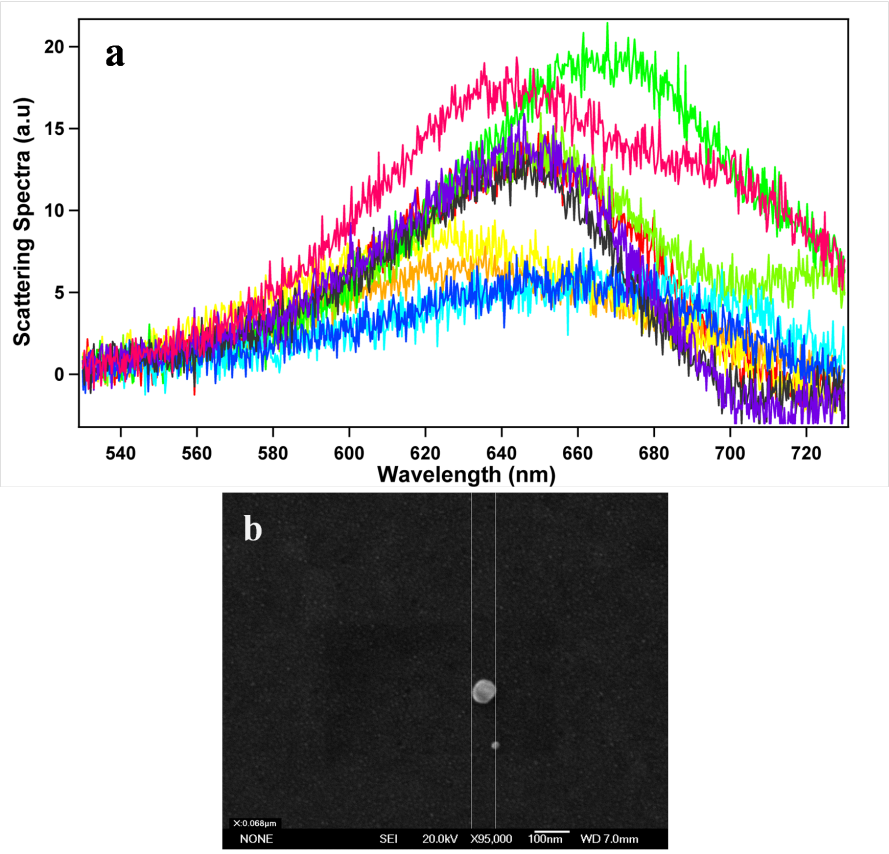

Figure 2.13: Single particle characterization. (a) Scattering spectra for ten different particles belonging to the same pattern. (b) SEM image.

After functionalization of the substrate and dip-casting it into the colloidal solution, we characterize it with an AFM. This VEECO microscope, with a Bioscope II stage and a Nanoscope controler V, was received in December 2008 and is financed by the "Agence Nationale de la Recherche" (ANR) under grant Photohybrid Blanc 07-02-188654. Figure 2.14 illustrates a typical AFM image of silver colloidal nanoparticles with 60-nm diameter, where panel (a) shows a 10x10 μm^2 region and panel (b) shows a zoom of 2x2 μm^2.

Absorption spectrum

In order to know the resonance position of the colloidal silver solution, an absorbance spectrum was done for a small volume taken from the solution then normalized with respect to the spectrum of water. The base line was taken for water because the later is the solvent of the colloidal solution. Figure 2.15 shows the

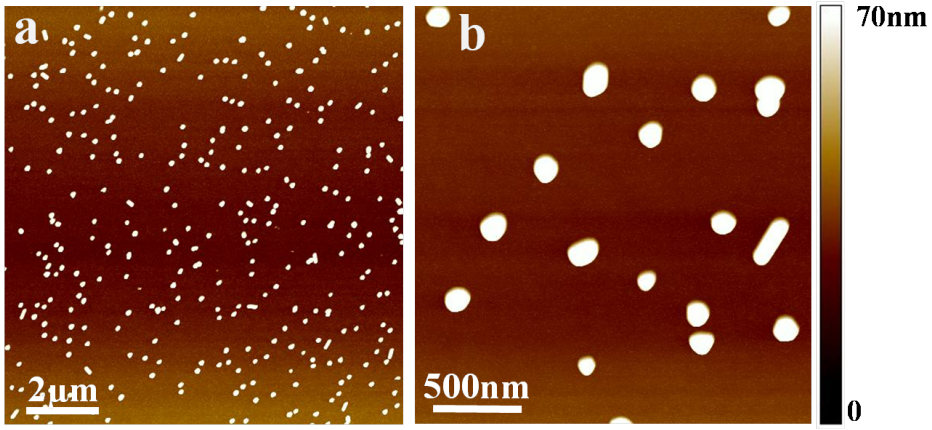

Figure 2.14: AFM images of colloidal silver nanoparticles. (a) 10x10 μm^2 and (b) 2x2 μm^2. The color bar shows the scale in Z-direction.

absorbance spectrum of silver colloidal nanoparticles of 60-nm diameter in water. The spectrum shows that the particles have maximum of absorbance at 452 nm.

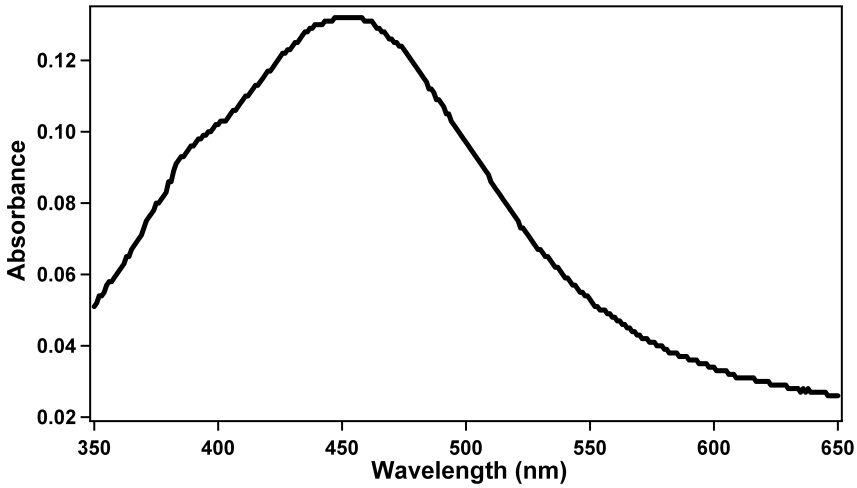

Figure 2.15: Absorbance spectrum of silver colloidal nanoparticles of 60-nm diameter in water.

After these parametric studies, we became more familiar with the optical properties of the chemically synthesized metal nanoparticles and the lithographic ones. These studies enabled us later to select the correct nanoparticle characteristics, including metal nature, nanoparticle diameter, nanoparticle height, for the sake of

our experiments.

Before going through the details of the main part of this work, *i.e.* photopolymerization triggered by the optical near-field of metal nanoparticles, we still need to understand the properties of the chemical solutions we are using, and their reaction mechanism. For this reason, we decided to dedicate the rest of this chapter to explain the principle of photopolymerization of the different photosensitive formulations and to characterize them.

2.5 Preparation and photopolymerization principle of different photosensitive solutions

Photopolymerization processes consist of initiating a polymerization reaction by means of a light beam. Whilst the liquid material solidifies in the irradiated areas, non-irradiated ones remain unchanged and can be washed out by a suitable solvent. [72, 73, 74] Coupling of photopolymerization with an experimental setup allows us to shape and vitrify a polymer part. [73] This method, called photolithography, can be used in data storage devices where information is addressed by holographic methods, mask projection, or pixel by pixel scanning.

2.5.1 Organic photopolymerizable solution

Composition

The used photopolymerizable formulation was developed by our collaborators "Olivier Soppera *et al.*" at Mulhouse at the "Institut de Sciences des Matériaux de Mulhouse" and was introduced in many papers. [48, 72, 73] It is made up of three basic components as illustrated in Figure 2.16: a sensitizer dye, a co-synergist amine, and a multifunctional acrylate monomer, pentaerythritol triacrylate (PETIA). PETIA is used as received from the supplier and forms the backbone of the polymer network.

The co-synergist was the methyldiethanolamine (MDEA) and the Eosin Y (2',4',5',7'-tetrabromofluorescein disodium salt) was used as the sensitizer dye. This system was developed mainly because of its high sensitivity in the spectral region from 450 nm to 550 nm with a maximum of absorption at 532 nm. In addition, this liquid system is very flexible as it is possible to modify the components independently to adjust the physical and chemical properties of the formulation,

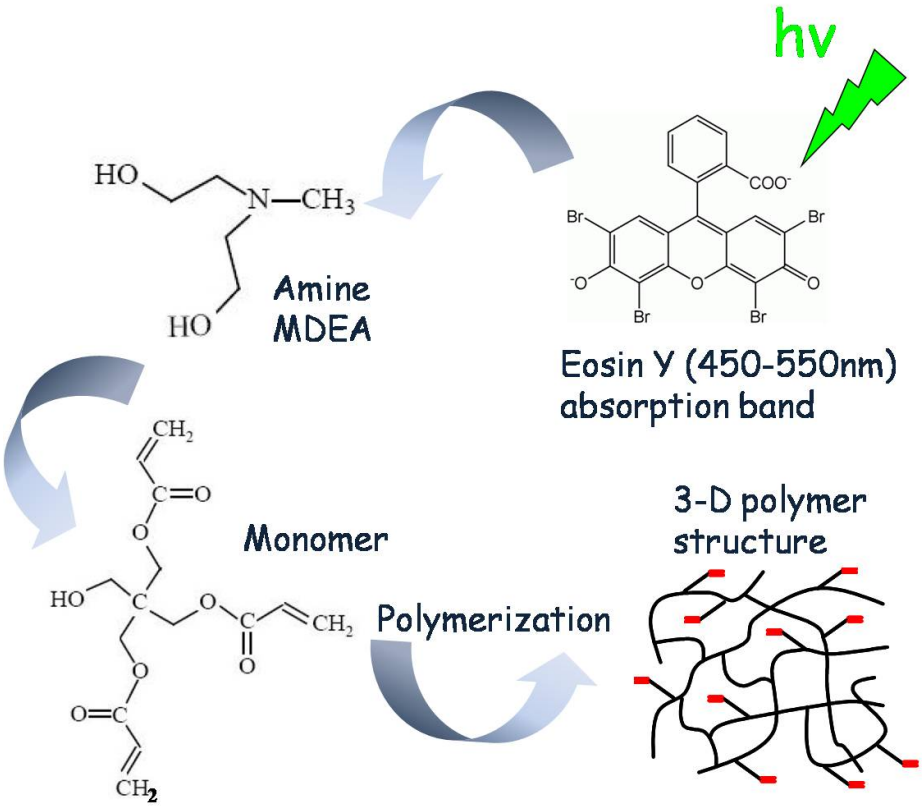

Figure 2.16: Scheme showing the three components of the photopolymerizable solution together with the photopolymerization process.

namely viscosity, spectral sensitivity, polymerization threshold, energy. The results reported in this chapter were obtained with mixtures containing 0.5 wt % of Eosin and 4 wt % of MDEA, unless mentioned differently. To be able to work with gold nanoparticles and with much larger silver metal nanoparticles, we replaced the photosensitizer by another dye, Methylene Blue, to ensure absorption in the 600-nm range. The absorption spectrum of this dye goes from 440 nm to 710 nm with a maximum of absorption at 650 nm.

Photopolymerization principle and reaction mechanism

Upon the absorption of actinic photons, Eosin is promoted to its singlet state; then, it is converted to its triplet state that undergoes photoreduction by reaction with the amine electron donor (MDEA). The corresponding amine-derived free radicals are now able to initiate polymerization of acrylic monomers. As a result

of the propagation and termination steps, the liquid formulation gets converted into a cross-linked polymer, that is a 3D-structure. Reactions involving radicals are highly sensitive to oxygen quenching, [73, 75, 76] leading to an inhibition period. During this period, photons absorbed by the dye, to create radicals, react primarily with dissolved O_2 until reaching a low O_2 concentration, thus allowing the polymerization reaction to begin and reach a degree of development enabling subsequent characterization. The amount of energy absorbed by the chemical solution at this stage is defined as the threshold energy. [77] Silver metal nanoparticles were used with this type of formulation because a spectral overlapping between dye absorption and SPR of the metal nanoparticles embedded in liquid polymer can be achieved. A simplified scheme [78] illustrating the main steps of photopolymerization reaction and the quenching processes during irradiation is presented in Figure 2.17.

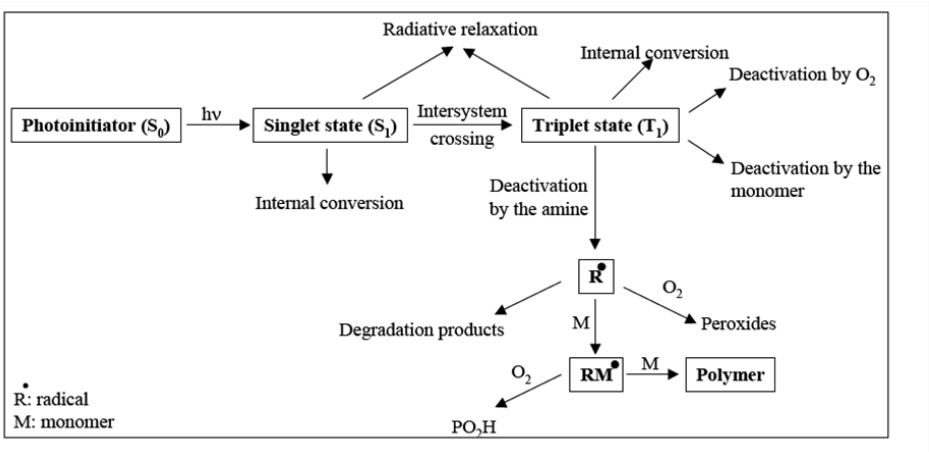

Figure 2.17: Reaction scheme of photopolymerization processes. (Reprinted with permission from Fouassier, J. P. (1995). Copyright 1995 Hanser Publishers)

It must be noted that we used to utilize 8% as a concentration of amine; yet we recognized that MDEA hangs on the metal particles and therefore creates a basic medium in their vicinity. Eosin Y is sensitive to the pH of the medium and flees the basic places, so we reduced the concentration of amine from 8 wt % to 4 wt %. We choose this new concentration based on Figure 2.18 that illustrates the influence of the concentration in weight of MDEA on the threshold time of the solution. While looking at this figure in details, we notice that decreasing the MDEA concentration from 8 wt % to 4 wt % has almost no influence on the solution threshold time.

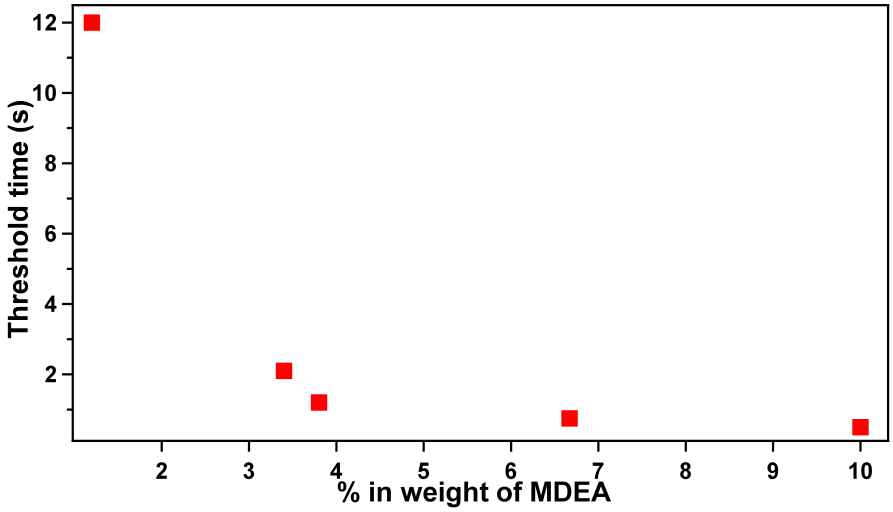

Figure 2.18: Influence of the concentration in weight of the amine on the formulation threshold time.

2.5.2 Hybrid sol-gel formulation

In the context of the "Photohybrid" project, a formulation of hybrid sol-gel materials, photopolymerizable with visible wavelengths, was also developed. Photoassisted hybrid sol-gel processing has gained special interest during the last years since it allows the formation of hybrid organic-inorganic materials by acid- or base-catalyzed hydrolysis and condensation of main group or transition metal alkoxides. [79] The photochemical processing brings some specific advantages such as low temperature and spatial control of the polymerization reaction for photolithographic applications. [80]

Compared to organic photopolymers, hybrid sol-gel materials are much more appropriate to prepare thin films ($< 1\mu m$). Indeed, the presence of SiOH moieties favors the adhesion of the film with substrates such as Si or SiO_2, preventing dewetting. Moreover, the possibility of doping the material with Titanium or Zirconium alkoxides allows tuning the refractive index. [81] The precursor used in this formulation is methacryloxypropyltrimethoxysilane. The inorganic part of the hybrid precursor is a trimethoxysilane. This function reacts with water to create siloxane chains that form the backbone of the material. The organic part is a methacrylate functionality that can be polymerized using an appropriate initiating system. The hardening of the material occurs during irradiation. To avoid

any phase separation that would lead to an opaque material unsuitable for optical applications, both organic and inorganic parts are covalently linked by a Si-C bond that remains stable under synthesis conditions. Since the elementary bricks composing the final materials are molecules, one can expect nanoscale resolution for such materials. They are thus potential negative resists for nanoscale patterning.

2.6 Interferometric setup based characterization

2.6.1 Experimental setup

The experimental setup used to characterize the solutions is shown in Figure 2.19. The actinic light was provided by a Nd:YAG laser; the selected wavelength 532 nm lies in the absorption spectrum of Eosin (this laser source is replaced by He:Ne at 633 nm when methylene blue is used as a dye). The laser beam is first coupled in a single mode optical fiber. At the second end of the fiber, the laser beam is quite filtered, cleaned and presents a gaussian profile. This end of the optical fiber is placed at the focal distance of an objective with 0.12 numerical aperture (NA) to ensure a parallel laser beam after this latter leading to a 1-cm collimated circular beam. After crossing a beam splitter, both monochromatic and coherent beams are reflected on two mirrors to finally interfere and create an interference pattern of bright and dark fringes at the sample stage. To control the final polarization of the laser beam, a polarizer is placed just before the cube splitter. Another laser source, whose wavelength does not lie in the absorption spectrum of the dye, is used to follow in-situ the creation of the grating and to detect the decay of the zero-order diffraction power. This "reading" source has a wavelength of 633 nm when Eosin Y has been used as a dye, and 1300 nm for methylene blue.

2.6.2 Results on the photochemical system using Eosin Y as dye

In order to perform precise characterization of the polymer gratings of micron and sub-micron size, we used AFM mainly in intermittent contact mode, or what we used to call "tapping mode". The gratings of polymers were recorded by the holographic set-up described above and their thicknesses were extracted from the AFM profile sections. Figure 2.20 shows AFM images of polymer gratings obtained for different time of exposure.

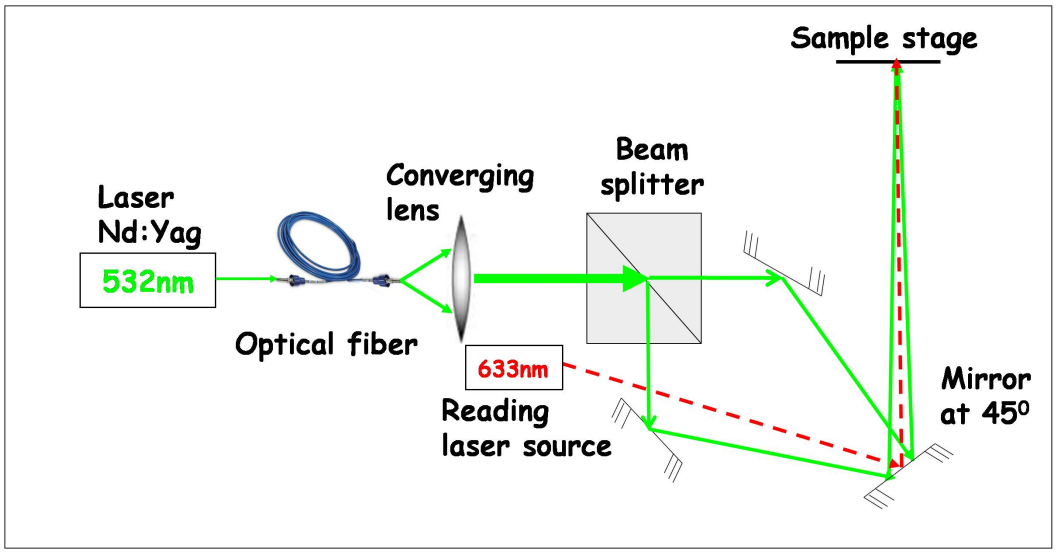

Figure 2.19: Scheme showing the interferometric experimental setup used to characterize the photosensitive solutions.

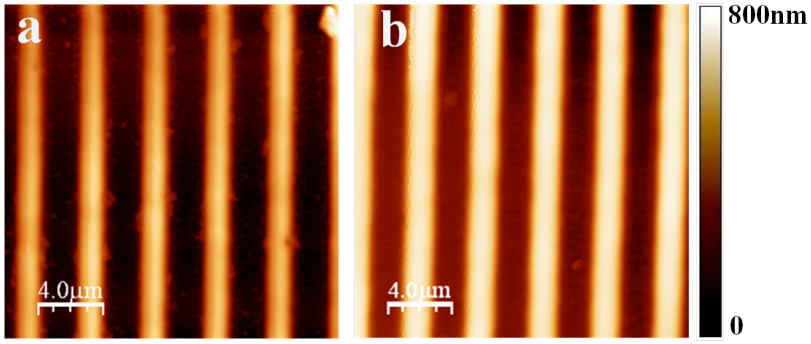

Figure 2.20: AFM images of polymer gratings obtained at P = 1 mW and t = 1.125 s (a) and 1.7 s (b).

To better understand of the response of our photochemical system when exposed to light, several experiments have been carried to illustrate the influence of the incident power, the exposure time, the diffusion of oxygen, the diffusion of dye, etc. on the fabricated gratings. All the achieved studies must be interpreted on the basis of comparing the incident power, represented by the number of photons per second received by the sample, to the diffusion speed of oxygen. As we said previously, the chemical process does not start unless the concentration of oxygen in the medium becomes much smaller than that of the formed radicals. Indeed, before reaching the threshold dose, the incident photons absorbed by the sample

react primarily with the dissolved O_2 present in the chemical drop volume. When the number of dissolved oxygen molecules is low enough, the polymerization reaction starts. Yet the regions receiving the incident light (what we call the bright regions) have now lower concentration in oxygen, that is why O_2 starts diffusing from the non-irradiated regions (dark regions) to the irradiated ones. If the rate at which the photons received by the sample is greater than the rate of diffused O_2, photopolymerization starts. However, if the rate of photons is smaller than that of oxygen, the chemical process will never start since all radicals are transformed to peroxides by means of O_2, as we can see in Figure 2.17.

Figure 2.21 summarizes an achieved study, in which we aimed to reveal the influence of the exposure time (at constant power) and that of the incident power (at constant exposure time) on the growth of the grating. Both curves in this figure were done at constant dose so that we will be able to compare them. It should be stressed that during this study the distance separating two successive bright fringes was kept constant, 4.3 μm. This implies that the reservoir of oxygen (see Section 2.5.1 that highlights the importance of oxygen) in the dark regions is constant for all the values appearing in Figure 2.21.

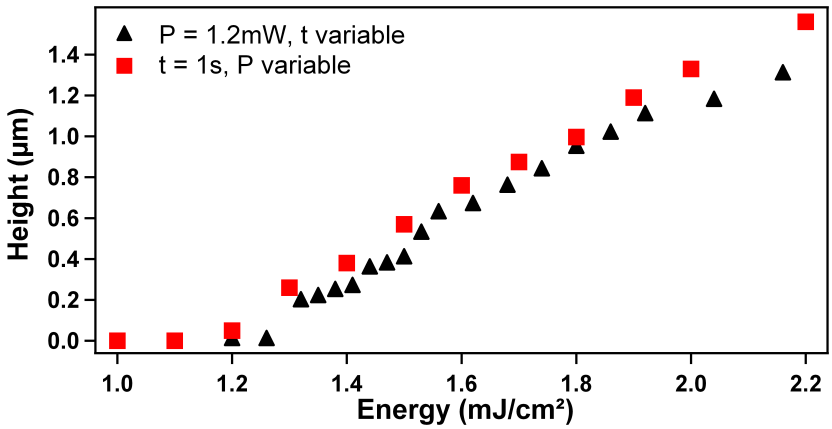

Figure 2.21: Influence of the incident power and the exposure time on the grating growth at constant dose.

Figure 2.21 clearly illustrates that the grating height in case of the red curve (t = 1 s, P variable) is always greater than that in the case of the black curve (P = 1.2 mW, t variable). As a matter of fact, this is due to the number of photons per second received by the sample and hence the number of radicals created. For a constant dose, say 1.5 mJ/cm^2, the power and the time of the red curve are

1.5 mW and 1 s, respectively, while those of the black curve are 1.2 mW and 1.25 s, respectively. This means that for a constant dose, the number of photons per second received by the sample in the case of the red curve is higher than that received in case of the black curve. Comparing the number of photons per second received by the sample in both cases to the constant rate of oxygen diffusion since the reservoir of oxygen in the dark region is the same (same grating period for both curves), we notice that more radicals are fabricated when this number increases. This implies that the chains of polymer are longer which induces more polymerization and hence leads to a higher grating height (case of the red curve). It must be noted that the threshold dose can be deduced from the curves illustrated in Figure 2.21. This parameter is defined as the value of the dose for which the height of the grating starts to be slightly greater than zero, meaning 1.25 mJ/cm^2 for the red curve and almost 1.3 mJ/cm^2 for the black curve.

To clarify the influence of the oxygen diffusion on the process of photopolymerization, a study as a function of the grating period has been achieved. Modifying the grating period changes the reservoir (number of molecules) of O_2 present in the dark fringes and hence its diffusion into the bright fringes is altered. Figure 2.22 shows the result of this study. Three different order of power were chosen (1.6 mW, 1 mW and 0.4 mW) intentionally so that the number of photons per second received by the sample is varied dramatically. In this way, we can understand the influence of the grating period on the threshold time for each range of power. This figure shows the evolution of the height of the grating polymer over its period and it summarizes a competition between the number of radicals created and the number of the O_2 molecules present in the medium.

For high powers, it is evident to reach the threshold rapidly since the number of incident photons per second is creating a huge number of radicals. Thereby, even if the consumed oxygen in the bright region is replenished from the dark regions, the rate at which the photons are reaching the sample is much larger than that of the diffused oxygen. This will immediately launch the polymerization process and hence the threshold time is small. While for low powers, the polymerization process needs much more time to start, since the rate of the incident photons received by the sample starts to be comparable to the rate of oxygen diffusion. This is confirmed by our results, black and red curve on Figure 2.22, respectively.

While the incident power is set at 1.6 mW (black curve on Figure 2.22), the corresponding threshold time is not influenced by the variation of the grating period. This can be understood by the fact that at this high power, the dominant

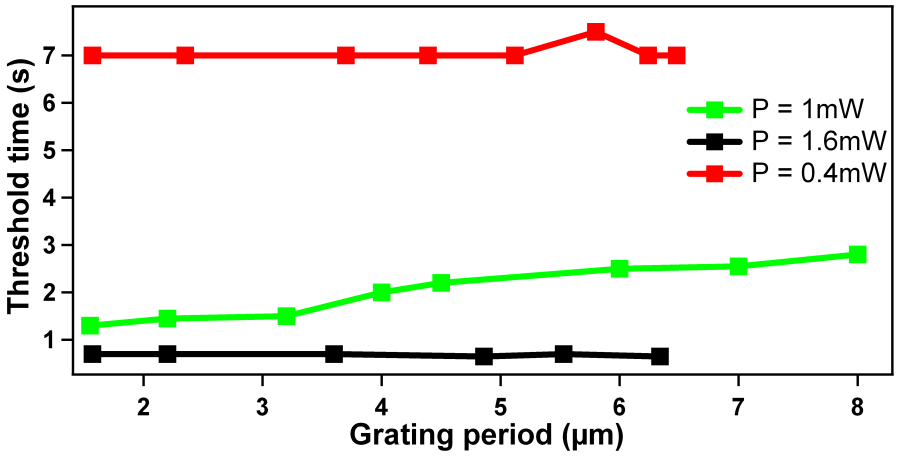

Figure 2.22: Influence of the grating period on the threshold time for three incident powers.

factor is the number of created radicals (which is proportional to the number of incident photons per second) and not that of O_2 molecules. This implies that the increase of the volume of the reservoir of oxygen will not affect the threshold because the number of radicals in the medium is already large. Indeed, the number of photons per second is too high to an extent that the oxygen does not have the time to diffuse from the dark regions and hence we are always dealing with the same number of molecules present in the bright regions.

When the incident power is fixed at 0.4 mW (red curve on Figure 2.22), we also notice that the variation of the grating period does not affect the threshold time. This is explained as, at this power, the number of created radicals per second is low but still sufficient to launch the photopolymerization. Additionally, the rate of coming photons per second is roughly higher when compared to the O_2 diffusion rate, thus oxygen has sufficient time to diffuse from dark regions and hence polymerization needs 7 s to start. Increasing the grating period, which leads to an increase in the reservoir of oxygen in the dark regions, does not affect the threshold time since oxygen has already diffused to the bright regions even for small periods. This implies that at this power and whatever the period is, the formed radicals are competing with the O_2 molecules already present in the bright regions and the ones diffusing from the dark fringes.

When the incident power is chosen to be 1 mW (green curve on Figure 2.22)),

we can remark the impact of the grating period on the threshold time. This curve reveals an excellent example on the competition between the number of radicals and that of O_2: When the reservoir of oxygen is larger, the number of radicals is no more sufficient to trigger photopolymerization during the same time; So the number of radicals needs to be higher that is why the chemical process is delayed and the threshold time is greater.

Another method for characterizing the polymer gratings has been also developed. This method relies on the study of the grating optical response in real time, through the variation of the refractive index $\triangle$n during polymerization. This index variation is associated with a phase grating detected through measurement of the diffraction efficiency of the formed grating with the use of a probing laser beam. During the process of polymerization, the change in the rate of conversion leads to a variation in the refractive index of the polymer which increases from 1.485 for the monomer liquid to 1.52 for the cross-linked polymer.

Figure 2.23 shows an example of a growth curve for a holographic polymer grating; it represents the diffraction efficiency as a function of the recording time t. The power of irradiation for this solution, containing 0.05% as Eosin concentration, was 2 mW. Four regions can be distinguished on this curve:
- Period of inhibition, shown in Figure 2.23 (b), during which there is consumption of the dissolved oxygen in the formulation. During this period, the threshold dose is not yet attained.
- Period of growth during which the formation of the polymer grating starts and its thickness increases.
- Period of stabilization.
- Period of slow decay, where there is an over exposure of the grating which leads to a decrease in the thickness of the grating and hence a loss of diffraction.

The curve in Figure 2.23 (b) shows a threshold value. This figure can be used to determine the threshold of polymerization before passing through rinsing procedure (that will eliminate the non-reticulated solution).

This technique of characterization was also used to study the influence of the incident power and that of the oxygen on the polymerization process. The decrease in the incident intensity slows down the dynamics of the polymer grating fabrication and hence increases the threshold of polymerization. Under certain conditions, we may reach a regime of non-polymerization ($I_{max} = 0.04$ mW in Figure 2.24); at this level, the competition between the polymerization process and the inhibition of oxygen is so crucial. Figure 2.24 shows a strong dependence of the threshold energy and the rate of grating formation on the incident power.

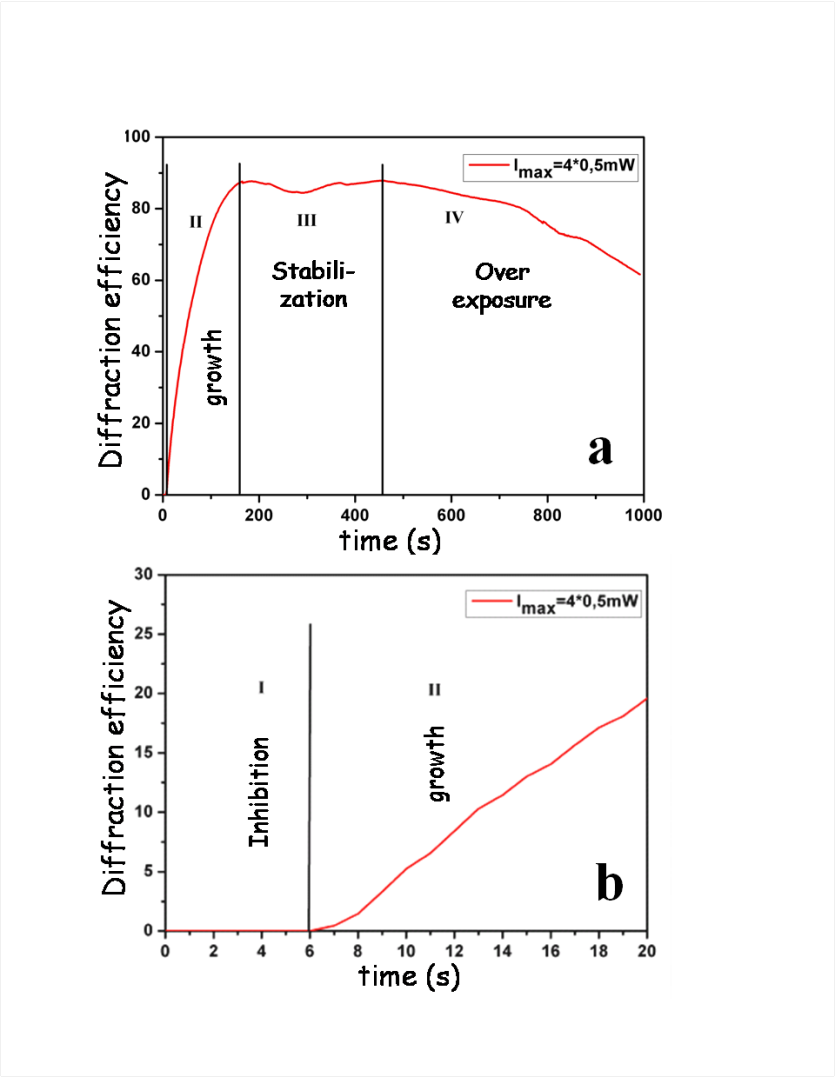

Figure 2.23: Example of a growth curve for a holographic polymer grating. a) Full curve illustrating the diffraction efficiency as a function of the recording time. b) Zoom done on the zone I and II of panel (a).

Figure 2.25 illustrates the dependence of the threshold dose, extracted from Figure 2.24, on the incident power. The curve shows two regimes of photopolymerization:

- Area of reciprocity power/threshold time: in this zone, the threshold time is inversely proportional to the incident power.

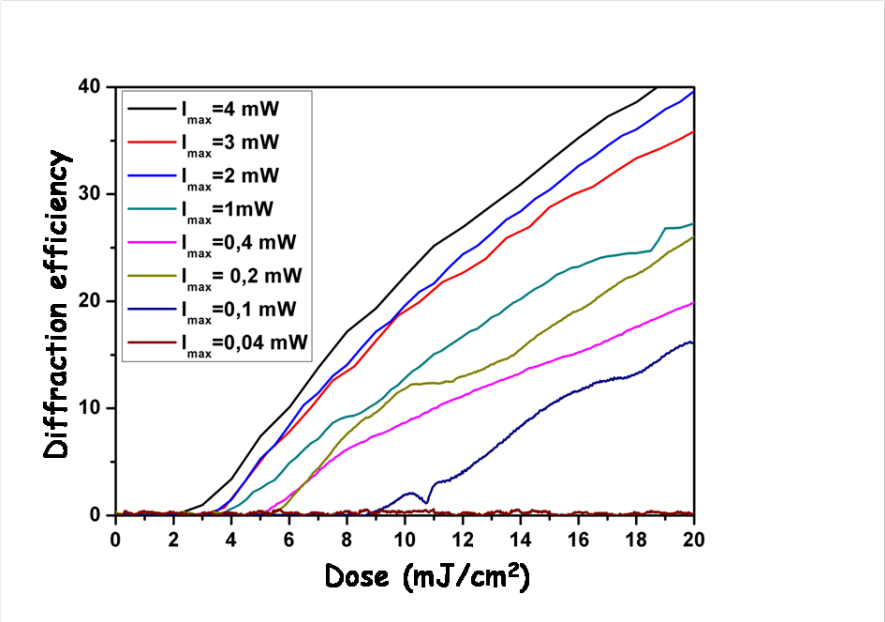

Figure 2.24: Study of the influence of the incident power on the dynamic of the polymer grating formation.

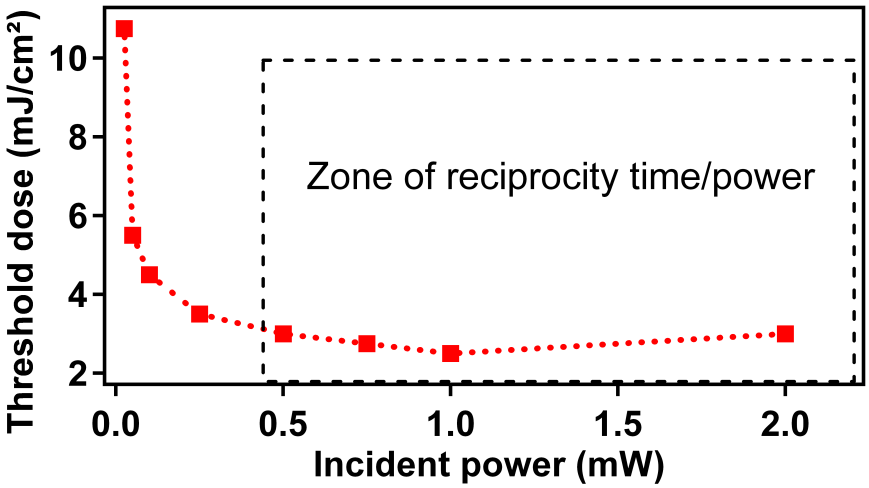

Figure 2.25: Evolution of the threshold dose of photopolymerization as a function of the incident power.

- Area of non-reciprocity where the threshold time and the power do not vary according to the same factor.

Indeed, in the area of reciprocity, a decrease of power requires an increase of

irradiation time by a identical factor to consume the oxygen within the drop.

In the area of non-reciprocity, the incident power is not high enough to consume all the O_2 molecules present in the chemical drop, in addition to the diffusion of oxygen from the ambient atmosphere which continuously replenishes irradiated areas (always assumed to be neglected for millimetric drops). Thus, more time is obviously needed to consume this amount of oxygen. Figure 2.25 shows also a zone, lower than 0.2 mW/cm^2, for which no polymerization can happen whatever the irradiation time is. As a matter of fact, the photochemical reaction does not consume all the oxygen introduced by diffusion to initiate polymerization, which means that the number of incident photons per second is not enough to compensate the existing molecules of O_2.

2.6.3 Results on the photochemical system using Methylene Blue as dye

The photochemical system using the Methylene Blue as a dye was also characterized to determine its threshold dose. Figure 2.26 shows AFM images of polymer gratings obtained during different times of exposure. While the incident power was set at 800 μW, we measured the thickness of the polymer grating for different irradiation time.

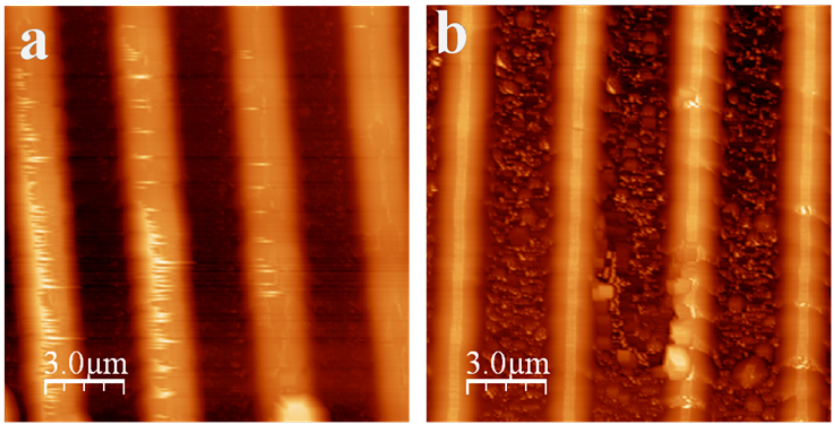

Figure 2.26: AFM image showing polymer gratings obtained for different exposure times. (a) 2.5 s, (b) 2 s.

Figure 2.27 shows the evolution of the amplitude of the polymer grating as a function of the exposure time. The threshold time can be deduced from Figure 2.27, which is about 1.85 s. This parameter was also determined by another characterization method, the diffraction efficiency one, and was found equal to 2

s. Both methods of characterization developed by our group reproduce faithfully the threshold of polymerization of the photochemical solution. The approach of plasmon-based nanophotopolymerization relies on the precise knowledge of the threshold.

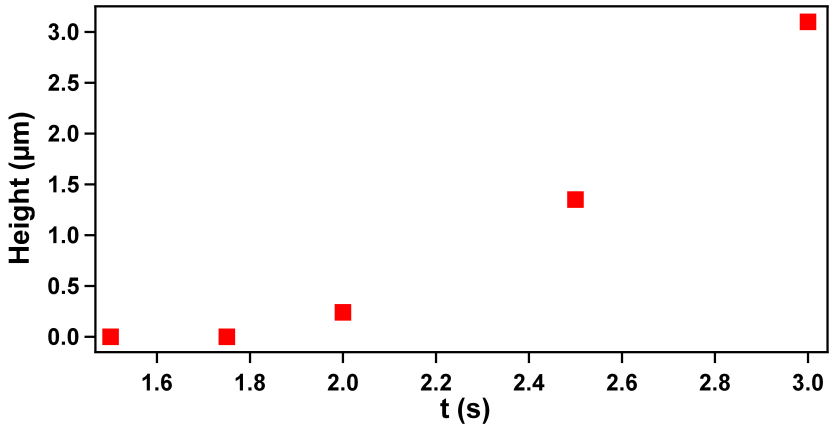

Figure 2.27: Evolution of the polymer height as a function of the irradiation time.

2.7 Focused laser beam setup based characterization

2.7.1 Experimental setup

The new experimental setup is represented in Figure 2.28. This setup has been developed after receiving the equipments (Ar:Kr laser source, inverted optical microscope, AFM, etc.) financed by the ANR, under grant Photohybrid (BLANC 07-2-188654).

The actinic light is delivered by a multi rays, ranging from 454 nm to 647 nm, Ar:Kr laser source that is first coupled in a single mode optical fiber; Coupling in the optical fiber guarantees a quite filtered, cleaned and presenting a Gaussian profile laser beam. The beam is then collimated by means of an objective with 0.12 as NA. As mentioned previously, the chosen incident wavelength should lie in the absorption spectrum of the dye of the chemical formulation. The beam is then reflected through a couple of mirrors, passes through a polarizer to adjust its polarization, and is finally coupled with an optical inverted microscope Olympus Ix71. Prior to the optical microscope, a 50/50 beam splitter is utilized to reflect part of the beam to an optical powermeter so that the power of the excitation

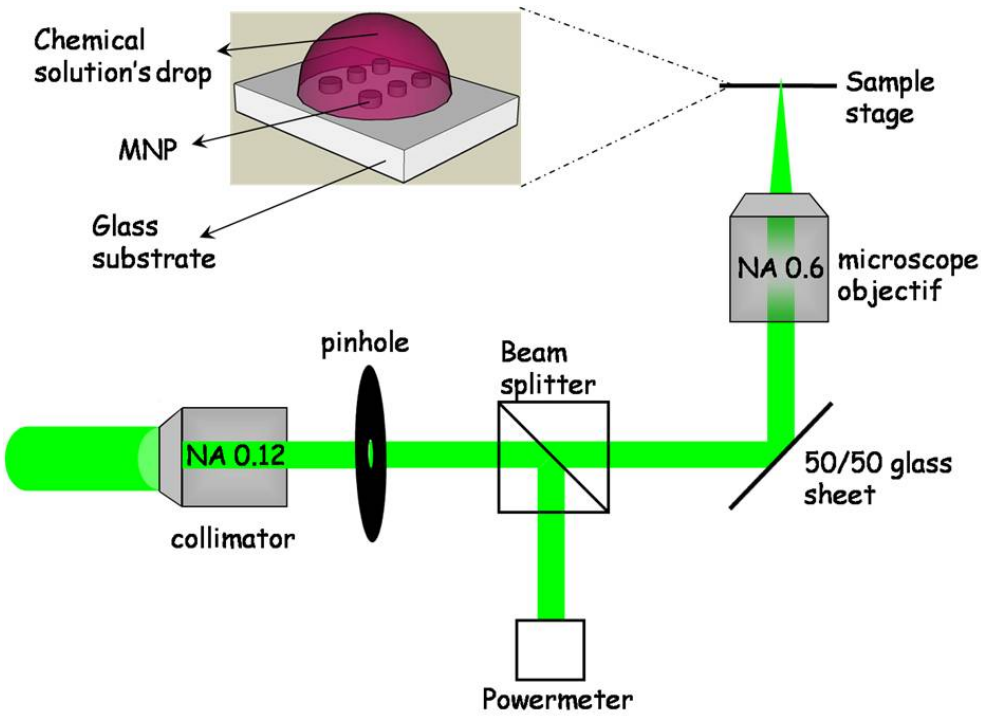

Figure 2.28: Newly developed experimental set-up. (Reprinted with permission from Deeb, C. *et al.*, Proc. of SPIE, 7395, 739505-1 (2009). Copyright 2009 SPIE).

beam is constantly monitored for any fluctuation. After a 0.6 NA objective, the diameter of the laser spot at the level of the sample stage can be adjusted between 3 μm and 8 μm, by placing a pinhole through the path of the laser beam (ref. Figure 2.28). Obviously, the diameter of the spot can be reduced more by increasing the NA of the microscope objective; with 1.45 NA, we reached 250-nm as diameter spot.

A He-Ne laser beam, with 633-nm wavelength, was also coupled in the inverted optical microscope and aligned with the actinic beam. The coupling of this laser offers a reference about the exact position of the Ar:Kr laser spot, even with the presence of the photo-sensitive formulation. The initial stage of the inverted optical microscope was replaced by a motorized stage of an AFM, Veeco Bioscope II. The optional AFM (with a moveable head) is also coupled to the optical microscope and is monitored by means of a Nanoscope V controller and an electronic box. The wavelength of the laser beam of the AFM is at 805 nm, meaning that the absorption of our dye will not be influenced by it.

Using this new experimental setup, an exposure for a group of metal nanoparticles can be established, then by moving the motorized Veeco stage, a second exposure with different irradiation parameters (power, time, wavelength, etc.) may be achieved. Using an appropriate microscope objective, we can also irradiate a single metal nanoparticle. During this PhD work, the focalized laser beam was not use to achieve nanophotopolymerization, yet we used it for the characterization of the chemical solutions, as we will see in the upcoming section.

2.7.2 Characterization of the chemical formulations

Chemical solution using Eosin Y as a dye

In order to characterize this photosensitive solution using a focalized laser beam, we fully studied it using the experimental setup described in the previous section. As already mentioned, we define the threshold energy as the amount of energy absorbed by the chemical solution that allows for the polymerization reaction to begin and reach a degree of development enabling subsequent characterization. The threshold energy is therefore not an absolute quantity and has to be defined on the basis of the performed experiment. Two approaches were followed for the deposition of the chemical drop: the first is a drop cast one and the second is a drop cast followed by a passage of a graduated roller to get a film of 10-μm thickness. All results shown in this section were done on a mixture of 4 wt % MDEA and 0.5 wt % of Eosin Y. The used wavelength was 514 nm.

- Drop cast approach: This approach consists on depositing a drop of the chemical solution on a glass substrate, then doing a series of exposures with a laser spot of 2-μm diameter, one next to the other by means of the motorized sample stage. After exposure, the sample is rinsed in a bath of ethanol followed by a bath of isopropanol. Figure 2.29 shows optical images illustrating the fabricated polymer tips on the surface of the glass.

Panel (a) of Figure 2.29 shows polymer tips made up with P = 650 nW and during t = 1 s, while those of panel (b)were fabricated with P = 300 nW and during t = 1 s. The threshold dose was found to be P = 300 nW and during t = 0.5 s. The effect of the incident dose on the length and the diameter of the tips is elucidated by comparing panel (a) and panel (b). As we can see on the optical images, the section of the base on which the polymer tip is resting is small compared to its height, this is the reason for which they were not able to stand up on the glass surface. It should be noted that the volume of the drop is the main reason for which the height of the polymer tips is high. This was already noticed by Bachelot

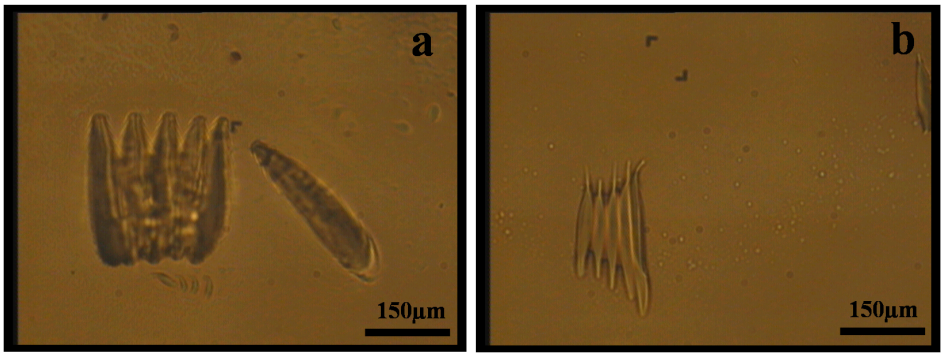

Figure 2.29: Optical image showing polymer tips on the surface of a glass substrate. The parameters of irradiation are P = 650 nW and t = 1 s for panel (a), and P = 300 nW and during t = 1 s for panel (b).

et al. in the case of integrating micrometer-sized polymer elements at the end of optical fibers by free-radical photopolymerization. [76] During their experiments, the group showed that even for shortest exposure, the length of the integrated tip on the fiber core is equal to the drop height. The only two differences between the experiments done in this paper [76] and our experiments is the profile of the electric field and the volume of the formulation drop which is millimetric in our case (and this is why polymer tips are much longer here).

- Drop cast approach followed by the passage of a 10-μm roller: The only difference between this approach and the above one is the passage of a graduated 10-μm roller on the chemical drop after depositing it. This reduces the volume of the drop and transforms it to a film of polymer of 10-μm thickness. In figure 2.30 (SEM image), we show several polymer tips obtained at different incident power of the actinic green light. These tips are still long enough so that they are not able to stand up on the surface of the glass, although we reduced the volume of the drop to a film of 10-μm thickness; this time the length of the polymer tips is due to the high incident power.

When the incident power is decreased, we noticed that the length of the tip is also decreased. This is confirmed in the SEM image, Figure 2.31, which illustrates the influence of the power and the irradiated time on the length of the fabricated tips: As we increase the laser energy, the length and even the diameter of the polymer tip increases also. Near the threshold energy, we made polymer tips able to resist and to stay up even after the rinsing process. From Figure 2.31,

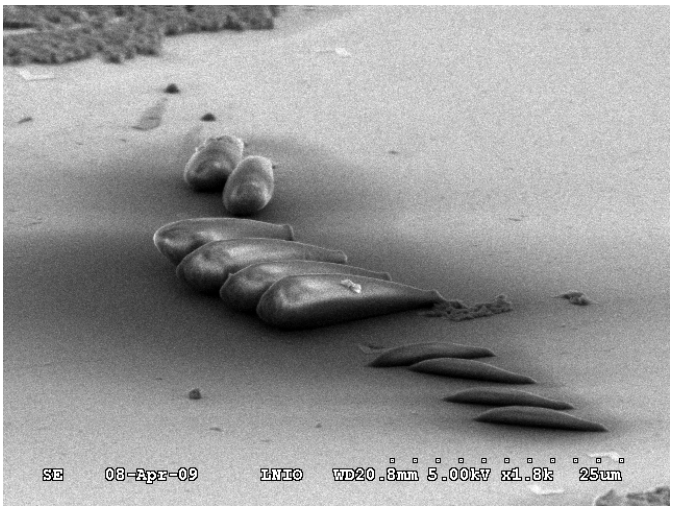

Figure 2.30: Influence of the laser dose on the fabricated polymer tips. The two first polymer tips (upper left corner) were fabricated with a power of P = 650 nW. From the third till the sixth polymer tip, we used P = 500 nW, and the four last tips were done with a power of 400 nW. The time was fixed at t = 1 s. (Reprinted with permission from Deeb, C. *et al.*, Proc. of SPIE, 7395, 739505-1 (2009). Copyright 2009 SPIE).

the threshold dose may be deduced. Indeed, a third line of exposure was done at P = 300 nW and t = 0.5 s; since this dose was below the threshold one, no polymerization took place. So the threshold parameters are P = 300 nW at t = 1 s (i.e $D_{th} = 7500$ mJ/cm^2).

Chemical solution using Eosin Y as a dye with 5 wt % inhibitor

A new solution has been developed with 5 wt % of inhibitor, while the concentrations of amine, monomer and dye were kept constant. The used inhibitor was the 4-methoxyphenol reagent, $C_7H_8O_2$. This solution has been introduced because we believe that during the process of photopolymerization, the radicals will be attacked by the oxygen and by the inhibitor, which may give better resolution to our fabricated polymer tips. Figure 2.32 shows a SEM image of polymer tips fabricated using the new chemical formulation, following the drop cast aspect then using the 10-μm graduated roller.

The polymer tips columns shown in the SEM image were made with P = 4 μW and during t = 1 s, 1/2 s, and 1/4 s, going respectively from the right of the SEM image to its left. A fourth column at the left of the image was illuminated

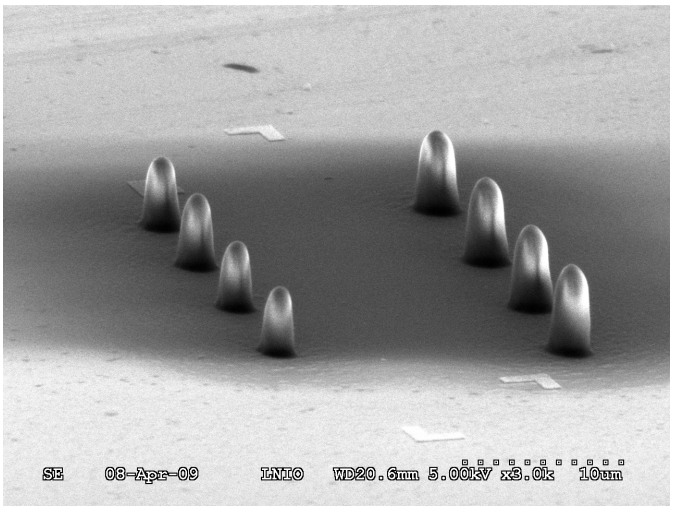

Figure 2.31: Influence of the laser energy on the length of the polymer tips near the threshold dose. The power for those polymer tips is kept constant (P = 300 nW). The time was 2 s for the right tips and 1 s for the left ones. (Reprinted with permission from Deeb, C. *et al.*, Proc. of SPIE, 7395, 739505-1 (2009). Copyright 2009 SPIE).

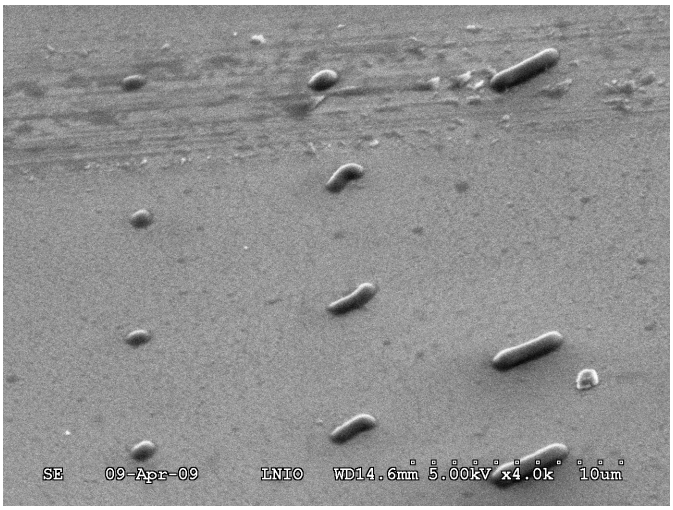

Figure 2.32: SEM image showing polymer tips fabricated by adding to the basic solution 5 wt % of inhibitor. The irradiation parameters were P = 4μW for t = 1 s, 1/2 s, and 1/4 s, going respectively from the right of the SEM image to its left.

with P = 4 μW and during t = 1/8 s; since no polymer tips were fabricated with these parameters, we can thus deduce the threshold parameters that are P = 4 μW for t = 1/4 s (i.e D_{th} = 25 000 mJ/cm^2). This figure clearly illustrates that the

resolution of the newly fabricated polymer tips has been improved with respect to the previous tips presented in Figure 2.30 and 2.31. It must be also noted that their size is even much smaller; We reached a size of $\sim$ 900 nm for the polymer tips presented at the left of Figure 2.32.

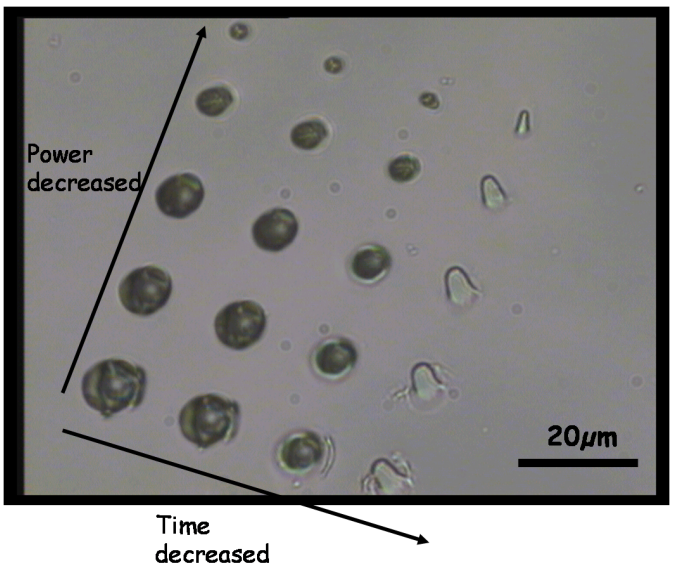

Figure 2.33: Optical image illustrating the influence of the laser energy on the length of the polymer tips. The power was varied between 3.54 μW and 0.33 μW, while the time was varied between 10 s and 0.1 s. (Reprinted with permission from Deeb, C. *et al.*, Proc. of SPIE, 7395, 739505-1 (2009). Copyright 2009 SPIE).

Hybrid Sol-gel

We have also characterized the sol-gel solution using the experimental setup described in section 2.7.1. The main aim of the several studies achieved on this spin-coatable solution was to be familiar with it and to determine the threshold energy for which the polymerization process starts. Relying on this parameter key, we will be able to accomplish a nanoscale photopolymerization as we will see in Chapter 3.

Figure 2.33 shows an optical image in which the influence of two parameters has been studied: the power of the actinic light and the time of the exposure. When the power is decreased, the time was kept constant and vice versa; whenever the power or the time is decreased, the size of the polymer tip is smaller. The most

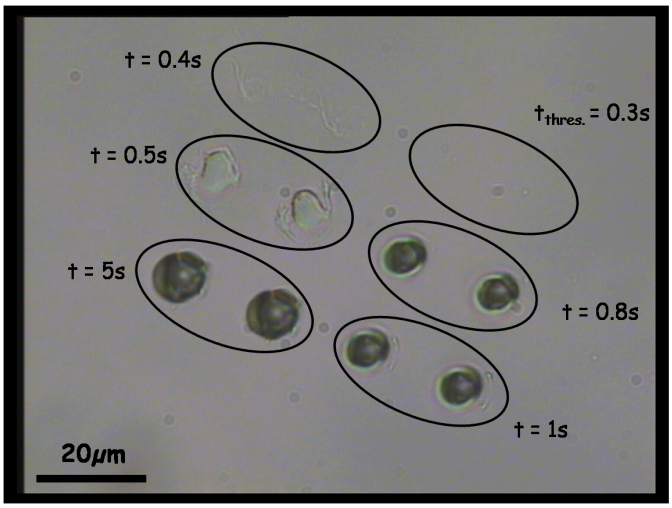

Figure 2.34: Optical image showing polymer dots of hybrid sol-gel solution: Determination of the threshold time of the photosensitive formulation at P = 3.54 μW.

interesting point in the sol-gel solution, in addition to the strong adhesion between the irradiated material and the substrate, is the ability to produce smaller polymer tips which encourage us to expect a nanoscale resolution for such materials.

To determine the threshold dose of the solution, we fixed the power at 3.54 μW and varied the time between 5 s and 0.3 s. As we can see on Figure 2.34, the threshold time is 0.4 s.

Figure 2.35 shows different polymer tips made with the same incident power, 3.54 μW, and the same exposure time, 0.7 s. The tips were used to write the name of our laboratory, LNIO, and that of our collaborators at Mulhouse, the DPG.

2.8 Conclusions

In this chapter, a quantitative study of noble metal nanoparticles was depicted. Along this study, we detailed the different techniques used to elaborate metal nanoparticles and the numerous ways adopted to characterize them. In a second time, the composition and the chemical mechanism of the different photopolymerizable solutions, used during this PhD work, were discussed. The characterization

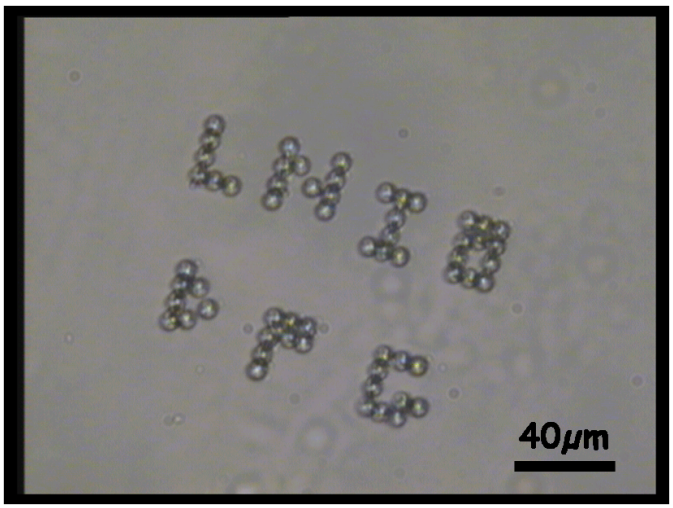

Figure 2.35: Optical image showing the fabrication of polymer dots using the same incident power and the same exposure time, 3.54 μW and 0.7 s respectively. The tips were used to write the name of our laboratory and that of our collaborators at Mulhouse, LNIO and DPG. (Reprinted with permission from Deeb, C. *et al.*, Proc. of SPIE, 7395, 739505-1 (2009). Copyright 2009 SPIE).

of the different molecular systems was also shown and the obtained results were interpreted.

The interaction metal/polymer was not discussed in the present chapter. This interaction will be detailed in Chapter 3 where we will show our ability to structure the photopolymer at the nanometric scale. In the first part of the following Chapter, we will show all the preliminary essays that have been achieved in order to determine, among all the types of metal structures and that of photopolymerizable systems described here, what is the best that suits our experiment.

In a second time, our approach used to directly image the dipolar profile of the near-field distribution, with a resolution better than 10 nm, will be itemized. With this approach, near-field profiles generated by LSP are recorded which enable us to quantify the near-field depth and its enhancement factor. It will be shown also our proficiency to get a near-field spectrum of a single metal nanoparticle. These results demonstrate a quantitative characterization, down to the nanometer level, of the confined evanescent optical fields that are prerequisite for developing photonic applications.

Chapter Three

Quantitatively Profiling Nanoparticles Plasmons with sub-10-nm resolution by molecular molding

3.1 Introduction

Optical properties of LSP supported by metal nanostructures have been introduced and discussed in Chapter One. As we argued in the first Chapter, the optical properties of metal nanoparticles have given rise to many efforts and studies over the past decade. [2, 6, 82, 83, 84] Indeed, this important branch of nanophotonics envisions many challenges and applications including solar energy harvesting, [85, 86, 87] optical manipulation, [8] efficient light generation, [9, 88, 89] local heating, [90] photothermal tumor ablation, [34, 91, 92] nanopatterning for data storage, [11, 54] nanoscale biosensing. [10, 31] A detailed understanding of the near-field response of engineered plasmonic nanostructures is therefore essential for controlling and optimizing a desired outcome along the line of the applications listed above. Determining a simple method for an accurate nanometer scale imaging of confined optical fields with quantitative measurements still constitutes an opened challenge.

As mentioned in Section 1.6, several efforts, namely proximal probe methodologies [51, 53, 59, 93] and electron microscopy, [57, 94, 95] have been made to better understand the near-field response of metal nanoparticles and their field distribution. All these methods constitute indirect and qualitative approaches of characterization: Near-field optical imaging techniques offer high resolution. How-

ever, they are complicated by sample-probe interactions. The presence of the probe perturbs the physics of the sample to be characterized and the effective object becomes a complex probe-sample nanosystem whose physics strongly depends on the geometry, material, etc. of the probe. On the other hand, photoemission electron [56] and electron energy-loss spectroscopy [58] microscopies are powerful technique, yet qualitative ones.

In the present chapter, we present many results of the approach introduced in Section 1.5, discuss the metal/polymer interaction, and show our ability to transact nanophotochemistry and to *map the near-field* of metal nanostructures by means of molecular probes. The first section of this Chapter will be dedicated to present our preliminary results performed on lithographic nanoparticles in presence of photopolymerizable solutions.
In the second part, we report a novel approach for imaging and *quantifying* both the depth and the strength of the optical near-field, of a single colloidal metal nanoparticle, associated with LSP. As introduced in Section 1.5, our approach relies on a nanoscale molecular molding of the confined electromagnetic field by a photo-activated polymer. We were able to directly image the dipolar profile of the near-field distribution with a resolution better than 10 nm and to quantify the near-field depth and its enhancement factor. [19] A near-field spectral signature of LSP of a single metal nanoparticle was achieved too and will be shown. These results demonstrate a quantitative characterization, down to the nanometer level, of the confined evanescent optical fields that are prerequisite for developing photonic applications.

3.2 Preliminary nano photopolymerization by means of lithographic nanoparticles

Nanoparticles fabricated using electron beam lithography have been firstly used to test our approach already detailed in Chapter 1. Two species of photosensitive formulations were utilized with this type of metal structures: Hybrid sol-gel and organic photopolymerizable solution using Eosin Y as dye. These two chemical systems were faithfully detailed in Chapter 2.

3.2.1 Using hybrid sol-gel as photopolymerizable system

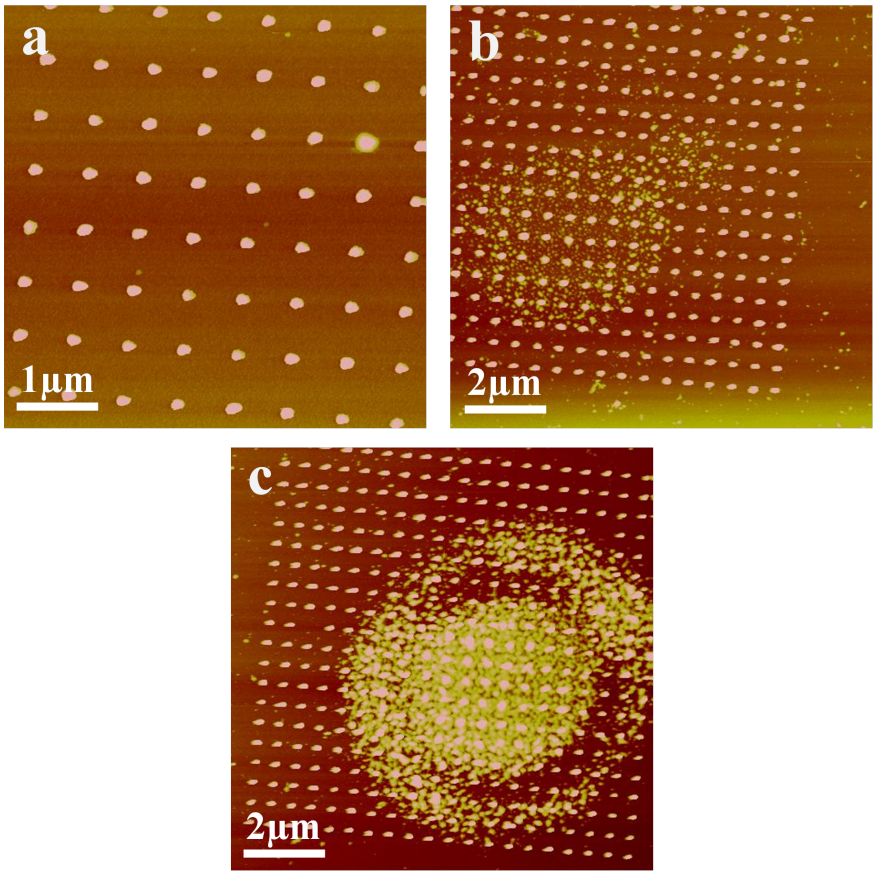

Figure 3.1: Photopolymerization using hybrid sol-gel in presence of lithographic nanoparticles. a) AFM image showing 70-nm diameter silver nanoparticles before the exposure. b, c) AFM images showing the lithographic nanoparticles after being irradiated during 0.2 s and 0.3 s, respectively.

Lithographic nanoparticles are consisting of cylindrical structures of 50-nm thickness, 300-nm edge-to-edge particles and with diameter varying from 60 to 110 nm. The metal structures are characterized before the exposure by means of AFM and extinction spectroscopy. The 70 and 80-nm diameter particles revealed to be the most suited one for our experiment since their extinction spectra overlap with absorption spectrum of the dye (see Figures 2.9 and 3.11 for silver nanoparticles spectra and for absorption spectrum dye, respectively). In parallel, the hybrid sol-gel is characterized with a 6-μm diameter laser spot and shows threshold parameters of 3.54 μW at 0.3 s. The full threshold study of this solution was shown in Chapter 2 (Figure 2.34).

Two exposures are performed on the metal structures using a wavelength of 514 nm and an incident power of 3.54 μW (i.e. $3.54\mu W/9\pi\mu m^2 = 0.125\times10^{-4}W/cm^2$): Both exposure doses are below the threshold one, one during 0.2 s and the second one during 0.3 s. Figure 3.1 shows the result of the two exposures. Figure 3.1 (a) shows a topographic AFM image of the 70-nm diameter metal nanoparticles before being irradiated with the laser beam. Figures 3.1 (b) and 3.1 (c) represent the AFM images of the silver lithographic particles after being shined during 0.2 s and 0.3 s, respectively.
These two images clearly reveal that the threshold dose was overcome at some locations (where no field enhancement is expected) and hence polymer dots are formed. This fact illustrates that the hybrid sol-gel is not homogeneous at the nanoscale level and it is, most probably, due to the presence of a higher number of dye molecules in the regions where the threshold was overcome. In other words, the obtained AFM images illustrate the spatial inhomogeneity of the threshold value. Therefore additional precautions must be taken into consideration to eliminate this inhomogeneity, namely using a filter paper while preparing the chemical solution. It must be pointed out that the apparent "speckles" in Figure 3.1 (b) and 3.1 (c) show a "beautiful" map of the zones with higher dye concentration and hence lower threshold. Despite the usefulness of this observation, this effect led us to temporarily forsake the use of these materials in order to focus on our objectives.

3.2.2 Using organic photopolymerizable solution with Eosin Y as dye

Silver lithographic nanoparticles were also used as light nanosources to induce nanoscale photopolymerization of an organic photosensitive solution utilizing the Eosin Y as dye (see Section 2.6 for additional informations about the chemical solution). This material is known to be homogenous at the nanoscale. Along this experiment, we use 70-nm diameter silver nanocylinders whose extinction spectra show a maximum peak at 485 nm in air. The chemical system is characterized using a 6-μm diameter laser spot (presenting a Gaussian profile) and shows a non-linear response identified by the following threshold parameters, 300 nW during t = 0.5 s.

Figure 3.2 shows the result of the exposure of silver nanoparticles with incident field linearly polarized along the vertical direction of the figure and an incident dose barely below the threshold one. Figure 3.2 (a) presents an AFM topographic image of the metal structures together with a polymer tip. The micrometer size

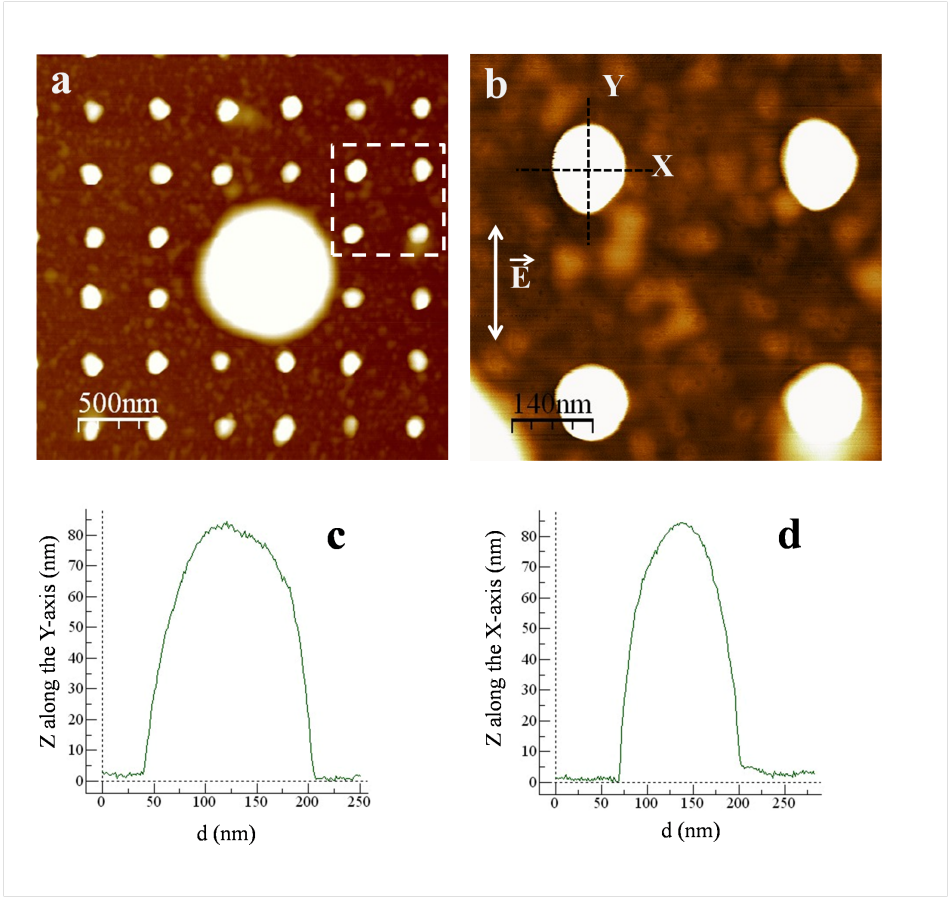

Figure 3.2: Photopolymerization of organic solution (with Eosin Y as dye) in presence of lithographic nanoparticles. a) AFM image showing 70-nm diameter silver nanoparticles together with a polymer tip. b) AFM image showing silver nanoparticles, around the polymer tip, irradiated with a dose smaller than the threshold one. The white vertical arrow indicates the direction of the incident field. c, d) Profiles of a single lithographic nanoparticles along the Y and the X-direction, respectively.

polymer disk is present where the incident dose exceeds the threshold one, at the peak of the beam Gaussian, and shows a diameter of 500 nm. Around the polymer disk where the dose is certainly below the threshold one as it can be shown in Figure 3.3, the metal nanoparticles are also irradiated with sufficient dose (6-μm laser beam) and exhibits elongation parallel to the direction of the incident field polarization, shown with the white vertical arrow, as it can be seen in the AFM image in Figure 3.2 (b). The elongation of the nanocylinders is due to a nanoscale photopolymerization induced by the local near-field based on LSP of the metal

structures. Indeed, using this procedure, we finish up with two lobes of polymer where a field enhancement is expected, parallel to the impinging field, which cause a nanoparticle elongation as it is illustrated in Figure 3.2 (c) and 3.2 (d). This point will be discussed in detail in the following section.

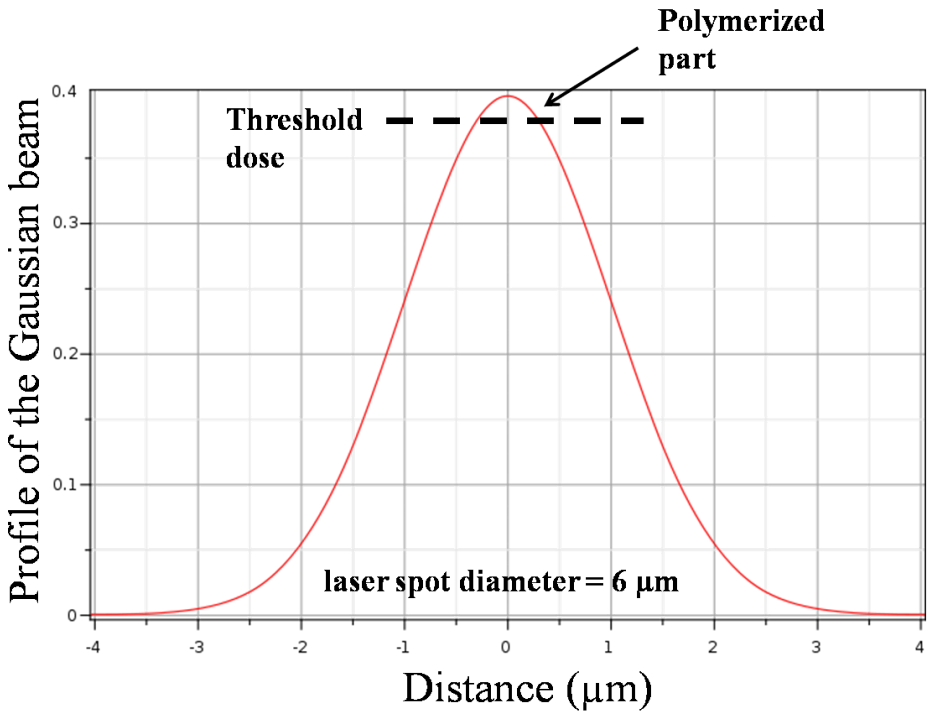

Figure 3.3: Illustration of the effect, seen in Figure 3.2, using a Gaussian profile beam. At the peak of the beam, where the dose exceeds the threshold one (indicated by the horizontal dashed line), a polymerized part is observed. The full width of the Gaussian beam is 6 μm as indicated on the x-axis.

Based on the results we presented in this section, we decided to use during the rest of this PhD dissertation the organic photopolymerizable solution with Eosin Y as dye, since the hybrid sol-gel shows an inhomogeneity at the nanoscale which might influence our approach.
Additionally, lithographic particles are localized on a nanometric region. In order to save time and samples and hence increase the probability of using the same sample for more than one exposure, we started working with colloidal silver nanoparticles which may be dispersed on the total surface of the glass sheet. The

results shown in the rest of this Chapter are hence based on the interaction "silver colloids/organic photosensitive systems".

3.3 Detailing our approach using colloids as nano-sources of light: First Results

Chemically-synthesized Ag NPs are here anchored on a silane-functionalized [49, 96] glass cover-slip by a dip-coating procedure 3.4 (a). The amino-silane functionalization guarantees a firm adhesion of the nanoparticles on the glass cover-slip despite the various stages of rinsing (see Chapter 2 section 2 for additional information on functionalizing the glass sheets).

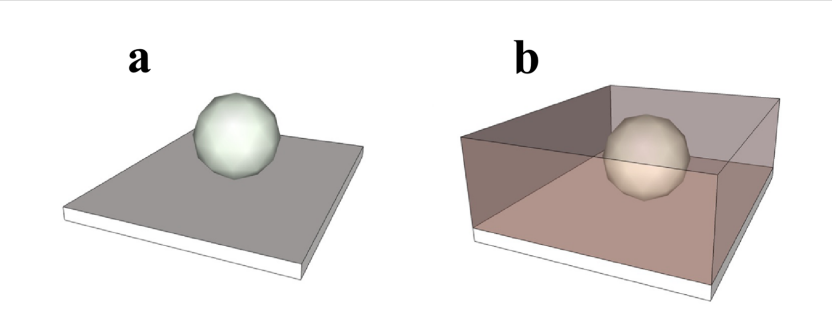

Figure 3.4: Deposition of the Ag NPs and the photopolymerizable solution on the glass substrate. a) Ag NP deposited on a functionalized glass substrate. b) Deposition of the photopolymerizable formulation. (Reprinted with permission from Deeb, C. *et al.*, ACS Nano, 4, 4579-4586 (2010). Copyright 2010 American Chemical Society).

To selectively address single nanoparticles of well-defined geometry, the decorated glass substrate is placed on an inverted optical microscope that couples to an AFM. The procedure followed to functionalize the glass substrates and the experimental set-up used to selectively address single metal nanoparticles were detailed in Sections 2.2 and 2.7, respectively. Next, the nanoparticles are homogeneously covered by a synthesized free radical photopolymerizable formulation (Figure 3.4 (b)) possessing high-resolution visible-light sensitivity and characterized by a threshold dose that must be overcome to induce the polymerization process (see Chapter 2 for additional information on the photosensitive systems). A controlled volume of the chemical solution is deposited onto the metal structures using a pipet. A drop

of 4-cm diameter, corresponding to a volume of 40 μl, was consistently obtained.

Let us remind some important steps of the procedure. The polymerization is activated by laser irradiation with wavelengths overlapping both the photopolymerizable formulation absorption spectrum and the Ag NPs plasmon resonance. The optical exposure is performed under normal incidence with a 1-cm wide linearly polarized laser beam from an Ar:Kr laser source. Namely, we used 514 nm as incident wavelength along this experiment. The exposure dose D_0 is chosen to be smaller than the threshold dose, D_{th}, below which no polymerization can occur (Figure 3.5 (a)). This threshold value is systematically quantified by far-field prestudies, as presented in Sections 2.6 and 2.7. Therefore, photopolymerization is not expected to occur in the absence of Ag NPs: because of the field enhancement at the plasmon resonance (see Figure 3.5 (a)), the effective dose near the metallic nanoparticles can be greater than the threshold D_{th} to initiate the chain reaction leading to polymerization as seen in Figure 3.5 (b).

After irradiation, any monomer that is not reticulated is removed by a rinsing procedure with ethanol and isopropanol (Figure 3.5 (c)) and characterized by AFM using intermittent-contact mode. It should be stressed that AFM characterization before and after the exposure is performed for the same pre-selected individual Ag NP. The coupled AFM-inverted optical microscope allows us to address single labeled particles and to retrieve them after the rinsing procedure. The size of the polymer wings attached to Ag NPs corresponds to the strength and the depth of the optical near-field, which allows us to quantitatively map the plasmon response unlike few previous reports that have demonstrated plasmon-enhanced photo-polymerization.
In particular, C. Ecoffet and coworkers produced for the first time polymer nanoparts by using a simple Fresnel evanescent waves generated by total internal reflection. [73] In this experiment, nanometer-resolution was achieved but only along the direction perpendicular to the substrate. G. Wurtz et al. showed that the lightning rod effect at the extremity of a metal tip under laser illumination could lead to local polymerization. [97] Srituravanich and coworkers demonstrated 90-nm resolution in plasmon-based optical lithography on negative-tone photopolymer with the use of an array of nanoapertures on a metal film. [98] Sundaramurthy et al. qualitatively evidenced the presence of locally enhanced field in the gap of a metal bowtie antenna. [99] Ibn el Ahrach et al. introduced new hybrid polymer/metal nanostructure produced by plasmon-based photo-polymerization. [20] More recently, K. Ueno and co-workers demonstrated sub-100 nm resolution photo-polymerization at the gap separating two gold nanoblocks. [100]

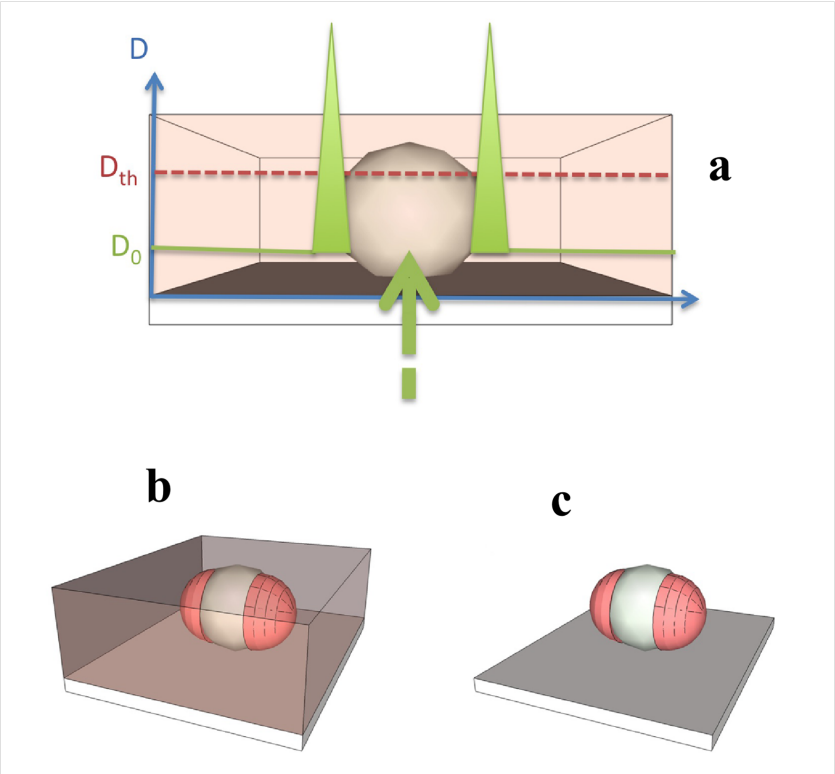

Figure 3.5: Fabrication of Hybrid nanoparticle. a,b) Plasmon based near-field photopolymerization of photopolymerizable formulation leading to two wings corresponding to the dipolar LSP resonance. c) The resulting hybrid nanoparticle is revealed by rinsing procedure. (Reprinted with permission from Deeb, C. *et al.*, ACS Nano, 4, 4579-4586 (2010). Copyright 2010 American Chemical Society).

In all of these works, the main motivation was either to produce nanostructures through plasmon-based lithography, or to perform a qualitative observation of plasmonic fields (proof of presence of hot spots, evidence for excitation of electromagnetic singularities, etc.). Quantification of the plasmon near-field was neither achievable nor performed. Here, a full parameter study is carried out and quantitative parameters values related to localized surface plasmons are measured. In particular, the knowledge of the plasmon field enhancement factor still constitutes a challenge. At best, a wide range of enhancement factor values have been reported in the literature based on numerical calculation and indirect measurements. We will show that our approach provides realistic values of these enhancement factors by relying on a well-referenced and well-characterized system, i.e. the free-radical polymerizable formulation.

Figure 3.6 demonstrates the ability to directly visualize the optical near-field with the approach described above. Figure 3.6 (a) shows topographic image of Ag NPs deposited on the functionalized glass before exposure. A single isolated particle was chosen (circle) to demonstrate our ability to map the field down to sub-10-nm resolution. Due to tip convolution, its apparent diameter is 110 nm while its actual diameter is 60 nm as deduced from the height of a cross section acquired through the center of the Ag NP. Since the colloidal particles used are spherical, the height acquired from a section sketched along the metal structures represents their diameter. Throughout our current analysis, only similar sized and nearly spherical particles were considered. A close-up image of the selected particle is displayed in Figure 3.6 (b). After the deposition of the photopolymerizable formulation, the Ag NPs were illuminated with a y-oriented linearly polarized light at $\lambda = 514$ nm. The exposure dose D_0 was set to 63% of D_{th}. The threshold conditions of the chemical solution used here have been determined to be incident power P = 2 mW/cm^2 with an irradiation time t = 3.5 s, implying a threshold dose D_{th} of 7 mJ/cm^2. We kept the incident laser power constant at 2 mW/cm^2, while varying the irradiation time across our experiments. As a typical example, in order to set D_0 to 63% of D_{th}, we set P = 2 mW/cm^2 and t = 2.2 s.

Figure 3.6 (c) shows a topographic image of the same selected particle after rinsing. It exhibits an elongation along the y-direction that results from the photopolymerization initiated by the enhanced local field. It should be highlighted that Figure 3.6 (b) and 3.6 (c) were obtained for the same metal nanoparticle with the same tip under the same scanning conditions.

In order to highlight the localized photopolymerization, we subtract Figure 3.6 (b) from Figure 3.6 (c), resulting in Figure 3.6 (d). Such differential image accurately depicts the spatial distribution of the polymerization resulting from the reticulation process, while circumventing the apparent increase of the polymer depth due to convolution with the AFM tip. Figure 3.6 (d) clearly reveals two polymer wings oriented along the incident polarization direction.
To elucidate wings origin, we numerically map in Figure 3.6 (e) the intensity distribution of an isolated Ag NP with finite-difference time-domain (FDTD) simulations. The field distribution is calculated for a spherical 60-nm Ag NP embedded in a medium of refractive index 1.485, matching that of the photopolymerizable formulation. The calculation shows a two-lobe pattern characteristic of a dipolar near-field distribution. The similarity between Figure 3.6 (d) and Figure 3.6 (e) implies that the enhanced localized near-field is responsible for the nanoscale photopolymerization.

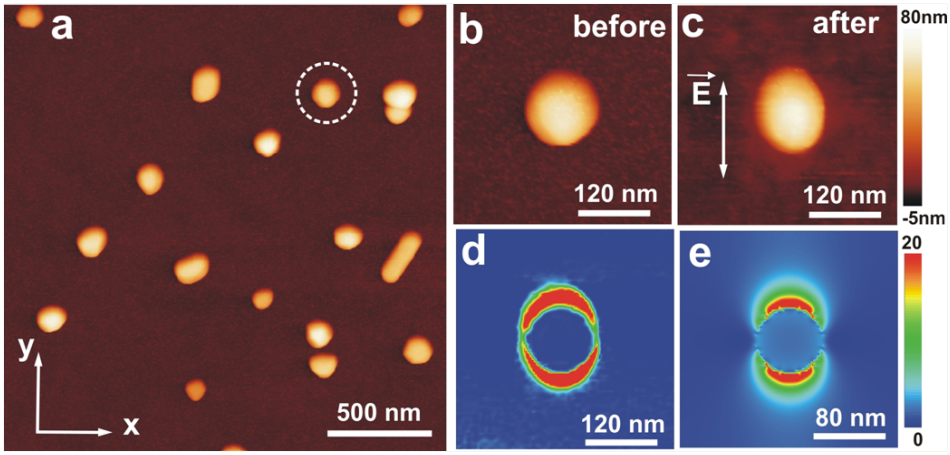

Figure 3.6: Near-field photopolymerization based on the resonant excitation of the dipolar plasmon mode of Ag NPs. a) Topographic AFM image of Ag NPs before the procedure. b) Close-up image of a. c) Close-up image of topographic image of Ag NPs after the procedure. d) Differential image of Figure c and Figure b. d) Near-field intensity as calculated by FDTD. (Reprinted with permission from Deeb, C. *et al.*, ACS Nano, 4, 4579-4586 (2010). Copyright 2010 American Chemical Society).

We demonstrate the mapping of the evanescent optical near-field supported by resonant LSP of individual silver nanoparticles, with sub-10-nm resolution. As proved, our approach relies on exploiting the enhancement of the electric field around a resonantly excited silver nanoparticle to trigger local photopolymerization, resulting in a polymer mold, which directly profiles the dipolar near-field distribution around the particle. The resolution with which we are able to profile the near-field is unprecedented (sub-10-nm). To the best of our knowledge, this is the first time, a sub-10 nm resolution photo-polymerization is being demonstrated in the visible, allowing, in turn, a sub-10 nm optical resolution characterization of plasmonic structures. Our unprecendented resolution is due to the use of the free radical formulation designed in house and optimized for molecular-level resolution, rather than commercial SU-8 resin that has been optimized only for UV-blue far-field lithography. [100]

In the coming section, we will detail all the artifacts that may cause an artificial nanoparticle elongation that resembles the one shown in Figure 3.6 (c), and will exclude them. Sample drift and tip wear are discussed and it will be shown that AFM measurements use to account for each and every one of those controls in our technique. In fact, our technique relies on these controls.

3.4 Possible Artifacts

Before going through the details of our parametric studies, we show in Figures 3.7 and 3.8 additional evidence that the dipolar profile distribution based on LSP of Ag NPs is responsible for the observed nanoscale photopolymerization. Actually, this section is dedicated to the discussion of possible artifacts that can lead to an artificial elongation of the metal nanoparticle. In order to guarantee that such artifacts are not affecting our measurements and that we use to account for each and every one of those controls in our experimental work, two types of possible artifacts are detailed: tip wear and sample drift.

3.4.1 Tip wear

The usage of the same AFM tip before and after the exposure may cause an enlargement in its size, leading to an artificial broadening in the AFM image. In order to make sure that such artifact does not affect our results, we calculated the differential profiles along the direction perpendicular (x-axis) to the incident field where no field enhancement is expected. Figure 3.7 shows this differential profile obtained by subtracting the topographical profile before polymerization from that after polymerization using a dose of $0.75D_{th}$.

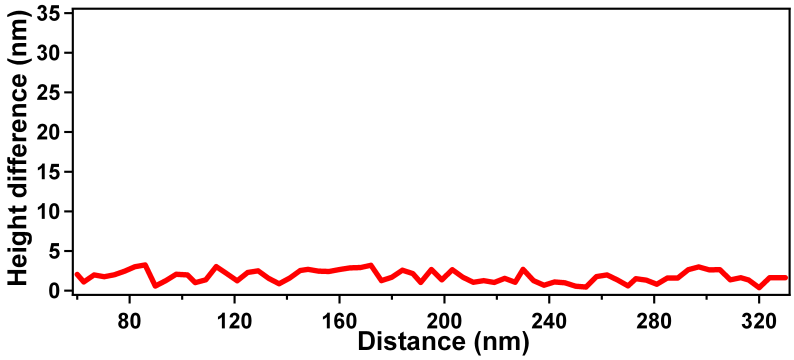

Figure 3.7: Height difference of an Ag NP taken along the x-axis before and after the polymerization for an incident dose of $0.75D_{th}$. (Reprinted with permission from Deeb, C. *et al.*, ACS Nano, 4, 4579-4586 (2010). Copyright 2010 American Chemical Society).

It clearly demonstrates that, since the Ag NP has the same apparent size and geometry along the x-direction before and after the procedure, the AFM tip had

almost the same characteristics while scanning the two images. This ensures that we are able to retrieve our region of interest rapidly without compromising the tip quality.

3.4.2 Sample Drift

Sample drift in the y-direction can lead to artificial elongation especially if we consider that the y-axis is the slow scan axis. In order to make sure that such artifact does not influence our results, we use to make some additional AFM images after the exposure by rotating the sample by 45°. The apparent elongated axis rotates by 45° too, demonstrating that the observed elongation is not a scan effect. In particular, this ensures that the two wings of polymer are purely due to the dipolar field and not due to sample drift during AFM imaging.

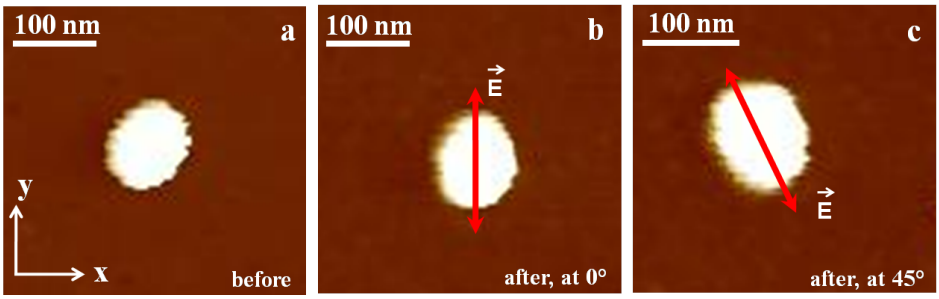

Figure 3.8: a) AFM image of selected nanoparticle before irradiation. b) AFM image after irradiation where the fast scan direction is along the x-axis and perpendicular to the field polarization. c) AFM image for the same particle with fast scan direction along the x-axis direction and sample rotated by 45°. (Reprinted with permission from Deeb, C. *et al.*, ACS Nano, 4, 4579-4586 (2010). Copyright 2010 American Chemical Society).

Figure 3.8 (a) shows a topographic AFM image before the laser exposure. An Ag NP with high in-plane symmetry is chosen to illustrate our ability to map the near-field distribution by means of molecular probes. Figure 3.8 (b) illustrates the AFM image of the same particle after being exposed to the laser beam with polarization along the vertical direction. Figure 3.8 (c) shows an AFM image of the same nanoparticle after rotating the sample by 45°. It should be noted that the fast scan direction is always kept along the x-axis for three panels of Figure 3.8. The selected Ag NP exhibits an elongation (Figure 3.8 (b)) in the same direction as the laser polarization shown by the red arrow. When the sample is rotated

by 45° (Figure 3.8 (c)), the elongation of the particle persists in the direction of the incident field, demonstrating that the imaged elongation of the Ag NP is not an artifact due to sample drift but it is purely due to nanoscale polymerization triggered by the LSP of the Ag NP.
It should be noted that we prefer to not use the y-axis as a fast AFM scan because the cantilever is parallel to this y-axis. Fast scans parallel to the cantilever can induce complex mechanical effects and additional artifacts.

We have attempted to be much more quantitative compared to previous works in the area of near-field imaging. By precise characterization of the polymer molds using AFM, which will be shown in the upcoming section of this chapter, we extract precise values for the enhancement factor and the depth of the near-field, which agree with electrodynamic simulations. We are also able to measure the spectral signature of the localized surface plasmon resonance directly in the near-field. These results will be annotated in the following section.

3.5 Quantitative characterization of Localized Surface Plasmons

3.5.1 Dependence of the polymer wings size on the exposure dose: Determination of the enhancement factor and the near-field penetration depth of LSP of spherical Ag NPs

We studied the dependence of the size of polymer wings on the exposure dose. [19] The profiles presented in Figure 3.9 emphasize the fact that the similarity between the differential image of Figure 3.6 (d) and the simulated distribution of Figure 3.6 (e) is due to the plasmon's near-field intensity which is effectively responsible for the process of photopolymerization.

Figure 3.9 (a) shows the height difference of a typical Ag NP obtained by subtracting topographic profile along the y-axis before and after the procedure excluding laser exposure. This figure shows a flat differential profile that reflects that no polymer wings can be formed without laser exposure, and hence without nanoparticle field enhancement. Figure 3.9 (b) shows the differential profile along the y-axis obtained by subtracting the topographical profile before polymerization

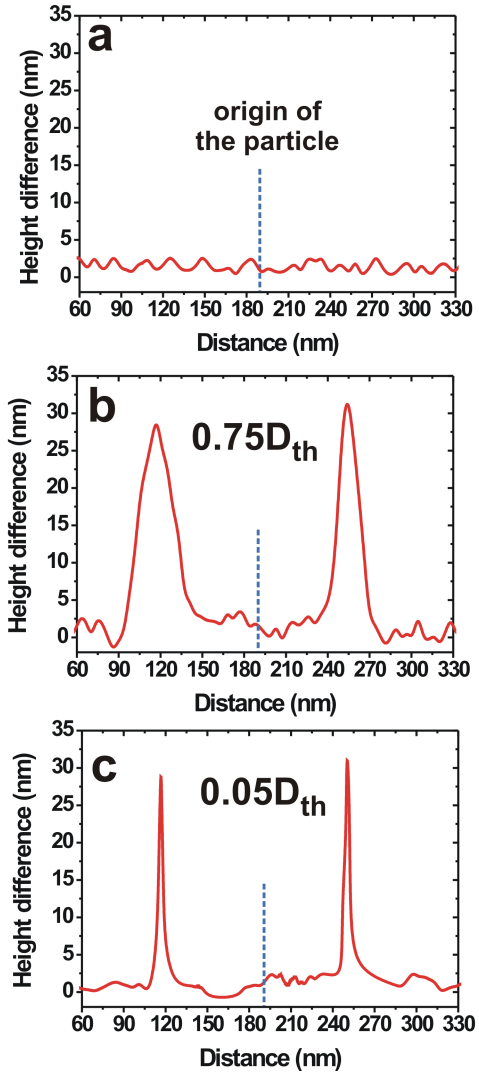

Figure 3.9: Molding the plasmon's near-field intensity by the process of photopolymerization. a) Reference profile: height difference of an Ag NP taken along the y-axis before and after the procedure excluding laser exposure. Differential profile along the y-axis for b) $0.75D_{th}$ and c) $0.05D_{th}$. (Reprinted with permission from Deeb, C. *et al.*, ACS Nano, 4, 4579-4586 (2010). Copyright 2010 American Chemical Society).

from that after polymerization using a dose of $0.75D_{th}$. Two peaks characterized by a height difference of 25 nm are standing out. These features clearly reveal a 20-nm full-width at half-maximum (FWHM) lateral extension of the particle along the y-direction, resulting from a near-field photopolymerization. This differential

profile should be compared to Figure 3.7 and Figure 3.9 (a).

The lateral extension of the polymer wings strongly depends on the enhancement factor and the exposure dose with respect to D_{th}. As an example of this dependence, the differential profile of Figure 3.9 (c) illustrates the situation for a much lower incident dose of $0.05D_{th}$. It features a much narrower polymer wing with 10-nm FWHM, i.e. $\sim \lambda/50$. We explain the dependence of the FWHM on the exposure dose as follows. For an exposure dose of $0.75D_{th}$, photopolymerization can occur at any location where the field enhancement factor exceeds $D_{th}/D_0 = 1.33$; while for an exposure dose of $0.05D_{th}$, only locations with an enhancement factor higher than will $D_{th}/D_0 = 20$ support photopolymerization.

It should be noted that although image differentiation allows one to evaluate the actual width of the polymer wings, the apparent distance between the two wings is, however, increased by AFM tip convolution.

We performed systematic quantitative studies of the size of the polymer wings as a function of the dose. Different doses smaller than D_{th} have been used ensuring that no far-field polymerization may occur. Figure 3.10 (a) shows the averaged full width w, shown in red squares, of the polymer that was reticulated and measured by AFM as a function of d (the normalized incident dose D_0/D_{th}). Each point corresponds to the average value of the full width of the two standing peaks, as shown in Figure 3.9 (b) and 3.9 (c), at different values of the normalized incident dose d. It must be also noted that each point is the average result corresponding to three different experiments made on three identical particles exposed with same dose. The graph demonstrates a monotonic logarithmic increase of w with d. We will see that this ln function is actually the signature of the evanescent nature of the involved plasmonic field.

This result can be understood by considering the near-exponential decay of the evanescent field scattered by the nanoparticle. The local dose D provided by the metallic nanoparticle in the y-direction can be expressed as in Eq. 3.1:

$$D = F_{max} D_0 exp(-\alpha y) \tag{3.1}$$

Where F_{max} is the maximum intensity enhancement factor related to the LSP resonance, α is the rate of field intensity decay, and y is the distance from the metallic nanoparticle. α^{-1} can be viewed as the spatial extension of the near-field intensity. We consider here the y-direction because along this direction the incident field is perpendicular to the metal/dielectric interface allowing surface charges to be excited. [101] Second, α is an average of the continuous spectrum

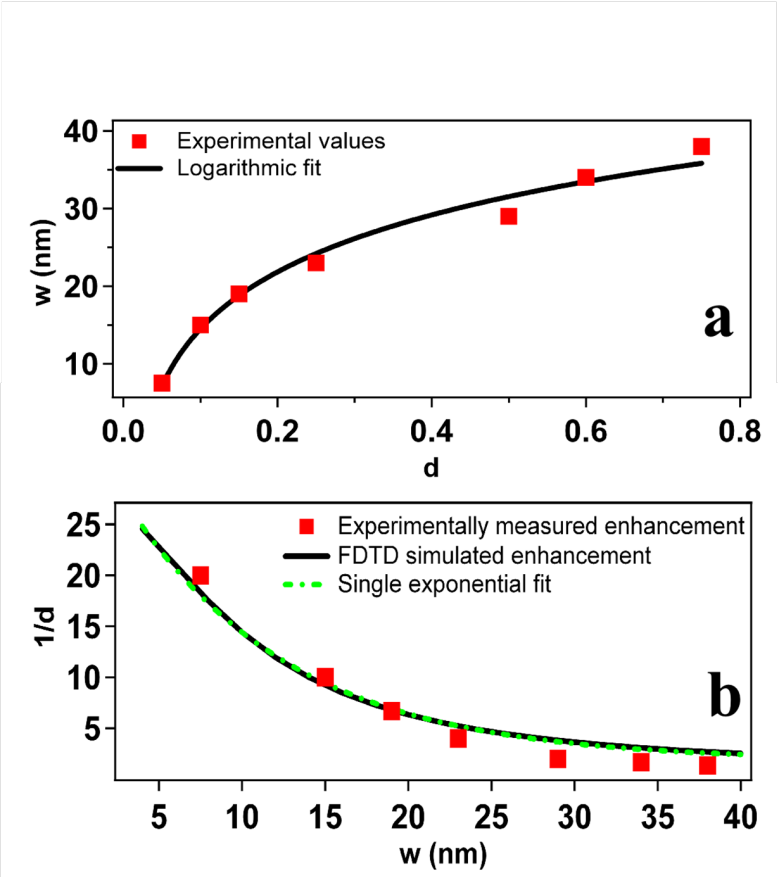

Figure 3.10: Quantification of the physical parameters related to localized surface plasmons. a) Effect of the incident dose on the photopolymerization width of polymer: experimental value (red squares) and fitting function $y = 11\ln(39 \times d)$. b) Experimental values (red points) of the local field-enhancement factor of Ag NP drawn as a function of the polymer width measured by AFM. Black line corresponds to the FDTD simulated enhancement and dashed green line is a single exponential fit. (Reprinted with permission from Deeb, C. *et al.*, ACS Nano, 4, 4579-4586 (2010). Copyright 2010 American Chemical Society).

of decay lengths (each of them being associated to lateral wave vectors) of the angular spectrum generated by the Ag NP diffraction. [102]
As discussed in the earlier section, photopolymerization occurs when D $\geq D_{th}$; By applying this condition to Eq. 3.1, we get:

$$\exp(-\alpha y) \geq \frac{D_{th}}{F_{max} D_0} \tag{3.2}$$

By reducing Eq. 3.2, we get the locations where the photopolymerization can

occur:

$$y < y_{max} = -\alpha^{-1} \ln(\frac{D_{th}}{F_{max} \times D_0}) \tag{3.3}$$

Replacing D_0/D_{th} by the normalized dose d, Eq. 3.3 can be written as:

$$y_{max} = \alpha^{-1} \ln(F_{max} \times d) \tag{3.4}$$

y_{max} is nothing but the measured w which can be expressed as $w = \alpha^{-1} \ln(F_{max} \times d)$. So our experimental values can be fitted with the following logarithmic function:

$$y = \alpha^{-1} \ln(F_{max} \times x) \tag{3.5}$$

By fitting our experimental data with the logarithmic function given by Eq. 3.5 and represented by the solid line in Figure 3.10 (a), we obtain 39 and 11 nm as values for F_{max} and α^{-1}, respectively.

The results of Figure 3.10 (a) can be treated differently to acquire the distance dependence of the local field-enhancement factor. Figure 3.10 (b) plots *1/d* as a function of *w*. The data, represented by red marks, resembles an exponential decay function that reflects the exponential decay of the plasmon near-field distribution. The experimental data is also in a good agreement with the FDTD simulated enhancement represented with the black curve. The simulated FDTD data were fitted with an exponential function, shown by the dashed green curve, and fitted values of F_{max} and α^{-1} are 34 and 10 nm respectively. The excellent agreement between the experimental data and the FDTD simulations strongly supports that our approach is able to profile the optical near-field of a single metallic nanoparticle with nanometer precision.

Moreover, our experimental results indicate that the near-field depth α^{-1} of colloidal spherical Ag NP is ~ 0.2 times the nanoparticle diameter (60 nm), which is consistent with the distance-decay observed for near-field coupling in particle-pairs. [103] In [103], Jain *et al.* found that interparticle plasmon coupling strength for polarization along interparticle axis decays nearly exponentially with a decay length, which is roughly about 0.2 in units of the particle size for different nanoparticle size, shape, metal type, or medium dielectric constant. Our direct mapping of the plasmonic field, thus, confirms the near-field distance-dependence proposed on the basis of indirect far-field spectra . To the best of our knowledge, this evanescent field depth value constitutes the first measurement achieved directly in near-field.

It should be stressed that the present approach of plasmon near-field characterization is direct. Near-field scanning probe optical microscopies (NSOM) have allowed extraction of immense optical information about metal nanostructures over the past two decades. [59, 93] However, NSOM is not a direct method and constitutes an inverse problem in the sense that, in NSOM, the near-field interaction between tip and sample leads to propagating waves that are integrated and detected in the far-field (Huygens Fresnel Principle). The precise control of the position of the tip along with the scan allows for sub-wavelength near-field imaging. The achieved resolution depends on many parameters including the nature of the interaction, the tip-to-sample distance, and the tip size. What is actually measured in NSOM is the far-field of a system resulting from the subtle "controlled" coupling between tip and sample. A primary issue with NSOM is that the nature of the signal depends very much on the tip quality as well as its surrounding environment. As a specific example, the signal from an apertureless NSOM can be proportional to either the intensity, or, to the complex field depending on the presence of surrounding scatterers acting as reference fields of an interferometric system. [104] An alternative way is to use single scatterers (e.g., molecules, quantum dots, etc.) to characterize the near-field via fluorescence emission. [105] However, in these methods, the fluorescence signal reports the competition between tip-induced near-field enhancement and quenching (energy transfer).

3.5.2 Dependence of the polymer wings size on the incident wavelength: Near-field spectral signature for single spherical Ag NPs

Due to the dispersive nature of the plasmon response, F_{max} is a function of λ and therefore the local photopolymerization should reflect the LSP spectral dependence. [19] Unlike the traditional approach of far-field spectroscopy, [13] our approach provides for the first time the opportunity to investigate this dispersive relationship directly in the near-field.

To illustrate this capability, we used the eight available wavelengths of the Ar:Kr source. The spectral response of the photochemical system, i.e. the function $D_{th}(\lambda)$, is characterized by far-field spectral investigation of D_{th}. Figure 3.11 (a) shows the measured D_{th} as a function of the incident wavelength. A clear minimum is observed at $\lambda = 530$ nm. This minimum corresponds to the maximum of the absorption spectrum (530 nm) of the Eosin Y dye used as a photo-sensitizer (Figure 3.11 (b)). The knowledge of the D_{th} for each λ allows us to set the normalized dose d at a constant value.

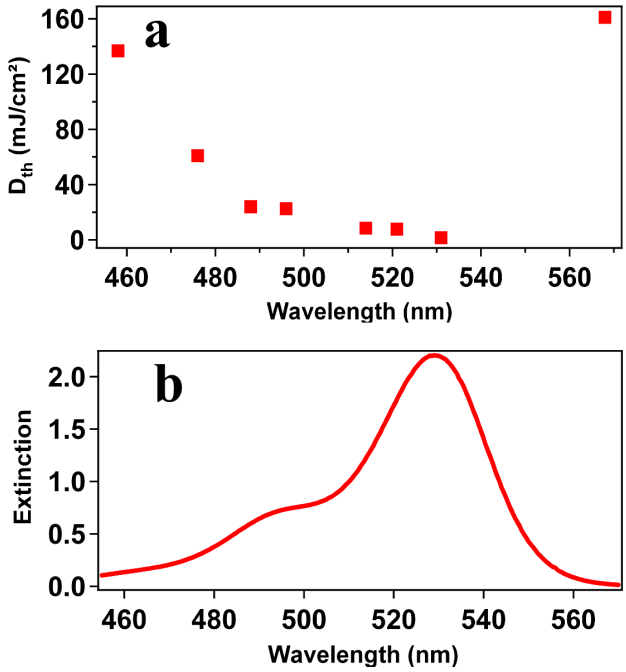

Figure 3.11: Spectral response of the photochemical system characterized in the far-field. a) Variation of D_{th} as a function of the incident wavelength. b) Absorption spectrum of the Eosin Y dye in the photochemical system. (Reprinted with permission from Deeb, C. *et al.*, ACS Nano, 4, 4579-4586 (2010). Copyright 2010 American Chemical Society).

Figure 3.12 shows w, related to F_{max}, as a function of wavelength for constant d = 0.75. Here we neglect the influence of the photochemical effects (in particular the diffusion of oxygen and dye) by considering them to be constant parameters. The spectrum in Figure 3.12 reflects the near-field spectral response of the Ag NP. A clear resonant behavior is observed and is attributable to the spectral signature of the underlying LSP mode, with a maximum at 494 nm as per a Gaussian fit (black curve). Our characterization approach is powerful because it provides in a simple manner the near-field spectrum of a single Ag NP that has unique information not accessible by far- field measurements.

Comparing this near-field spectrum to the far-field one, already shown in Figure 2.13, we remark that the ensemble far-field spectrum has a much broader width that result from inhomogeneous broadening due to NP size dispersion and a plasmon maximum at 452 nm. Using Eq. 3.6 to calculate the shift in wavelength, [20]

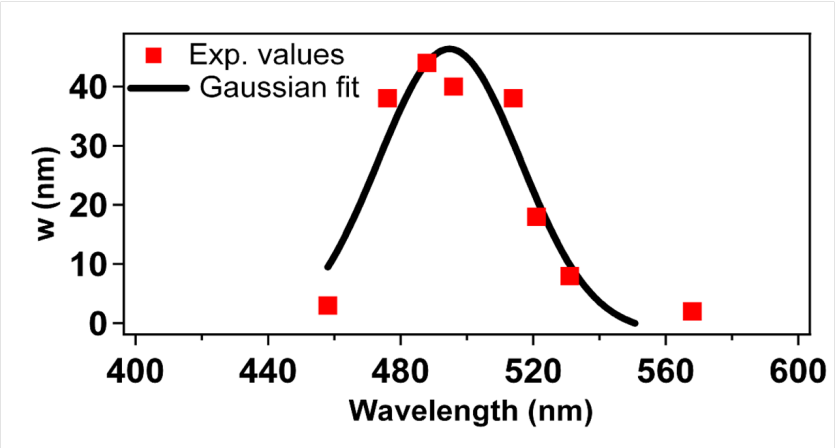

Figure 3.12: Near-field spectrum of a single Ag NP: Effect of the incident wavelength on the polymer width (red points) fitted by a Gaussian function (black line). (Reprinted with permission from Deeb, C. *et al.*, ACS Nano, 4, 4579-4586 (2010). Copyright 2010 American Chemical Society).

while changing the outer medium of Ag NPs from water to the photopolymerizable solution,

$$\Delta\lambda = -4n_m\Delta n_m\frac{d\lambda}{d\epsilon} \tag{3.6}$$

and by considering n_m as the refractive index of water, and Δn_m = 1.485 - 1.33 = 0.155, and based on published values of the silver dielectric function ϵ, [106] we found $\Delta\lambda$ to be 12 nm. Thus the extinction maximum peak of Ag NPs is expected at 464 nm. We believe that the difference between the corrected far-field spectrum and the near-field one is attributed to the size and shape distributions of the solution (Figure 3.6 (a)) and its effects on the far-field inhomogeneous line-width. Our characterization approach is powerful because it provides in a simple manner the near-field spectrum of a single Ag NP that has unique information not accessible by far-field measurements.
To our knowledge, this is the first time an optical spectrum from a nanostructure has been directly extracted in the near-field. In general, near-field optical spectroscopy is permitted by the use of a tip. However, as pointed out above, what is actually measured in near-field spectroscopy is the far-field signature of the spectrum resulting from the coupling between tip and sample. In the present approach, we used a constant incident normalized dose (D_0/D_{th}). The resulting data are dependent mostly on the spectral characteristics of the metal nanoparticle. At the most, the presence of the photopolymer leads to a simple homogenous spectral shift in accordance with what would be introduced by increasing the surrounding

refractive index. In the case of the use of a scanning tip, on the other hand, the spectral dispersion of the particle resonance is expected to depend in a complex manner on the position, nature, and geometry of the tip.

3.6 Conclusions

In conclusion, we presented in this Chapter an approach of "metal/polymer" nanoscale interaction and demonstrated our ability to launch a photochemical process at precise regions where a field enhancement is expected.

In the first section, we showed preliminary studies that validated our approach. Then, we elucidated our approach that permits us to quantitatively characterize the evanescent optical near-field of single Ag NPs. Our data point out our ability to directly map, with sub-10-nm resolution, the evanescent optical near-field supported by resonant LSP of individual Ag NPs using molecular probes. As discussed previously, our approach relies on exploiting the enhancement of the electric field around a resonantly excited Ag NP to trigger local photopolymerization, resulting in a polymer mold. The resolution with which we were able to profile the near-field is unprecedented (sub-10-nm).

Moreover and by precise characterization of the polymer molds using AFM, we were capable to extract precise values for the enhancement factor and the depth of the near-field, which agree with electrodynamic simulations. Our direct measurement of the distance decay of the near-field confirms for the first time the model proposed in earlier work on the basis of indirect far-field spectra. We are also able to measure the spectral signature of the LSP resonance directly in the near-field. This spectral direct signature allows for interrogating the near-field response of the Ag NPs, which addresses the fundamental difference between near-field and far-field spectra.

Whereas the interest of the approach is demonstrated here in the well known case of near-field plasmon dipolar resonance of a spherical Ag nanoparticle, it can be extended to more complex particle geometries that exhibit interesting resonances and various physical phenomena. It is worth noticing that this method can also be potentially used to probe a larger fraction of the full three-dimensional near-field intensity distribution, whereas previous methods are generally sensitive only to the near-field distribution at the tip apex.

Chapter Four

Off-Resonant Optical Excitation of Gold Nanorods: Nanoscale Imprint of Polarization Surface Charge Distribution

4.1 Introduction

The interaction metal/polymer, with metallic nanoparticles irradiated at their resonance, has been discussed in Chapter three. Throughout the studies achieved along the previous Chapter, we demonstrated our ability to map the near-field of colloidal silver nanoparticles by means of probes consisting of molecules. We were also capable to quantify the enhancement factor and the depth of the near-field associated with this type of metal nanostructures. Additionally, a near-field spectrum corresponding to the LSP of a single colloidal nanoparticle has been recorded. In few words, Chapter three has described the way we employed our photochemical approach to quantitatively image the resonant behavior of metallic nanoparticles.

Let us now imagine the case of a metal nanoparticle embedded in the same type of photopolymerizable solution used in Chapter three, yet irradiated with an incident wavelength far from that corresponding to LSPR. Under these conditions of illumination, the metal nanoparticle is not considered anymore as a resonant nanosource of light, but an off-resonance one. The surface charge density held at the interface metal/dielectric, which is the surrounding photosensitive medium in our case, will start oscillate with the incident field. At this stand, many questions

may arise in this case of experiments:

Will we be able to profile the field associated with the surface charges that are localized at the interface? Will the amplitude of this field be high enough to overcome the threshold dose and to initiate the polymerization process? If the field enhancement is enough to have an effective dose, near the nanoparticle interface, that exceeds the threshold one, do we image all the components of the field... Or only the components for which the unit vector is normal to the interface and aligned with the incident polarization, as was predicted by the quasistatic approximation?
All these questions and others will be addressed along this Chapter.

4.2 Boundaries conditions and non-resonant behavior

When a metal conductor is under no electric field, or more generally, in the situation described by the theory of electrostatics, the charge carriers are driven by a random motion; hence no electric current is observed and consequently the metal is said to be in electrostatic equilibrium.
Once placing the metal in a region of space where there is an electric field, the free charges, electrons negative charges, of the metal and under the influence of the field, start moving to reach its boundaries; this implies that on the other end there will be positive charges. The imbalance of charges will induce an electric field that opposes the prevailing electric field. The movement of charges cease when the two fields, the applied incident field and the one created in the conductor, oppose at any point inside the conductor. The electrostatic equilibrium is re-established. Assuming a conductor that obeys Ohm's law and for which the electrostatic equilibrium is settled, thus the current flowing inside is given by Eq. 4.1:

$$\overrightarrow{j} = \sigma \overrightarrow{E}_{inside} = \overrightarrow{0} \tag{4.1}$$

Where σ is the metal conductivity. Note that the attenuation of the power inside a non-perfect conductor can be expressed by means of the so-called "penetration" or "skin depth", defined as the inverse of α, as $\delta = 1/\alpha$. This means that the electric field $\overrightarrow{E}_{inside}$ inside a metal conductor, away from its edges and sides, is null.

By considering the case of gold nanorods that are shined by polarized electromagnetic field and by assuming that the gold nanorod as the first medium with dielectric function ε_g and the surrounding photopolymerizable solution as the second medium with dielectric function ε_{ps}; The boundary conditions for the electric field across material interfaces (gold/photosensitive solution) are written as in Eq. 4.2:

$$E_{t_{ps}} - E_{t_g} = 0 \quad \text{and} \quad E_{n_{ps}} - E_{n_g} \neq 0 \tag{4.2}$$

Where E_t and E_n are the tangential and the normal components of the electric field to the surface of gold nanorod, respectively. [101] E_{ps} and E_g are respectively the electric field components in the photopolymerizable solution and in gold.
In words, this means that the tangential components of the electric field are continuous across the interface, while the normal components are not. By referring to our previous demonstration that the electric field inside a metal conductor decreases to reach a null value after a distance of δ, we can thus consider that $\overrightarrow{E}_{inside} = \overrightarrow{0}$. This implies that the tangential components of the electric field on the interface turn out to be zero while the normal ones are different from zero. This leads to the conclusion that whenever a system consisting of metal conductor/dielectric is irradiated by an electric field, the components of the incident field on the boundary surface are null unless they are perpendicular to the interface.

Summing up, it is a classical exercise for a student in electromagnetism to study the behavior of an electric field at the interface between a metal and a dielectric medium. This situation is a simple application case of the boundary conditions for the electromagnetic fields which can be summarized as: the discontinuity of the normal component of the electric field vector at the interface is related to a surface charge density ρ, [101], as it can be seen by Eq. 4.3:

$$E_{1n} - E_{2n} = \frac{\rho_{s,pol}}{\epsilon_0} = \chi \overrightarrow{n}.\overrightarrow{E_0} \tag{4.3}$$

Where E_{2n} and E_{1n} are the normal components of the electric field inside and outside the metal respectively, $\rho_{s,pol}$ is the surface charge density of polarization charges, χ is the metal electric susceptibility, $\overrightarrow{n}$ is the unit normal vector at the considered point of the surface, and $\overrightarrow{P}$ is the induced polarization.

From the same configuration (i.e. a metal/dielectric interface), it is possible to derive the existence condition of a surface wave propagating along the interface. This surface wave, known as a surface plasmon, is associated to the collective oscillation of the surface charges and is a resonant phenomenon. As stated in Chapter three, surface plasmons are currently the focus of a strong interest due to their

appealing properties for solar energy harvesting, [85] optical manipulation, [8] efficient light generation, [9, 88, 89] nanosensing, [10] and nanoscale light guiding. [57]

The difference between the *resonant* (surface plasmon) and *off-resonant* cases can be understood as follows. Away from the resonance, we are essentially in a quasi-static situation, with the charges oscillating in time at the exciting field frequency (AC field). At resonance, there is a wave propagating along the interface, the so-called surface plasmon wave, meaning that electrons are oscillating both in time and space along the interface. In the case of metallic nanoparticles, different surface plasmon resonances may exist; each one corresponds to a given mode of the electromagnetic field, with its own associated field distribution. [107] The intensity of the associated field can be orders of magnitude higher than the incident field due to the resonant nature of the phenomenon. In off-resonance case, there is still an associated field localized at the interface but its amplitude is dramatically lower than in the resonant case. A remarkable exception is the so-called lightning rod effect [108] which arises from geometrical singularities: near a sharp protrusion on a metallic surface the electric field reaches high intensity values. This effect has been experimentally observed in case of metal nanorods and tips. [109, 110] It is very polarization-dependent and this dependence is related to the above-evoked field boundary conditions. Apart the lightning rod effect that benefits from charge density enhancement at singularities, [111] only few experimental reports on non-resonant effects have been reported, [39, 112] because off-resonant excitation generates weak fields that are extremely difficult to measure.

In this Chapter, we report on imaging the non-resonant field on a metal/dielectric interface on gold nanorods. [107] Our approach relies on the use of a photopolymer that undergoes photo-crosslinking to embody the profile of the electric field intensity. The used photochemical approach has already been employed to image the resonant behavior of metallic nanoparticles (i.e. their surface plasmon resonance), as it was discussed in Chapter three. In the case of non-resonant structures, the local field enhancement stems from the surface charges created by the electric field discontinuity at the metal/dielectric interface. This allows us to present nanoscale-resolution maps of the spatial distribution of the surface charge density. [107]

4.3 Sample fabrication and characterization

Gold nanorods were fabricated on a glass substrate by electron-beam lithography and lift-off techniques. The details of this fabrication technique can be found in Chapter two.

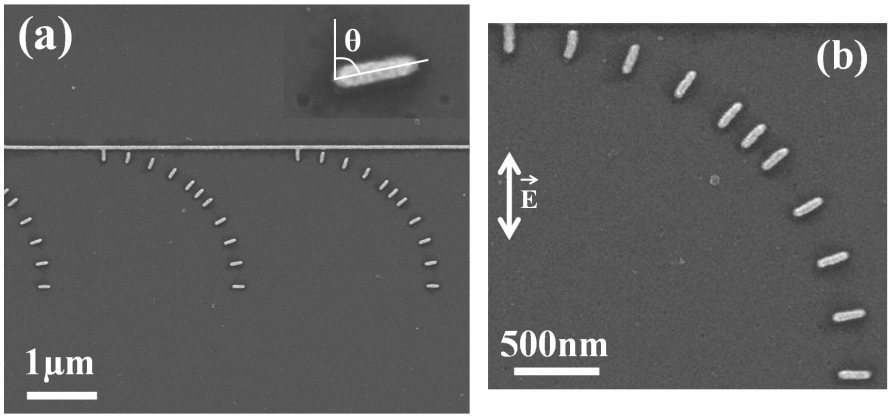

Figure 4.1: Representative scanning electron micrograph showing several regions consisting of gold nanorods that are distributed in quarter of circles in (a). (b) Close-up image showing eleven differently oriented nanorods.

The structures are manufactured so that they form quarter of circles as it can be shown in Figure 4.1(a). Each quarter of circle consists of eleven nanorods oriented differently with respect to the vertical direction, alternating from $\theta = 0°$ for which the major axis of the rod is parallel to the vertical direction, to $\theta = 90°$ for which the major axis is perpendicular to the vertical direction. It must be noted that θ indicates the angle between the nanorod major axis and the vertical direction, as indicated in the inset of Figure 4.1(a). The nanorod orientation is illustrated in the scanning electron micrograph shown in Figure 4.1 and the incident electric field direction is represented by the white arrow in Figure 4.1 (b).
The importance of this distribution is to have, on the same sample, particles whose major and minor axes are differently oriented with respect to the fixed incident light polarization. This will guarantee that all metal nanoparticles have almost the same crystalline structure and that they will be irradiated under the same conditions. Moreover and after characterizing the sample and accomplishing the irradiation, no additional samples are needed since all informations can be gathered from this distribution. Finally, this nanoparticle configuration will save time and samples.
The typical length and width of the nanorods were approximately 235 and 85 nm, respectively. The thickness of the nanostructures is set constant and equals to 28 nm.

In a first step, far-field scattering spectra were calculated using the discrete dipole approximation method (DDA) for a gold nanorod to acquire the optical properties of this structure. These calculations were achieved by Prashant K. Jain, our collaborator at the University of California Berkeley.
Nanorod dimensions were chosen to be equal to those measured experimentally, namely 28-nm thick, 88-nm width, and 238-nm length (including semi-circular end-caps of radius 44 nm). The DDA simulations were performed using DDSCAT 7.0 with a tolerance of 1×10^{-5}. The target was defined by a cubic lattice of virtual dipoles with an inter-dipole/mesh spacing of 2 nm. The dielectric function of gold was described by the experimental data for bulk gold from Johnson and Christy without any additional size correction. The spectra for two distinct incident light polarization directions, i.e., one along the long-axis of the nanorod, and the other along the short-axis, were summed together to result in a spectrum of the scattering efficiency, showing both the short- and the long-axis LSPR modes.

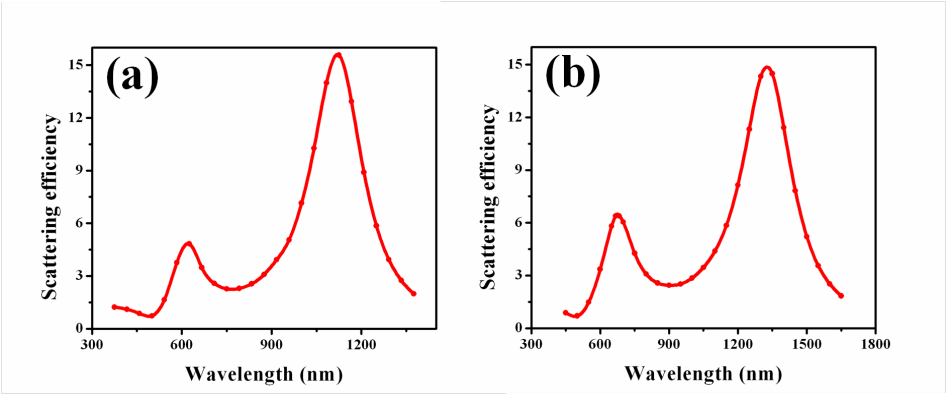

Figure 4.2: Far-field scattering spectra for a single gold nanorod calculated using DDA (a) in air and (b) in photopolymerizable solution.

Spectra were calculated for two different values of the effective medium refractive index:
a. $n_{eff} = 1.25$, for nanorods on a glass substrate, n $\sim$ 1.5, in air with n $\sim$ 1, before immersion in the photopolymerizable solution.
b. $n_{eff} = 1.5$ for nanorods on a glass substrate, n $\sim$ 1.5, embedded in the photosensitive solution with n $\sim$ 1.5.

Figure 4.2 illustrates the far-field scattering spectra which reveal the response of both nanorod axes. The spectrum reveals the minor and major axes surface

plasmon responses, which are located around 662 nm and 1313 nm, respectively. The scattering efficiency of the minor axis is obviously lower than that for the major axis due to the difference in size between the two axes, 85 nm to 235 nm. Figures 4.2 (a) and 4.2 (b) correspond to the gold nanorod scattering spectrum in air and in photopolymerizable solution, respectively. [107] It should be highlighted that a red-shift can be noticed in the response of LSP of both axes when passing from air to photosensitive solution that has a higher effective refractive index. The influence of the outer medium on the plasmon resonance response was already pointed out in Chapter one.

4.4 Description of the used Approach - Imaging the non-vanishing components of the electric field

Our approach relies on a nanoscale photopolymerization prompt by local field intensity in the vicinity of gold nanorods. After morphological characterization using scattering spectroscopy and AFM, the nanorods are coated with a photopolymerizable solution drop and illuminated out of their resonance, at a wavelength that matches the maximum of the absorption spectrum photopolymerizable formulation but sufficiently off-resonant from the nanorod surface plasmon responses. Namely, we used 530 nm as incident wavelength along this experiment. As it can be seen on Figure 4.3, the optical exposure is performed under normal incidence with a 1-cm wide linearly polarized homogeneous laser beam, provided by an Ar:Kr laser source. At the sample level, the polarization of the incident field was kept vertical (y-direction in the plane of the paper), for all the results presented in this Chapter.

The visible-sensitive free radical photosensitive solution is characterized by a threshold dose below which no polymerization can occur. [19, 20] As for Chapter three, the exposure dose is chosen to be smaller than the threshold dose to guarantee that no chain reaction is initiated by the far-field incident laser beam. Namely, the exposure dose was chosen to be 65% of the threshold dose to avoid any far-field photopolymerization. However, the threshold dose might be overcome by any local field enhancement originating from gold nanorods. In such a case, the polymerization chain reaction is initiated leading to reticulation. The polymerized parts are then revealed by a rinsing procedure which consists of removing any non-reticulated monomer. Finally, AFM characterization is carried out and compared to AFM images obtained on the same gold nanorods before the

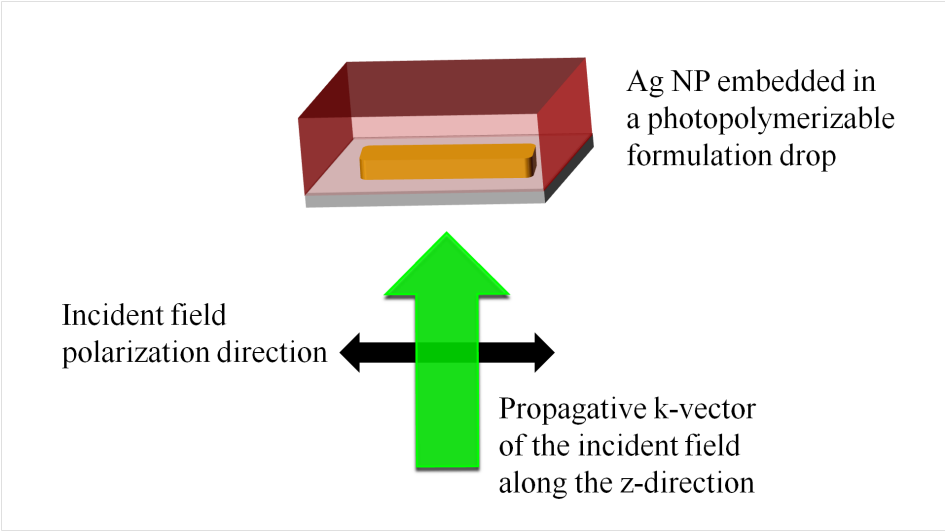

Figure 4.3: Scheme reminding the used experimental set-up for optical exposures.

photopolymerization procedure. Such a differential imaging approach accurately depicts the spatial distribution of the polymerization resulting from the reticulation process, while circumventing the apparent increase of the polymer depth due to convolution with the AFM tip. The overall resolution of this technique is better than 5 nm, [19] meaning that it is able to imprint enhanced fields localized within regions smaller than 5 nm.

The procedure was performed on several samples, each sample consisting of eleven differently oriented gold nanostructures. We will show that gold nanorods exhibit an elongation whenever the component of the electric field along the unit normal vector $\overrightarrow{n}$ is not zero. To the best of our knowledge, the local imaging of the non-vanishing components of the electric field at the metal nanoparticle/dielectric interface, while the nanoparticle is irradiated off-resonance, has never been achieved before. [107]

In order to highlight the elongation of the major and the minor axes of the gold nanorod emanated from the localized photopolymerization, we subtract the AFM images for the same single nanorod before and after the complete procedure (deposition of a drop of the photosensitive solution, laser illumination and rinsing). Figure 4.4(a_0) shows an AFM image for a gold nanorod before the procedure while Figure 4.4(a_1) shows the AFM of the same nanorod after the procedure. Figure 4.4(a_2) is the subtraction of Figure 4.4(a_1) and 4.4(a_0). Such differential image accurately depicts the spatial distribution of the polymerization resulting

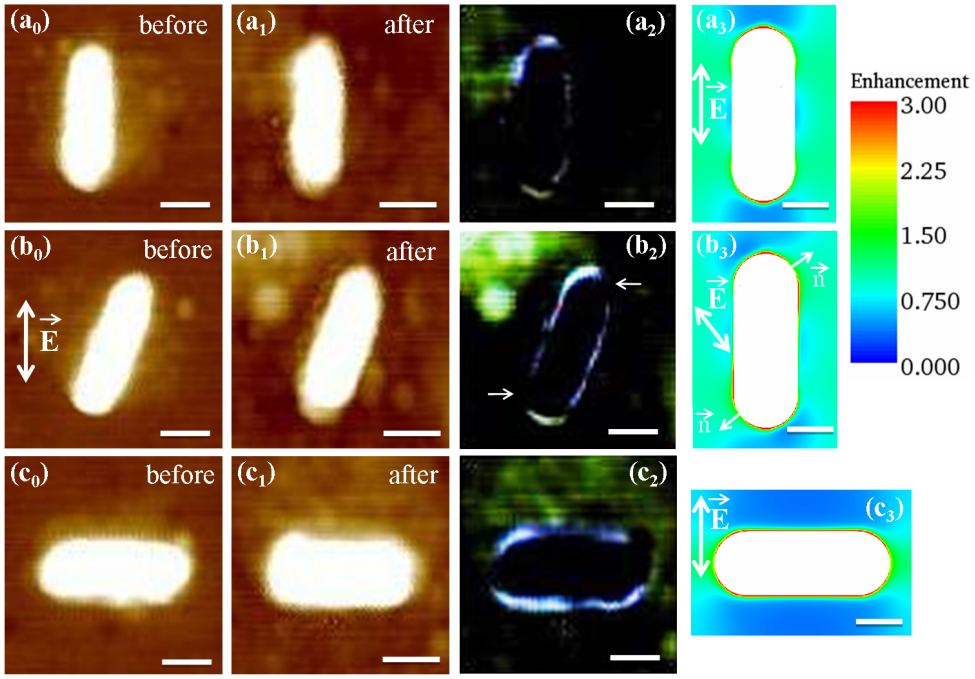

Figure 4.4: Highlighting the elongation of the minor and major axes of the nanorod. The three rows of this figure presents three nanorods oriented differently with respect to the incident polarization; row 1, 2 and 3 corresponds to a nanorod orientation of 0°, 22.5° and 90°, respectively. The first column of this figure shows the AFM image of the gold nanorod before the procedure while the second column corresponds to the AFM images after the procedure. The third column illustrates the differential images that correspond to the subtraction between the first and the second column. Column four represents the near-field calculations performed using FDTD on a GNR, embedded in a medium refractive index of 1.485, for differently oriented incident polarization indicated by the white arrow, together with a linear color legend. The fixed incident field polarization is represented by the white arrow drawn in panel (b_0) and the error bars correspond to a distance of 90 nm. (Reprinted with permission from Deeb, C. *et al.*, J. Phys. Chem. Lett., 2, 7-11 (2011). Copyright 2011 American Chemical Society).

from the reticulation process, while circumventing the apparent increase of the polymer depth due to convolution with the AFM tip. Figure 4.4(a_2) clearly reveals the points at the surface of the nanorod where the effective dose exceeded the threshold dose, and hence where polymerization occurred. [107]

This experiment has been achieved for three gold nanorods with three different orientations with respect to the vertical incident polarization. Figure 4.4(b_0) and 4.4(b_1) represent the AFM images for a 22.5° inclined nanorod before and after the procedure, respectively. While Figures 4.4(c_0) and 4.4(c_1) belong to the third nanorod with an orientation of 90° with the polarization (major axis is perpendicular to the polarization). Figures 4.4(b_2) and 4.4(c_2) are the differential experimental image resulting from the subtraction of Figures 4.4(b_0) and 4.4(b_1) and Figures 4.4(c_0) and 4.4(c_1), respectively.

4.5 Interpretation of our results - Parametric study

It is clear from the differential AFM images (third column of Figure 4.4) that a very localized polymerization occurs at the nanorod surface, whose extension depends on the relative orientation of the nanorod with respect to the polarization axis. [107]
It is worth noticing that the polymer extension is maximum when the local vector normal $\overrightarrow{n}$ to the nanorod surface is aligned with the polarization direction as it can be seen, for example, at the ends of the nanorod in Figure 4.4(a_2) and at the nanorod sides of Figure 4.4(c_2). Conversely, the polymer extension is null when the normal vector is perpendicular to the incident polarization as one can see at the nanorod sides on Figure 4.4(a_2) and at the nanorod ends in Figure 4.4(c_2).
The tilted nanorod is an intermediate case of Figures 4.4(a_2) and 4.4(c_2) and thus illustrates the vanishing and the non-vanishing electric field components. It is quite remarkable that only two regions on the inclined nanorod surface show no polymer extension, as pointed out by the two white arrows on Figure 4.4(b_2). These specific regions present a local unit normal vector $\overrightarrow{n}$ that is perpendicular to the incident polarization, while in all other regions, the incident field has a non-zero projection onto $\overrightarrow{n}$. This implies that any drastic change in the direction of the normal vector with respect to the incident field, which might be due to an imperfection during the e-beam procedure or to an impurity on the nanorod surface, is exhibited by our photopolymerizable approach based on surface charge densities.

We propose that the local polymerization is driven by the surface charges created by the electric field discontinuity at the rod interface, following the usual boundary condition given by Eq. 4.3.
The surface charges create in turn their own electric field, which is responsible for a small field enhancement in the vicinity of the rod surface and consequently

allows photopolymerization. In the following, we present the rationale supporting our proposal, on the basis of two different arguments.

- Dependence of the NP elongation on its orientation

First, we present the observed nanoparticle (NP) elongation l as a function of its orientation θ with respect to the incident field polarization (vertical in-plane direction). The elongation was measured along the major and minor axis of the rod and was averaged over four different nanorods. Again, the NP elongation is calculated from the subtraction between the size of the same nanorod before the procedure from that after the experiment.

The procedure followed to measure the value of the nanorod elongation along the major and the minor axes is schematized in Figures 4.5 (a) and 4.5 (b), respectively. The schemes show that for the same value of the angle θ, the length and the width of the nanorod were constantly measured then averaged over four different nanorods. It should be highlighted that, for all the acquired measurements, the direction of the incident field was always kept vertical as it is represented by the black arrow on Figures 4.5 (a) and 4.5 (b).

Along the major axis (red triangles in Figure 4.6 (a)), the elongation is maximum for an orientation angle $\theta = 0$, namely a rod aligned with the polarization direction, and decreases when the rod is tilted, reaching zero (no polymerization) when the rod is perpendicular to the polarization direction ($\theta = 90°$). Conversely, along the minor axis (red triangles in Figure 4.6 (b)), the elongation is maximum when $\theta = 90°$. To understand this behavior, a phenomelogical model can be developed.

Above the threshold, the polymer extension is roughly proportional to the field intensity at the rod surface I_{surf}, that is $l = \alpha I_{surf}$, where α is a parameter depending on the photophysical properties of the polymer and I_{surf} corresponds to the surface field intensity. The electric field at the gold nanorod surface is the sum of the incident field E_0 and the field $\chi \overrightarrow{n}.\overrightarrow{E_0}$ created by the surface charges. [107] Summing the fields coherently and projecting them along both gold rods axes yields respectively to the following intensity expressions given by Eqs. 4.4 and 4.5:

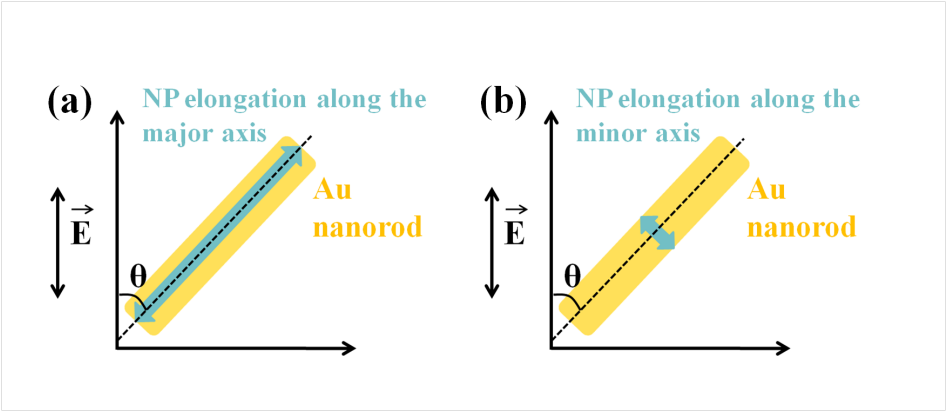

Figure 4.5: (a, b) Representative scheme showing the value corresponding to the NP elongation along the major and the minor axis, respectively. The vertical black arrow illustrates the incident polarization.

$$I_{surf}^{M} = I_0(1 + \chi^2 cos^2\theta + 2\chi cos\theta \times cos\phi) \tag{4.4}$$

and

$$I_{surf}^{m} = I_0(1 + \chi^2 sin^2\theta + 2\chi sin\theta \times cos\phi) \tag{4.5}$$

Where M and m stand respectively for the major and the minor axes and ϕ is the phase difference between the incident field and the induced dipole field.
On the basis of this model and assuming that the field scattered by the dipoles constituting the gold nanostructures to be in phase with the incident field, we have fitted the experimental elongation along the major axis by $l = l_0(1+\chi^2 cos^2\theta+2\chi cos\theta)$ (black line in Figure 4.6 (a)), where χ is the only fitting parameter. $l_0 = \alpha I_0$ was set to be equal 1 nm representing the minimum elongation that can be detected using AFM (corresponding to the AFM lateral resolution). The agreement is good, and we obtain $\chi = -5.2 \pm 0.1$.

Along the minor axis, the fit function was chosen as $l = l_0(1 + \chi^2 sin^2\theta + 2\chi sin\theta) + l_1$, where l_1 is an offset. The coefficient l_0 was set at the same value found in case of the major axis, since the incident intensity is the same along both axes. We found $\chi = -5.8 \pm 0.3$ and $l_1 = 8.3nm$. Again, a good agreement is observed between the fit and the experimental data. The origin of the offset is explained as follows. Along the minor axis, the gold rod surface in contact with the photopolymerizable solution, namely the nanorod sides, is much greater than the surface of contact along the major axis which is limited to the rod ends. This

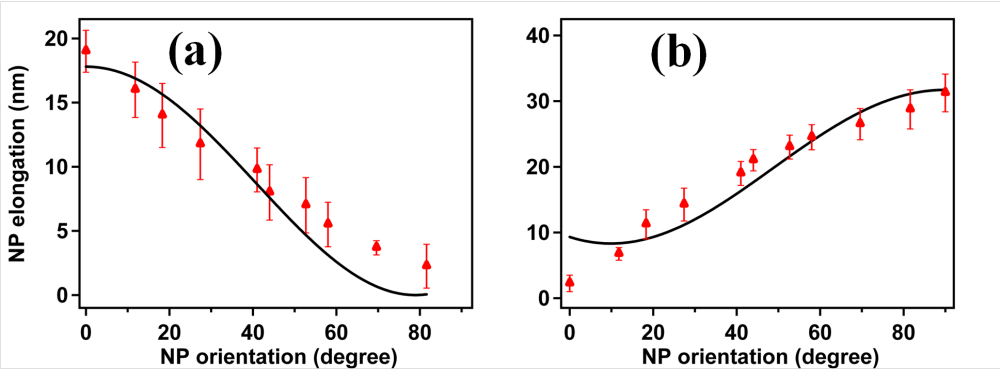

Figure 4.6: Dependence of the nanoparticle elongation on its orientation with respect to a vertical in-plane direction. (a) Red triangles: Experimental major axis elongation of gold nanorods averaged from several samples. Black solid line: fit by $l = l_0(1 + \chi^2 cos^2\theta + 2\chi cos\theta)$ with $\chi = -5.2 \pm 0.1$. (b) Same for minor axis with $l = l_0(1 + \chi^2 sin^2\theta + 2\chi sin\theta) + l_1$ as fit function, where $\chi = -5.8 \pm 0.3$ and $l_1 = 8.3nm$. The error bars of the red triangles represent the standard experimental deviation. (Reprinted with permission from Deeb, C. *et al.*, J. Phys. Chem. Lett., 2, 7-11 (2011). Copyright 2011 American Chemical Society).

induces a higher probability of adhesion of the formulation on the rod sides, and a tiny layer of polymer may remain attached to the gold nanorods sides after the rinsing procedure, even in the absence of photoexcitation. This is why we observe a 3-nm elongation of the minor axis at $\theta = 0^o$. It is worth noticing that equivalent values for χ were found for both axes. From the susceptibility, we can deduce the real part of the dielectric constant of gold since $\epsilon_r = 1 + \chi$. Averaging both axes, we obtain $\epsilon_r = -4.5$, in notable agreement with reported values for gold at $\lambda =$ 530 nm. [1] This model constitutes the first evidence that the polymer elongation is directly related to surface charges created on the gold nanorods through gold susceptibility and permittivity. [107]

- Near-field FDTD Simulations

To confirm our proposal, we performed numerical simulations to compute the near-field enhancement at the gold nanorod surface. These calculations, carried using FDTD method, were made by Prashant K. Jain through a recent collaboration with our team. Three-dimensional (3-D) FDTD simulations were performed using EM EXPLORER 2.0 for a gold nanorod having a width of 88 nm and a length of 238 nm, including semi-circular end-caps of radius 44 nm. A 3-D simulation domain 300-nm x 200-nm in size with a 2-nm mesh and default analytical

absorbing boundary conditions was employed. Bulk refractive index values for gold were also used from Johnson and Christy. The medium was assumed to be uniform with n = 1.485 and k = 5.13×10^{-3}, based on the known absorption coefficient of 7.55×10^{4} $M^{-1}cm^{-1}$ for the photopolymerizable solution and a dye concentration of 0.5%.

The nanorod was illuminated by a plane-wave with a wavelength of 530 nm and a propagative k-vector along the nanorod thickness. Simulations were performed for two extreme incident polarization directions, i.e., one along the long-axis of the nanorod corresponding to 0°, and the other along the short-axis corresponding to 90°. Calculations for intermediate cases, where the incident field makes angle of 22.5° with the nanorod major axis, were also executed. Field intensity values were normalized by those from a blank run without the gold nanorod in order to obtain the field intensity enhancement. The total near-field intensity $(E_x)^2+(E_y)^2+(E_z)^2$ was calculated at every grid point using a convergence tolerance of 0.01 and 100,000 maximum iterations. Field intensity values were normalized by those from a blank run without the gold nanorod in order to obtain the field intensity enhancement. For each incident polarization direction, the enhancement in the x-y plane was mapped on a linear color scale.

The fourth column of Figure 4.4 shows the result of the near-field simulations using FDTD, where Figures 4.4 (a_3), 4.4 (b_3), and 4.4 (c_3) correspond respectively to an incident field polarization along the nanorod major axis, making an angle of 22.5° with the major axis and perpendicular to it.
Figure 4.4 (a_3) confirm that for incident polarization along the major axis, this leads to surface charges and near-field at nanorod ends. While for a polarization along the minor axis, surface charges and near-field are concentrated at nanorod sides as it can be seen on Figures 4.4 (c_3). These results confirm our experimental observations illustrated in Figures 4.4 (a_2) and (c_2), respectively.

The $\theta = 22.5°$ case, as it is shown in Figure 4.4 (b_3)), is particularly instructive, where it is worth highlighting that no polymerization was experimentally observed at two precise regions on the gold nanorod surface (white arrows in Figure 2b2), exactly where $\overrightarrow{n}$ is perpendicular to $\overrightarrow{E}$. These observations are attributed to the fact that no surface charges are excited at locations where the unit normal $\overrightarrow{n}$ is perpendicular to the incident field direction, resulting in the enhancement factor at these locations being insufficient to overcome the threshold dose for polymerization. [107] The field enhancement distributions obtained from FDTD clearly reflect this. For each of the polarization directions (Figures 4.4 (a_3)), 4.4 (b_3)))

and 4.4 (c_3)), at all of the locations on the gold nanorod where $\overrightarrow{n}$ is perpendicular to $\overrightarrow{E}$, the field enhancement is significantly lower than the maximum field enhancement on the nanorod surface.

It is worth emphasizing that local heating of the nanorod may create radicals and hence trigger polymerization. However, because we are illuminating the gold nanorods off-resonance, the structures are not expected to absorb any significant light, and hence, the local temperature increase is expected to be negligible. Additionally, we believe that the effect of local heating of the metal nanorod will be homogeneous and will not depend on the incident polarization. [113] This implies that thermal polymerization, if any, will be induced at every single point of the metal structure regardless of the unit normal vector direction with respect to the incident field polarization.

4.6 Conclusions

In conclusion, we have reported on nanoscale photopolymerization on the surface of non-resonant metal nanostructures. The photopolymerization is triggered by the localized electromagnetic field enhancement associated with the surface charge densities supported by the nanorod sides.
The controlled photopolymerization at the nanometric scale relies on the knowledge of the threshold dose of the photosensitive formulation; reckoning on the high density of charges resulting from the discontinuity of the normal components of the electric field at the interface metal/dielectric, we demonstrated that the effective dose at some precise positions exceeds the threshold dose of the photopolymer, and hence polymerization process is initiated.

To the best of our knowledge, this is the first time that the spatial distribution of the surface charges is unveiled. This also demonstrates the versatility of the photochemical imaging approach, which is sensitive enough to imprint weak non-resonant fields with nanoscale resolution, thus allowing a direct visualization of the surface charge density distribution with a 2-nm resolution.

Chapter Five

Evidence of Two Regimes in Plasmon-Based Free-Radical Nanophotopolymerization: Dye and Oxygen Roles

5.1 Introduction

Photophysical interactions between metal nanoparticle/photochemical system have been studied in details in preceding Chapters three and four. Two fundamentally different types of illumination were used: resonant irradiation matching the surface plasmon response of metal nanostructures and an off-resonant one. The experimental results achieved in these two Chapters elucidated, to a great extent, the behavior of the metal nanostructures from the point of view of their optical attributes.

In this Chapter, we will take a nanometric look at the photochemical system itself. In particular, we will discuss its behavior as a function of the diffusion of the constituent species, namely dye and oxygen, in response to different irradiation parameters. As a matter of fact, better understanding and optimization of these photochemical processes are crucial for achieving accurate control of photopolymerization at the nanoscale, and thus significantly increasing the resolution of light-induced photofabrication.
In this Chapter, we will present results which prove that our near-field photopolymerization approach can serve as a super high-resolution tool to understand the diffusion of dye, and that of oxygen, at the nanometric scale.

Such studies not only demonstrate that we can employ the near-field to break the diffraction limit and achieve nm-scale resolution but also constitute, from a more fundamental point of view, a unique opportunity to investigate nanophotochemistry.

In this regard, we have determined the physico-chemical parameters and phenomena controlling the spatial extent of the photopolymerization process. We surprisingly recognize that the dye diffusion plays a crucial role at the nanometer scale, as opposed to previous studies at the micrometer level, [72, 75, 76, 114] where its role was fairly neglected.

5.2 Experimental basics

The studies accomplished in this Chapter rely on the same approach that was already used in previous Chapters and which we will remind its important steps here.
Colloidal silver nanoparticles, stabilized by citrate groups, are anchored on the surface of a glass substrate that was previously functionalized to create an amine termination. Additional information on glass substrate's functionalization can be found in Chapter two. In a first time, the metal structures are characterized using spectroscopy in order to have their surface plasmon resonance and using AFM.
A photosensitive solution, namely the same chemical system used in Chapters three and four, is characterized by means of far-field studies in order to determine its threshold dose. This parameter is defined as the needed dose to initiate the reaction process and hence polymerize. Thus and in order to prevent far-field photopolymerization, the threshold dose should never be overcome. The photopolymerizable solution is then deposited on the glass substrate with metal structures on it.

Laser exposures were performed at 514 nm using a linearly polarized homogeneous beam with 1-cm diameter. The incident wavelength was chosen to match the plasmon response of the colloidal nanoparticles and the absorption spectrum of the dye. As already mentioned, the incident dose should be smaller than the threshold one to avoid any far-field polymerization. Namely for the results of this Chapter, the incident dose was varied between 7% and 63%.

Under these illumination conditions, no polymerization occurs in far-field and only the enhancement of the resonant dipolar response of the silver nanoparticles allows overpassing the threshold of polymerization. Thus the colloids are actually behaving as light nanosources that are providing the needed amount of "lack" energy by producing highly confined electromagnetic fields and transferring it to the dye to start the cross-linking of a free-radical photopolymerizable system.

The sample is then rinsed with ethanol and isopropanol to remove the unpolymerized monomer hence revealing the hybrid nanoparticles. The hybrid system consists of the silver particle and two lobes of polymer well directed with the incident field polarization. After exposure, the sample is characterized again using AFM and the nanoparticle elongation, due to the polymerization extent, is evaluated by subtracting the nanoparticle width, in the polarization direction, before and after the complete procedure.
A typical example showing the complete procedure of near-field polymerization, where the colloidal nanoparticle gets elongated after irradiation, was shown in Chapter three through Figure 3.6.

The photoinitiating system composed of Eosin Y and the MDEA, associated to an acrylate monomer, was previously used in several applications like holography, laser direct writing self-guiding photopolymerization. This system exhibits a suitable sensitivity at 514 and 532 nm, and it is very flexible as it is possible to modify the components independently to adjust the physical and the chemical properties of the formulation, namely, viscosity, spectral sensitivity, or polymerization threshold. A simplified scheme of the molecular pathway leading to photopolymerization is shown in Figure 5.1. The absorption of a photon leads first to the excited singlet state of the Eosin, and then to the triplet state by intersystem crossing. From the triplet state, the dye can react with the amine to produce the first radical able to induce the free-radical polymerization of the methacrylate monomer. Since the monomer is trifunctional, a rapid crosslinking of the polymer network is usually observed.

Alternatively, another pathway is quite important to be considered. The left part of the scheme describes all the inhibition processes that take place. They are mainly due to oxygen dissolved in the photopolymer. Oxygen can indeed react with the triplet state of the dye, or with radicals to create peroxide radicals that are not active for polymerization. Usually, in free-radical polymerization, these later processes are considered to be negative since they decrease the efficiency of the global polymerization process, hence introducing an inhibition period, and in some cases, a limited final monomer conversion. In micro and nanofabrication, such molecular phenomenon can be advantageously used to sharply control the polymerization volume. The consequence of the oxygen inhibition is the introduction of a threshold of polymerization that can precisely determined under precise conditions.

Both pathways lead to the transformation of Eosin to a protonated Eosin radi-

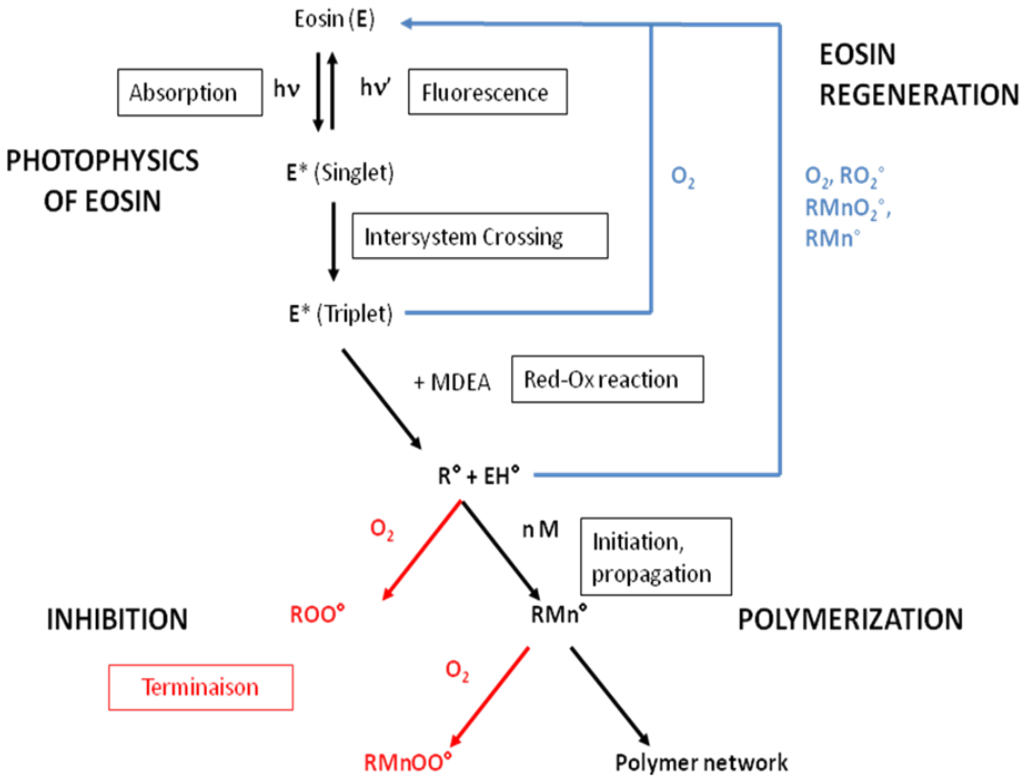

Figure 5.1: Scheme illustrating the photoinduced polymerization of the methacrylate monomer, the inhibition processes, and the Eosin Y regeneration pathways.

cal. This radical is known to be ineffective for initiating polymerization. However, several reactions of this radical have to be considered: First, it can react with another protonated Eosin radical to regenerate an Eosin molecule in the leuco form. The later form is not absorbant at 532 nm, and the consequence of this reaction is the progressive bleaching of the Eosin formulation. Second, the protonated Eosin radical can undergo a disproportion reaction with other radicals (deprotonated amine radical, peroxide radicals or free-radicals of the growing polymer chains), where in this case, the Eosin is regenerated to its fundamental state. Such process regenerate the Eosin in an active state that can photosensitized again other MDEA reactions.

A very precise control of the spatial extent of the photopolymerization, based on localized plasmons and surface charge density, was already demonstrated in previous Chapters. [19, 107] We also proved that this technique constitutes an exciting experimental setup to investigate the effect of high confinement on pho-

topolymerization processes. The aim of this Chapter is to illustrate that by observing the spatial extent of the polymerization reaction under different illumination conditions, it was possible to explore the physico-chemical processes that govern the nanofabrication. Throughout the results presented here, we will show that our near-field polymerization approach gave us the opportunity to highlight some phenomena available only at the nanometric scale, namely the dye diffusion and dye regeneration.

5.3 Experimental Results and Interpretation

Based on the experimental approach described in the previous section, we performed several studies where we illustrate the effect of different parameters on the polymerization extent, namely the incident power, the exposure time, and the dye concentration. An additional experiment was carried out by our collaborators at Mulhouse to reinforce our results. It should be noted that the interpretation of the results presented along this section was done in collaboration with our chemist coworkers who helped us to better understand the physico-chemical processes that are taking place.

5.3.1 Study at constant dose: Influence of the incident power and the exposure time on the nanoparticle elongation

The aim of this study is to clarify the role of both, the incident power and the exposure time, on the polymerization extent, at constant dose. The threshold conditions of our chemical system were at P = 2 mW/cm^2 during t = 1s. We decided to work at 70% of these parameters to prevent any polymerization due to a far-field illumination or to any roughness present on the substrate surface. Hence and for t = 0.7s (70% of 1s), we varied the incident power so that the exposure dose goes from 7% and 63%. Similarly, at P = 1.4 mW/cm^2, which is 70% of 2 mW/cm^2, we varied the time to have an exposure dose values between 7% and 63%. It should be noted that the exposure dose is the product of the incident power and the time of exposure.
For every single dose value, the silver colloids are characterized, illuminated below the chemical solution threshold dose, rinsed and re-characterized by AFM. Then the nanoparticle elongation which corresponds to the polymerization extent along the vertical direction of the incident field (vertical direction in the plane of the page) is deduced by subtracting the particle width before the procedure from that

after the procedure.

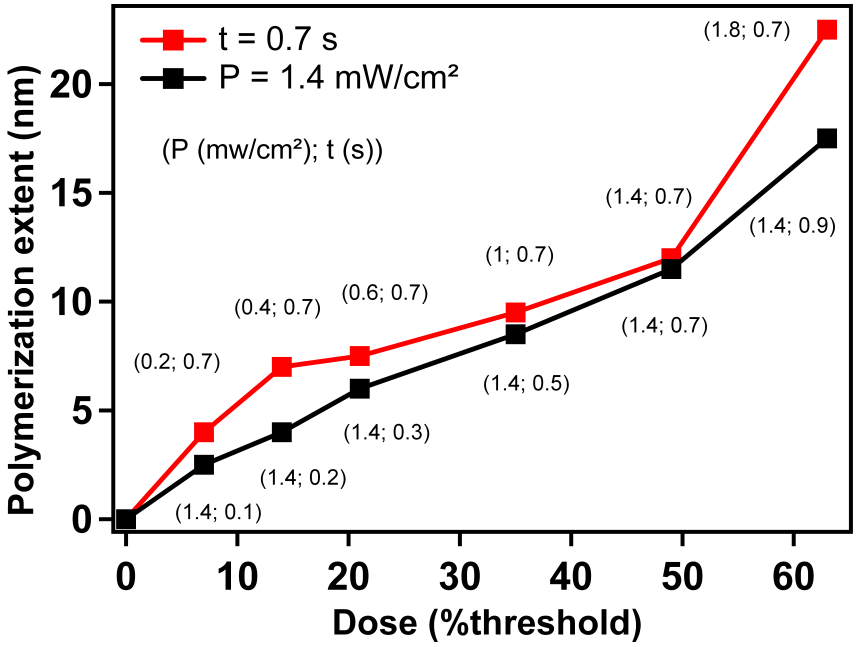

Figure 5.2: Evolution of the spatial extent of the near-field photopolymerization with the dose, for constant incident power or irradiation time. The black trace shows the polymerization extent as a function of the incident dose with the incident power density as constant parameter (1.4 mW/cm^2), while the red trace illustrates the response of the polymer at constant irradiation time (0.7 s).

Figure 5.2 illustrates the result of this study, where the evolution of the spatial extent due to the near-field photopolymerization is plotted as a function of the incident dose, while the incident power or the irradiation time is kept constant.

On the black curve, the power density is equal to 1.4 mW/cm^2 and increasing irradiation times are used between 0.1 and 0.9 s. This experiment gives a direct visualization of the kinetic of growth of the polymer lobes. The dose is given in % of the threshold dose of polymerization. As expected, one can observe the increase of the polymer extension with irradiation time. It is worth noticing that the trend is almost linear and the thickness of the polymer can be tuned between 3 and 18 nm demonstrating, as it was already done in Chapters three and four, the high control of the spatial extent of the polymerization reaction. Considering the irra-

diation wavelength used here, this corresponds to a $\sim \lambda/200$ resolution, which is obviously far from the diffraction limits predicted by the Rayleigh criterion.
The response of the system is also evaluated in different conditions, keeping the irradiation time constant and varying the power to adjust the dose. The red trace of Figure 5.2 illustrates the photosensitive solution response for a constant irradiation time, t = 0.7 s. Interestingly, the results obtained in this case present some deviation. First, the global trend is no longer linear. Second, it has to be emphasized that below 49% of the threshold dose, the extension of the polymerization is more pronounced for lower power and higher time, at the same constant doses, demonstrating that the polymerization process is favored by low intensity. As expected, the data overlap for both studies (at constant power and constant time), at P = 1.4 mW/cm^2 and t = 0.7 s, illustrating both the control and the reproducibility of our procedure.
Surprisingly, for the highest dose (corresponding to 63% of the polymerization threshold), the extent of the polymerization is favored at higher incident power, which is at first sight in contradiction with our results presented at a dose below 49%. However, this can be argued as follows. Starting from the crossing point of the two curves, a new regime is taking place that is also promoting the photopolymerization process. These results will be fully described along the coming sections.

It is worth noticing the "almost" linear bearing of both traces in Figure 5.2, which is, at a first glimpse, in contradiction with the logarithmic behavior of the size of the polymer wings as a function of the dose, described in Chapter Three. In fact, the same bottle of silver nanoparticles was used for both experiments, yet the experiments presented here were carried out after three months from the bottle shipping. This implies that the metal structures got "old" with time and silver was a bit oxidized, which influenced its enhancement factor. Thus and along the experiments of this Chapter, the variable $F_{max} \times d$ belongs to $[0.5 - 10]$ since d belongs to $[0.05 - 0.8]$ and F_{max} equals ≈ 10. While during the experiments of Chapter Three, $F_{max} \times d$ was belonging to $[1.75 - 28]$ since F_{max} was ≈ 35. Hence and by relying on the equation, $y = \alpha^{-1} \ln(F_{max} \times d)$, we are visualizing in the present Chapter the first part of the logarithmic behavior.
The first conclusion that can be drawn from this study is the evidence that time and power are not equivalent regarding the spatial extent of the polymerization.

In order to go further into the interpretation of these first results, spectroscopic characterizations of the conversion of both dye and monomer were carried out in a separate experiment, at Mulhouse. In particular, it is important to verify that the far-field induces almost no modification of the photopolymer, in terms

of its constituents. Indeed, the bleaching and polymerization kinetics were investigated respectively by UV-visible spectroscopy and fourier transform infrared spectroscopy (FTIR). The bleaching (%) and conversion (%) correspond respectively to the fraction of the dye, and that of the monomer, that was consumed at a given irradiation time. These values were extracted respectively from the relative decrease of the Eosin Y absorbance in the UV-visible spectrum, evaluated at a maximum absorption of 532 nm, and the C=C stretching band in the FTIR spectrum (1635 cm^{-1}).

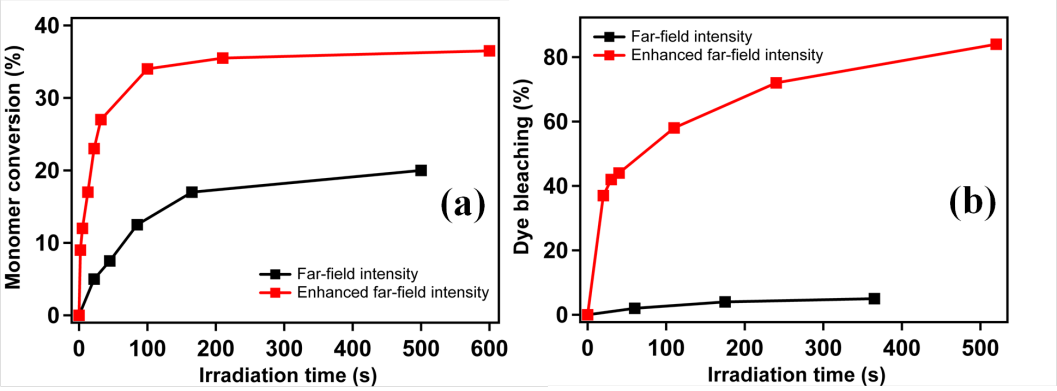

Figure 5.3: Spectroscopic characterizations of the conversion of both dye and monomer using UV-visible spectroscopy and FTIR. a) Kinetic of conversion of the monomer and b) proportion of bleached dye for P = 0.10 mW/cm^2 (far-field conditions) and P = 2.00 mW/cm^2 (Enhanced far-field, estimated from an exaltation factor of 20). Under these conditions, the far-field gel-time was estimated to be 22 s.

The power density of the far-field was here chosen to be 0.10 mW/cm^2. The enhancement factor of this type of metal structures was already evaluated in Chapter three and in [19] and was found to be at least equal to 20. This exaltation corresponds to a power density of 2.00 mW/cm^2 which will be assumed as the maximum field intensity around the silver colloids. Summing up, two different types of irradiation conditions will be distinguished: far-field irradiation elucidating an illumination with an incident dose smaller than the threshold dose, and an "enhanced" far-field irradiation corresponding to an illumination with the parameters of the near-field, namely the power density used in far-field enhanced by a factor of 20. The results of this study are plotted in Figure 5.3.

As expected, the conversions of both dye and monomer exhibit significant dif-

ference depending on the incident intensity. For intensity corresponding to the far-field exposure conditions, the dye bleaching remains at very low level, even for doses much higher than the polymerization threshold time, as it can be seen on the black trace of Figure 5.3 (b). Under these conditions, the conversion of the monomer is also very limited (20 % after 600 s) (see black trace of Figure 5.3 (a)). These results demonstrate that at low intensity, the molecular modifications of the material are extremely low. According to the far-field studies, the threshold of polymerization of the chemical solution was observed at 22 s which corresponds, as it is shown in Figure 5.3 (a), to a monomer conversion of only 5 %. One of the characteristic of the monomer that was chosen is indeed to show a very low conversion needed for cross-linking and, at the same time, sufficient to resist rinsing procedure.
Multiplying the intensity by a factor of 20, because of the dipolar response of silver nanoparticles, creates a significant modification of the kinetics of consumption of monomer and dye, as it can be seen respectively on the red traces of Figures 5.3 (a) and 5.3 (b), when compared to the black traces . It is worth noticing that the non-linearity of the response versus light intensity explains the excellent results in terms of spatial resolution that were obtained. From the results shown in Figure 5.3, a factor of 20 is certainly sufficient to provide no polymerization in the far-field and a complete polymerization in the near-field. A rapid gelification of the photopolymer matrix accounts for a dramatic decrease of the reactive species mobility as soon as the polymerization starts and thus, termination by occlusion process stops the polymerization. However, since the monomer is trifunctional, good mechanical properties can be insured even for these relatively low conversion percentages.

The prominant conclusion that one can deduce from this experiment is that the low intensity far-field irradiation does not affect much the global concentration of dye within the formulation, even with doses leading to a significant bleaching of dye at higher intensity. As discussed in the description of the photopolymerization process, bleaching of Eosin by dismutation of Eosin radical EH° competes with regeneration. Since the dismutation of Eosin is a bimolecular reaction between two protonated Eosin radicals, this reaction is favored by a high concentration of these species which is obtained under high intensity. On the contrary, disproportion reactions with other radicals species will be favored when the concentration of proponated Eosin radical is at a lower level (*i.e.* lower intensity). This implies that for low incident powers, the bleaching of the Eosin is low which leads to high polymerization extents.

On the basis of the results presented in Figure 5.3, the trend observed in Figure 5.2 can be partially explained as follows: For a given dose, the extent of the polymerization was found to be more pronounced for the lower intensity. This result is actually in contradiction with previous results on photofabrication at a higher scale, namely micrometer scale. [76, 114] In previous work, the polymerization extent was indeed found to be significantly favored by an increase of the intensity. This behavior was explained as follow: The inhibition role of oxygen is more pronounced at low intensity (*i.e.* long irradiation times) because the consumption of oxygen is slow enough to allow a continual replenishment from the surroundings. In fact, the polymerization process starts only when the oxygen concentration in the photopolymer droplet is low enough, which implies that the replenishment increases the inhibition time. For higher incident power, the inhibition is less sensitive because diffusion has no time to proceed efficiently. The conclusion of the previous studies is thus exactly opposite to what we have observed here.
This is the reason for which a more complete analysis of the involved processes at the nanometric scale has to be proposed in order to fully analyze the results presented here. Two phenomena can be implied: The dye diffusion and the mechanism of Eosin regeneration. Indeed, these two mechanisms strongly depend on the light intensity that governs the polymerization kinetics.

A simple calculation has to be driven to quantify the concentration of molecules involved at the nanoscale. Taking into account that the typical dye concentration is 0.5 wt.%, and assuming a homogeneous distribution of dye within the photopolymer solution, a volume of 10x10x10 nm^3 contains only 4 molecules of dye. The same volume contains an average of 200 MDEA molecules and 6000 $C = C$ double bonds. Considering these data, it appears that the limited reactant is the dye.

Polymerization can only start if the local consumption of oxygen is high enough to allow an efficient creation of radicals. Typically, oxygen diffusion is about $10^{-12} m^2/s$. If one considers that the length over which a species can diffuse is determined by $\sqrt{Dt}$ where D is the diffusion coefficient and t the time, the length covered by an oxygen molecule during one second is about 1 micron. Local consumption of oxygen is thus very difficult to be achieved at the nanoscale. Under these conditions, the extremely limited number of Eosin dye as compared to the inhibitor concentration will lead to no polymerization.

This behavior can only be explained by, first, considering the dye diffusion. In fact if the polymerization process is dye diffusion limited, then an increase of the irradiation time (corresponding to a decrease of the laser intensity by the same

factor) is favorable for the polymerization, which will be in accordance with our observed results. Although in microfabrication, the dye is usually neglected, yet, here, it has to be taken into account for the following reasons: First, because of a high molecular weight and polarity, the dye diffusion in the monomer matrix is quite slow. However and by reducing the scale to the nanometer, this allows the dye to significantly diffuse into the irradiated volume. Secondly, such process can be efficient since the dye bleaching is negligible in the volume surrounding the near-field region, as it was shown in Figure 5.3 (b)). In the present case, the dye diffusion allows a continual replenishment of the volume surrounding the Ag NPs, which partially explains how polymerization can be favored at lower incident powers. Actually, low intensity corresponds to higher irradiation times, which certainly increases the probability of the diffusing dye that is entering in the near-field volume. It is worth highlighting that this aspect is specific to the nanoscale and linked to the extremely limited number of molecules: At the microscale, the average number of molecules present in the irradiation volume (1000 x 1000 x 1000 nm^3) is obviously greater by a factor of 10^6 and thus the need for diffusion from the polymer droplet into the irradiated volume is not necessary. Under these conditions, the limiting process is the number of photons absorbed by the photopolymer per second and hence, for a given dose, competitive processes such as inhibition by oxygen appear to be relevant.

The second parameter that has to be evoked to explain the nanoscale enhanced polymerization process relies on the dye regeneration pathways described in Figure 5.1. In point of fact and as it was previously discussed, exposures at low intensity favor molecular mechanisms that lead to the regeneration of the Eosin in its active form. Consequently, the dye can absorb a new photon and starts the polymerization of a new chain, after reacting with a MDEA molecule. Such effect explains how a very limited number of Eosin Y molecules can trigger efficiently the polymerization. Moreover, the very limited number of intermediate species linked to the confinement of the reaction lead to a very low probability reaction between two Eosin protonated radicals. Subsequently, the dye bleaching in the near-field volume is quite low and thus one Eosin molecule can undergo a large number of cycles before getting bleached.

In order to confirm this assumption, two additional experiments were carried out. The first one consisted on observing the extent of photopolymerization for different intensities, at a given dose. On the other hand and during the second study, we changed the dye concentration wt % and studied its influence on the

nanoparticle elongation.

5.3.2 Influence of the incident power on the nanoparticle elongation at constant dose

The dose that was chosen here was corresponding to 7% of the polymerization threshold to avoid any undesirable phenomenon provoked by far-field irradiation, as mentioned previously. It can be clearly observed on Figure 5.4 that the decrease of the intensity, which corresponds to an increase of the irradiation time by the same factor, favor the extent of the polymerization reaction. Such results confirm the preliminary conclusion drawn from Figure 5.2 and emphasize the predominant role of the dye diffusion to control the polymerization process. As the intensity is decreased, this gives the time for the dye to diffuse from the photopolymer droplet which constitutes an infinite reservoir of dye, since the dye consumption by far-field irradiation can be neglected. Surprisingly, even for the lower intensity, the polymerization is not affected by the diffusion of oxygen that acts as an inhibitor.

A different behavior is observed for the last data point (14 mW/cm^2) where a slightly higher polymerization volume was obtained. This attitude can be argued by the fact that the effect of oxygen quenching plays an essential role at such high intensity. Indeed, the corresponding irradiation times are too short to allow any replenishment of the dye by diffusion process. Thus, the polymerization is only induced by the excitation of the dyes present in the near-field region at the close proximity of the nanoparticle. Notice that for P=1.4 mW/cm^2 and t=0.1 s, the spatial extent of polymerization was extremely limited. Under these conditions and since oxygen diffuses faster than Eosin Y, this causes a constant quenching of the reactive species which almost stops the polymerization reaction. Ergo, when the power is increased from 1.4 mW/cm^2 to 14 mW/cm^2, the rate of radical production becomes high enough to compete efficiently with oxygen quenching, since the O_2 diffusion starts to be time-limited in this last case. Such behavior that is in agreement with what is usually observed in photoinduced microfabrication accounts for the particularity of the last data point in Figure 5.4. The results of this figure are fully interpreted in the following.

1. $t \gg 1s$ and $P < 0.1$ mW/cm^2

The corresponding results highlight the effect of a low intensity irradiation

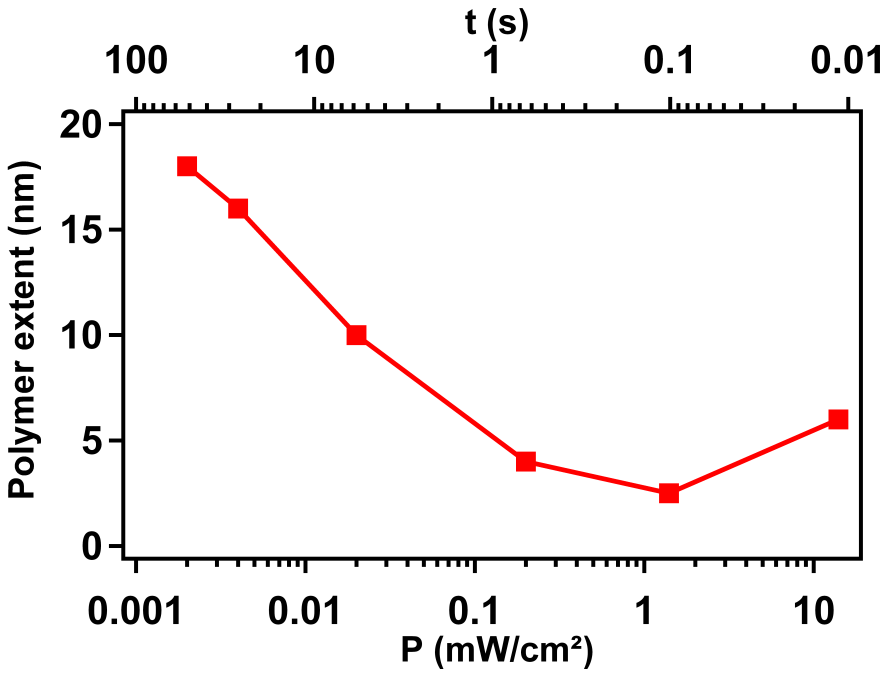

Figure 5.4: Effect of the incident power (and the irradiation time) on the polymer thickness. The dose is kept constant at a low value (7% of the threshold dose), to eliminate any far-field undesirable disturbance.

which corresponds to long exposure time. In this case, the dye concentration in the near-field volume is slightly lower than the Eosin Y bulk's concentration because of diffusion process and conditions favorable for Eosinregeneration. Under such conditions, as long as gelification is not occurring, the concentration of the dye remains at a relatively high level. Reactive species can be created at a rate high enough to counterbalance the oxygen inhibition, despite the continual supply of O_2 by diffusion. This actually induces a low O_2 concentration close to the Ag NPs which then trigger polymerization.

2. t = 1 s

We are here in a new regime since the used illumination time starts to be short compared to the rate of dye diffusion. Thus the dye does not have enough time to access the near-field region. However, the exposure time is still long enough to keep the oxygen concentration at a value sufficient to quench the polymerization. This implies that the few dye molecules, already existing in this region at an instant t_0, consume the O_2 present at this instant and fabricate polymer. Indeed and because of the small number of dye molecules, the polymerized zone is reduced to 2 nm,

as it can be seen on Figure 5.4. Additionally, the rate of diffusion of oxygen is high (because of the small size of O_2 molecules) which means that the zone will be constantly replenished by oxygen and thus polymerization will occur only where the enhancement factor is maximum.

3. t $\ll$ 1 s

When the irradiation time is further decreased, the polymer extent re-increases. In this regime, we are not anymore influenced by the dye diffusion (too short time compared to V_{dye}), yet the oxygen diffusion starts to be the affecting factor. Thus this regime is guided by the competition between the oxygen diffusion and the number of photons per second received by the sample, which was already seen at the micrometer scale. Thus, by decreasing the number of diffusing O_2 molecules, the polymerization thickness would obviously increases. Dealing with this time scale (short irradiation time), polymerization efficiency is higher for higher power because the number of incident photons per second becomes high compared to the oxygen diffusion dynamics.

5.3.3 Influence of the dye concentration on the nanoparticle elongation

In order to confirm the role of dye diffusion, the same previous experiment, at 7% of the threshold dose, were conducted using a formulation with a lower concentration of dye. The results obtained for a solution with a concentration divided by a factor of 5 (0.1 wt. %) are given in Figure 5.5, along with results carried on a 0.5 wt. % Eosin Y solution. The achieved experiments on both formulations were done at 7 % of the polymerization threshold that was determined independently for each single solution separately.

The decrease of the concentration of Eosin Y in the formulation provokes a decrease of the polymerization process efficiency for all irradiation times, as it can be seen on the black trace of Figure 5.5. The clear effect of the dye concentration on the extent of the polymerization can be obviously detected by comparing the red and the black traces corresponding respectively to a 0.5 wt. % and a 0.1 wt. % of Eosin Y in the solution. The local concentration of dye is actually a factor influencing the polymerization process. Unfortunately, it is not possible to test

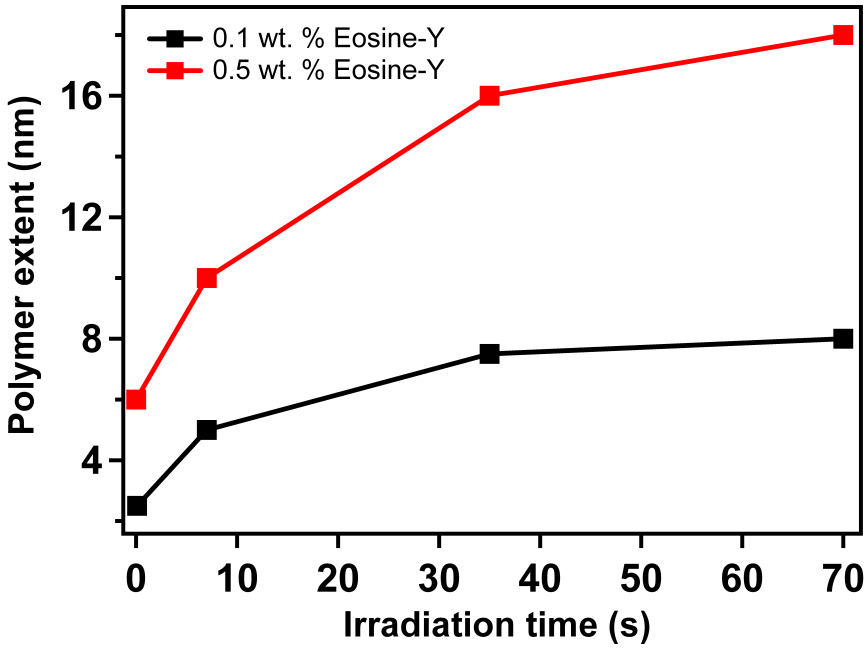

Figure 5.5: Role of Eosin Y concentration on the spatial extent of the polymerization. The red and the black traces correspond to the used dye concentration, respectively fixed at 0.5 wt. % and 0.1 wt. %. The MDEA concentration was set constant at 4 wt. %. The dose was kept constant to a value corresponding to 7 % of the polymerization threshold (evaluated separately for each formulation).

higher concentrations of Eosin because 0.5 wt. % is close to the solubility of the dye in the photosensitive formulation.

Additionally, it must be noted that the 0.1 wt. % dye trace shows a plateau that was obtained for a lateral size of polymer lobes of 8 nm. Such results suggest that the extent of the polymer lobes is directly linked to the initial Eosin concentration and almost independent of the irradiation conditions.
It has to be finally emphasized that a lower concentration of Eosin Y can be considered as favorable if a high resolution of polymer nanofabrication is needed.

5.4 Conclusions

In conclusion, we demonstrated in this Chapter the presence of interesting phenomena at the nanometric scale that were fairly neglected at higher levels. Indeed,

by means of our near-field photopolymerization approach that was faithfully developed in earlier Chapters, we were capable to perceive the existence of interesting events, namely the diffusion and the regeneration of dye, that were ignored in previous micrometer studies since Eosin Y needs too much time to diffuse to the irradiated bright regions. However at the nanoscale level, we proved that the diffusion of dye, together with its regeneration, play a decisive role and hence influence dramatically the polymerization extent. As a matter of fact, the irradiated zone where the effective dose overcomes the threshold dose has nanometric size, in contrary to the size of the bright regions at the micrometer scale, and thus we showed that, by increasing the irradiation time, the dye starts to diffuse to these bright regions to enhance the polymerization process. Furthermore, performing the studies at low intensity guarantees a high probability of dye regeneration which also improves the polymerization extent.
It is worth reminding that the nanometric size region where the effective dose overpasses the threshold one is actually the zone of near-field of colloidal silver nanoparticles where their enhancement factor delivers the required amount of energy, and thus trigger the photopolymerization.

In order to annotate the different behavior observed at the micro and the nanoscale, a simple calculation has to be driven to quantify the quantity of molecules involved at the nanoscale.
Taking into account that the typical dye concentration was 0.5 wt. %, and assuming a homogeneous distribution of the dye within the photopolymer solution, a volume of $10 \times 10 \times 10$ nm^3 contains only four molecules of dye. The same volume contains an average of 200 MDEA molecules and 6000 C=C double bonds. On the basis of these numbers, it appears that the limited reactant is the dye. Thus, it explains why the dye diffusion is so important to provide an efficient polymerization.

Consequently, the extremely limited number of molecules can account for the different comportment observed between the micrometer and the nanometer level: at the microscale, the average number of molecules present in the irradiation volume, of average size $1000 \times 1000 \times 1000$ nm^3, is obviously greater by a factor of 10^6, and thus the need for dye diffusion from outside the irradiated volume is not necessary.
Under these conditions, the limiting process is the number of photons absorbed by the photopolymer and for a given dose, competitive processes such as inhibition by oxygen appears to be relevant.

IN this PhD work, we described an approach for the reliable and comprehensive quantitative characterization of plasmonic near-field structures and for the reputable understanding of the physico-chemical processes that govern the nanofabrication.

Earlier work has considered the interaction between metal structures and photosensitive molecules and has proved that the possibility of triggering a nanoscale photopolymerization, by means of the localized surface plasmons of such nanoparticles, is feasible. It has been also shown that the nanophotopolymerization approach constitutes a powerful technique to image the near-field of metal structures and thus avoids the perturbation of the physics of the sample by bringing a probe close to it. It is worth noticing that the approach of nanoscale photopolymerization relies on the non-linear response of the photosensitive formulation.

During this dissertation, we have attempted to be much more quantitative compared to previous works in the area of near-field imaging.
By irradiating the metal nanoparticles at their resonance, we were capable to nano-mold the dipolar profile of the confined electromagnetic distribution by a photo-activated polymer, with a resolution better than 10 nm. Then and by a precise characterization of the polymer molds using AFM, we were capable to extract precise values for the enhancement factor and the depth of the near-field of silver colloidal nanoparticles, which were in striking agreement with electrodynamic simulations. Moreover, we showed our ability to measure the spectral signature of the localized surface plasmon resonance of a single metal nanoparticle directly in the near-field.
These results demonstrated a quantitative characterization, down to the nanometer level, of the confined evanescent optical fields that are prerequisite for developing photonic applications.

Additionally, we applied our near-field photopolymerization on gold nanorods embedded in a photopolymerizable solution. Again, and by illuminating gold particles off their resonance, we were able to directly embody the profile of the non-resonant field held on the metal/dielectric interface. As a matter of fact, we proved that the sensitivity of the photopolymer is high enough to imprint the non-resonant field of the boundaries, thus allowing a direct visualization, with a nanoscale resolution (2 nm), of the surface charge density distribution governed by vectorial boundaries condition at metal/dieclectric interface. We have shown that, in the case of non-resonant illumination of metal structures, the local field enhancement stems from the surface charges created by the electric field disconti-

nuity at the metal/dielectric interface. These results constitute the first evidence that the polymer elongation is directly related to surface charges created on the gold nanorods through gold susceptibility and permittivity.

Our near-field approach also gave us the opportunity to highlight some phenomena available only at the nanometric scale, namely the dye diffusion and the dye regenration. Verily and by observing the spatial extent of the polymerization reaction under different illumination conditions, it was possible to explore the physico-chemical processes that govern the nanofabrication.

We believe our work is of general interest to the nanoscience community, especially to readers in the fields of plasmonics, near-field optics, nanophotonics, and molecular photochemistry. There is great potential for future researchers to use the fundamental guidelines developed in this thesis in order to design and optimize hybrid nanosystems.

Several perspectives emanate from the present work and aim to understand the material at the nanoscale level.
In fact, we recently started to utilize complex shapes metal nanoparticles, namely nanotriangles, to enhance photopolymerization at their apexes. This will enable us to study the lightning rod effect which arises from geometrical singularities or near any sharp protrusion on a metallic surface, where the electric field reaches high intensity values. Moreover, by creating this polymer dot at one of the triangle apexes, its symmetry will be broken and hence we can investigate non-linear properties of the new hybrid system.

We also initiated work on varying the refractive index of the photopolymerizable formulation by doping it with luminescent materials, such as chromophores, semiconductor quantum dots, metal nanoparticles, liquid crystal molecules, etc. This experiment will finally engender two polymer wings, directed along the incident polarization, where active molecules are imprisoned in them. In point of fact, it would be interesting to conduct a study on the coupling between metal nanoparticles and wrapped molecules in the polymer matrix, by means of conventional or ultrafast spectroscopic techniques.

Additionally, we can study plasmonic propagation using our near-field photopolymerization approach. By making a chain of metal nanorods and illuminating one end of this linear array, we will generate surface plasmons propagative

waves that will trigger the chemical process and hence embody the profile of this wave. then and by precise characterization of the polymer mold, we can determine important parameters related to the propagation of delocalized surface plasmons.

Furthermore, we can take advantage of our nanoscale approach to study the effect of the distance, between metal nanoparticles and molecules bounded to polymer wings, on the Raman signal of the molecule. Minutely, we apply our nanophotopolymerization technique to constitute differently elongated polymer lobes on different samples. Then by functionalizing the polymer part and adding molecules to the sample, we will be capable to adjust the molecule/metal particle distance by just varying the elongation of the polymer lobes around the metal nanosources. This will be a powerful distance control technique that will enable us to study the variation of fluorescence signal of a molecule when its distance from a metal nanoantenna varies.

Bibliography

[1] P. B. Johnson and R. W. Christy. Optical constants of the noble metals. *Phys. Rev. B.*, 6:4370–4379, 1972.

[2] S. A. Maier. *Plasmonics: Fundamental and Applications*. Springer, 2007.

[3] L. M. Liz-Marzan. Nanometals formation and color. *Materials Today*, 7:26–31, 2004.

[4] S. Link and M. A. El-Sayed. Shape and size dependence of radiative, non-radiative and photothermal properties of gold nanocrystals. *Inter. Rev. in Phys. Chem.*, 19:409–453, 2000.

[5] S. Link and M. A. El-Sayed. Optical properties and ultrafast dynamics of metallic nanocrystals. *Annu. Rev. Phys. Chem.*, 54:331–336, 2003.

[6] A. V. Zayats and I. I. Smolyaninov. Near-field photonics: surface plasmon polaritons and localized surface plasmons. *J. Opt. A: Pure Appl. Opt.*, 5:16–50, 2003.

[7] F. Raimondi, G. G. Scherer, R. Kötz, and A. Wokaun. Nanoparticles in energy technology: Examples from electrochemistry and catalysis. *Angew. Chem. Int. Ed.*, 44:2190–2209, 2005.

[8] M. L. Juan, R. Gordon, Y. Pang, F. Eftekhari, and R. Quidant. Self-induced back-action optical trapping of dielectric nanoparticles. *Nature*, 5:915–919, 2009.

[9] M. A. Noginov, G. Zhu, A. M. Belgrave, R. Bakker, V. M. Shalaev, E. E. Narimanov, S. Stout, E. Herz, T. Suteewong, and U. Wiesneret. Demonstration of a spaser-based nanolaser. *Nature*, 460:1110–1112, 2009.

[10] J. N. Anker, W. P. Hall, O. Lyandres, N. C. Shah, J. Zhao, and R. P. Van Duyne. Biosensing with plasmonic nanosensors. *Nature Mat.*, 7:442–453, 2008.

[11] W. Srituravanich, L. Pan, Y. Wang, C. Sun, D. B. Bogy, and X. Zhang. Flying plasmonic lens in the near field for high-speed nanolithography. *Nature Nanotech.*, 3:733–737, 2008.

[12] *Plasmon Printing - A New Approach to Near-Field Lithography*, volume 705. Kik, P. G. and Maier, S. A. and Atwater, H. A., 2002.

[13] H. Wang, Y. Wu, B. Lassiter, C. L. Nehl, J. H. Hafner, P. Nordlander, and N. J. Halas. Symmetry breaking in individual plasmonic nanoparticles. *PNAS*, 103:10856–10860, 2006.

[14] J. Berthelot, A. Bouhelier, J. Huang, C. Margueritat, G. Colas-des Francs, E. Finot, J. Weeber, A. Dereux, S. Kostcheev, H. I. E. Ahrach, A. Baudrion, J. Plain, R. Bachelot, P. Royer, and G. P. Weiderrecht. Tuning of an optical dimer nanoantenna by electrically controlling its load impedance. *Nano Lett.*, 9(11):3914–3921, 2009.

[15] C. Hägglund, M. Zäch, and Bengt Kasemo. Enhanced charge carrier generation in dye sensitized solar cells by nanoparticle plasmons. *Appl. Phys. Lett.*, 92:013113, 2008.

[16] Y. Chen, K. Munechika, and D. S. Ginger. Dependence of fluorescence intensity on the spectral overlap between fluorophores and plasmon resonant single silver nanoparticles. *Nanolett.*, 7:690–696, 2007.

[17] Y. Fedutik, V. V. Temnov, O. Schöps, U. Woggon, and M. V. Artemyev. Exciton-plasmon-photon conversion in plasmonic nanostructures. *Phys. Rev. Lett.*, 99:136802, 2007.

[18] P. Viste, J. Plain, R. Jaffiol, A. Vial, P. M. Adam, and P. Royer. Enhancement and quenching regimes in metal-semiconductor hybrid optical nanosources. *ACS Nano*, 4(2):759–764, 2010.

[19] C. Deeb, R. Bachelot, J. Plain, A. L. Baudrion, S. Jradi, A. Bouhelier, O. Soppera, P. K. Jain, L. Huang, C. Ecoffet, L. Balan, and P. Royer. Quantitative analysis of localized surface plasmons based on molecular probing. *ACS Nano*, 4(8):4579–4586, 2010.

[20] H. Ibn El Ahrach, R. Bachelot, A. Vial, G. Lérondel, J. Plain, and P. Royer. Spectral degeneracy breaking of the plasmon resonance of single metal

nanoparticles by nanoscale near-field photopolymerization. *Phys. Rev. Lett.*, 98:107402, 2007.

[21] C. F. Bohren and D. R. Huffman. *Absorption and Scattering of Light by Small Particles*. Wiley: New York, 1983.

[22] K. L. Kelly, E. Coronado, L. L. Zhao, and G. C. Schatz. The optical properties of metal nanoparticles: The influence of size, shape, and dielectric environment. *J. Phys. Chem. B*, 107:668–677, 2003.

[23] U. Kreibig and M. Vollmer. *Optical Properties of Metal Clusters*. Springer, 1995.

[24] K. S. Lee and M. A. El-Sayed. Gold and silver nanoparticles in sensing and imaging: Sensitivity of plasmon response to size, shape, and metal composition. *J. Phys. Chem. B.*, 110:19220–19225, 2006.

[25] L. Stephan and M. A. El-Sayed. Spectral properties and relaxation dynamics of surface plasmon electronic oscillations in gold and silver nanodots and nanorods. *J. Phys. Chem. B.*, 103:8410–8426, 1999.

[26] G. T. Boyd, Z. H. Yu, and Y. R. Shen. Photoinduced luminescence from the noble metals and its enhancement on roughened surfaces. *Phys. Rev. B*, 33:7923–7936, 1986.

[27] K. L. Kelly, E. Coronado, L. L. Zhao, and G. C. Schatz. Surface enhanced raman spectroscopy using shaped gold nanoparticles. *J. Phys. Chem. B*, 107:668, 2003.

[28] T. Yamaguchi, S. Yoshida, and A. Kinbara. Effect of retarded dipole-dipole interactions between island particles on the optical plasma-resonance absorption of a silver-island film. *Journal of the Opt. Soc. Of America*, 64:1563–1568, 1974.

[29] Y. Yu, S. Chang, C. Lee, and C. R. C. wang. Gold nanorods: Electrochemical synthesis and optical properties. *J. Phys. Chem. B*, 101:6661–6664, 1997.

[30] P. K. Jain, S. Eustis, and M. A. El-Sayed. Plasmon coupling in nanorod assemblies: Optical absorption, discrete dipole approximation simulation, and exciton-coupling model. *J. Phys. Chem. B*, 110:18243–18253, 2006.

[31] P. Alivisatos. The use of nanocrystals in biological detection. *Nature Biotech.*, 22:47–52, 2004.

[32] J. B. Jackson, S. L. Westcott, L. R. Hirsch, J. L. West, and N. J. Halas. Controlling the surface enhanced raman effect via the nanoshell geometry. *Appl. Phys. Lett.*, 82:257–259, 2003.

[33] L. R. Hirsch, J. B. Jackson, A. Lee, N. J. Halas, and J. L. West. A whole blood immunoassay using gold nanoshells. *Anal. Chem.*, 75:2377–2381, 2003.

[34] I. H. El-Sayed, X. Huang, and M. A. El-Sayed. Surface plasmon resonance scattering and absorption of anti-egfr antibody conjugated gold nanoparticles in cancer diagnostics: Applications in oral cancer. *Nano Lett.*, 5:829–834, 2005.

[35] Prashant K. Jain. *Plasmons in Assembled metal nanostructures: Radiative and nonradiative properties, near-field couplin and its Universal Scaling Behaviour*. PhD thesis, School of Chemistry and Biochemistry, Georgia Institute of Technology, 2008.

[36] G. V. Hartland. Measurements of the material properties of metal nanoparticles by time-resolved spectroscopy. *Phys. Chem. Chem. Phys.*, 6:5263–5274, 2004.

[37] S. K. Eaha, H. M. Jaegera, N. F. Scherera, X. M. Linb, and G. P. Wiederrecht. Femtosecond transient absorption dynamics of close-packed gold nanocrystal monolayer arrays. *Chem. Phy. Lett.*, 386:390–395, 2004.

[38] M. Perner, T. Klar, S. Grosse, U. Lemmer, G. Von Plessen, W. Spirkl, and J. Feldmann. Homogeneous line widths of surface plasmons in gold nanoparticles measured by femtosecond pump-and-probe and near-field optical spectroscopy. *Jour. of Lumin.*, 76 and 77:181–184, 1998.

[39] M. Scharte, R. Porath, T. Ohms, M. Aeschlimann, J. R. Krenn, H. Ditlbacher, F. R. Aussenegg, and A. Liebsch. Do mie plasmons have a longer lifetime on resonance than off resonance. *App. Phy. B.*, 73:305–310, 2001.

[40] C. Voisin, D. Christofilos, P. A. Loukakos, N. Del Fatti, F. Vallee, J. Lerme, M. Gaudry, E. Cottancin, M. Pellarin, and M. Broyer. Measurements of the material properties of metal nanoparticles by time-resolved spectroscopy. *Phys. Rev. B*, 69:195416, 2004.

[41] J. H. Hodak, I. Martini, and G. V. Hartland. Spectroscopy and dynamics of nanometer-sized noble metal particles. *J. Phys. Chem. B*, 102:6958–6967, 1998.

[42] C. M. Pitsillides, E. K. Joe, X. Wei, R. R. Anderson, and C.P. Lin. Selective cell targeting with light-absorbing microparticles and nanoparticles. *Biophys Jour.*, 84:4023–4032, 2003.

[43] X. Huang, P. K. Jain, I. H. El-Sayed, and M. A. El-Sayed. Gold nanoparticles: interesting optical properties and recent applications in cancer diagnostics and therapy. *Nanomedicine*, 2:681–693, 2007.

[44] H. Wang, D. W. Brandl, F. Le, P. Nordlander, and N. J. Halas. Nanorice: A hybrid plasmonic nanostructure. *Nano Lett.*, 6:827–832, 2006.

[45] M. W. Knight and N. J. Halas. Nanoshells to nanoeggs to nanocups: optical properties of reduced symmetry core-shell nanoparticles beyond the quasistatic limit. *New J. Phys.*, 10:105006, 2008.

[46] H. Zeng, W. Cai, P. Liu, X. Xu, H. Zhou, C. Klingshirn, and H. Kalt. ZnO-based hollow nanoparticles by selective etching: Elimination and reconstruction of metal-semiconductor interface, improvement of blue emission and photocatalysis. *ACS Nano*, 2(8):1661–1670, 2008.

[47] H. Ibn El Ahrach, R. Bachelot, G. Lérondel, A. Vial, A. S. Grimault, J. Plain, P. Royer, and O. Soppera. Controlling the plasmon resonance of single metal nanoparticles by near-field anisotropic nanoscale photopolymerization. *Journal of Microscopy*, 229:421–427, 2008.

[48] *Nanoscale photo polymerization induced by the enhanced optical near field of metallic nanoparticles*, volume 7395. Deeb, C. and Baudrion, A. L. and Jradi, S. and Plain, J. and Bouhelier, A. and Soppera, O. and Balan, L. and Ridaoui, H. and Royer, R. and Bachelot, R., Proc. SPIE 2009.

[49] J. Plain, Y. Sonnefraud, P. Viste, G. Lérondel, S. Huant, and Royer. Self-assembly drives quantum dot photoluminescence. *Jour. of Fluoresc.*, 19(2):311–316, 2003.

[50] L. Novotny. The history of near-field optics. *Prog. in Opt.*, 50:137–184, 2007.

[51] R. Bachelot, P. Gleyzes, and A. C. Boccara. Reflection-mode scanning near-field optical microscopy using an apertureless metallic tip. *App. Opt.*, 36:2160–2170, 1997.

[52] A. Hartschuh, Xie S. X. Sanchez, E. J., and Novotny Lukas. High-resolution near-field raman microscopy of single-walled carbon nanotubes. *App. Opt.*, 90:095503, 2003.

[53] S. Hudlet, S. Aubert, A. Bruyant, R. Bachelot, P. M. Adam, J. L. Bijeon, G. Lérondel, P. Royer, and A. A. Stashkevich. Apertureless near field optical microscopy: a contribution to the understanding of the signal detected in the presence of a background field. *Opt. Comm.*, 230:245–251, 2004.

[54] C. Hubert, A. Rumyantseva, G. Lérondel, J. Grand, S. Kostcheev, L. Billot, A. Vial, R. Bachelot, and P. Royer. Near-field photochemical imaging of noble metal nanostructures. *Nano Lett.*, 5:615–619, 2005.

[55] Mathieu Juan. *Contribution expérimentale et théorique à l'étude multi-échelle des mouvements moléculaires photo-induits dans les systèmes azoïques*. PhD thesis, Laboratoire de Nanotechnologie et d'Instrumentation Optique, Université de Technologie de Troyes, 2008.

[56] L. Douillard, F. Charra, C. Fiorini, P. M. Adam, R. Bachelot, S. Kostcheev, G. Lérondel, M. L. de la Chapelle, and P. Royer. Optical properties of metal nanoparticles as probed by photoemission electron microscopy. *J. of Appl. Phys.*, 101:83518–83522, 2007.

[57] L. Douillard, F. Charra, Z. Korczak, R. Bachelot, S. Kostcheev, G. Lérondel, P. M. Adam, and P. Royer. Short range plasmon resonators probed by photoemission electron microscopy. *Nano Lett.*, 8:935–940, 2008.

[58] R. F. Egerton. Electron energy-loss spectroscopy in the TEM. *Rep. Prog. Phys.*, 72:016502, 2009.

[59] A. Bouhelier. Field-enhanced scanning near-field optical microscopy. *Microsc. Res. and Tech.*, 69:563–579, 2006.

[60] J. P. Kottmann, O. J. F. Martin, D. R. Smith, and S. Schultz. Non-regularly shaped plasmon resonant nanoparticle as localized light source for near-field microscopy. *Jour. of Microsc.*, 202:60–65, 2001.

[61] H. Fischer and O. J. F. Martin. Engineering the optical response of plasmonic nanoantennas. *Opt. Exp.*, 16(12):9144–9154, 2008.

[62] K. H. Su, Q. H. Wei, X. Zhang, J. J. Mock, D. R. Smith, and S. Schultz. Interparticle coupling effects on plasmon resonances of nanogold particles. *Nano. Lett.*, 3(8):1087–1090, 2003.

[63] R. Shenhar and V. M. Rotello. Nanoparticles: Scaffolds and building blocks. *Acc. Chem. Res.*, 36:549–561, 2003.

[64] BB International, Copyright 2009 BBI Online - Registered in England and Wales 2075749 VAT no.762455421.

[65] J. Grand, P. M. Adam, A. S. Grimault, A. Vial, M. L. De la Chapelle, J. L. Bijeon, S. Kostcheev, and P. Royer. Optical extinction spectroscopy of oblate, prolate and ellipsoid shaped gold nanoparticles: Experiments and theory. *Plasmonics*, 1:135–140, 2006.

[66] Johan Grand. *Plasmons de surface de nanoparticules : spectroscopie d'extinction en champs proche et lointain, diffusion Raman exaltée.* PhD thesis, Laboratoire de Nanotechnologie et d'Instrumentation Optique, Université de Technologie de Troyes, 2004.

[67] Pierre Viste. *Etude expérimentale des interactions entre luminophores et nanoparticules métalliques.* PhD thesis, Laboratoire de Nanotechnologie et d'Instrumentation Optique, Université de Technologie de Troyes, 2007.

[68] J. Plain, A. Pallandre, B. Nysten, and M. Jonas A. Nanotemplated crystallization of organic molecules. *Small*, 2(7):892–897, 2006.

[69] J. Grand, S. Kostcheev, J. L. Bijeon, M. Lamy de la Chapelle, P. M. Adam, A. Rumyantseva, G. Lérondel, and P. Royer. Optimization of sers-active substrates for near-field raman spectroscopy. *Synt. Met.*, 139:621–624, 2003.

[70] A. Bouhelier, R. Bachelot, J. S. Im, G. P. Wiederrecht, G. Lérondel, S. Kostcheev, and P. Royer. Electromagnetic interactions in plasmonic nanoparticle arrays. *J. Phys. Chem. B*, 109:3195–3198, 2005.

[71] S. Link and A. El-Sayed, M. Size and temperature dependence of the plasmon absorption of colloidal gold nanoparticles. *J. Phys. Chem. B.*, 103:4212–4217, 1999.

[72] A. Espanet, C. Ecoffet, and J. Lougnot, D. Photopolymerization by evanescent waves. ii: revealing dramatic inhibiting effects of oxygen at the submicrometer scale. *J. Polym. Sci. A: Polym. Chem.*, 3:2075–2085, 1999.

[73] C. Ecoffet, A. Espanet, and J. Lougnot, D. Photopolymerization by evanescent waves: A new method to obtain nanoparts. *Adv. Mater.*, 10:411–414, 1998.

[74] R. Bachelot, F. Abdesslame, R. Fikri, D. Barchiesi, G. Lérondel, and P. Royer. Coupling semiconductor lasers into single-mode optical fibers by use of tips grown by photopolymerization. *Opt. Lett.*, 29:1971–1973, 2004.

[75] A. Espanet, G. Dos Santos, C. Ecoffet, and J. Lougnot, D. Photopolymerization by evanescent waves: characterization of photopolymerizable formulation for photolithography with nanometric resolution. *Appl. Surf. Sci.*, 138:87–92, 1999.

[76] R. Bachelot, C. Ecoffet, D. Deloeil, P. Royer, and Lougnot D. J. Integration of micrometer-sized polymer elements at the end of optical fibers by free-radical photopolymerization. *Appl. Opt.*, 40:5860–5871, 2001.

[77] *Photopolymerization Induced Materialization of the Dipolar Response from Isolated Metallic Nanoparticles*, volume 5458. Wurtz, G. and Burget, D. and Carré, C., Proc. SPIE 2004.

[78] J. P. Fouassier. *Photoinitiation, photopolymerization and photocuring*. Hanser Publisher, 1995.

[79] P. Judeinstein and C. Sanchez. Hybrid organic-inorganic materials: A land of multidisciplinarity. *J. Mater. Chem.*, 6:511–525, 1996.

[80] C. Croutxe-Barghorn, O. Soppera, and M. Chevallier. Diffraction gratings in hybrid sol-gel films: On the understanding of the relief generation process. *Macromolec. Mat. and eng.*, 288(3):219–227, 2003.

[81] O. Soppera, C. Croutxe-Barghorn, and J. Lougnot, D. New insights into photoinduced processes in hybrid sol-gel glasses containing modified titanium alkoxides. *New J. of Chem.*, 25(8):1006–1014, 2001.

[82] B. Deutsch, R. Hillenbrand, and L. Novotny. Visualizing the optical interaction tensor of a gold nanoparticle pair. *Nano Lett.*, 10:652–656, 2010.

[83] J. A. Schuller, E. S. Barnard, W. Cai, Y. C. Jun, J. S. White, and M. L. Brongersma. Plasmonics for extreme light concentration and manipulation. *Nat. Mat.*, 9:193–204, 2010.

[84] W. L. Barnes, A. Dereux, and T. W. Ebbesen. Surface plasmon subwavelength optics. *Nature*, 424:824–830, 2003.

[85] H. A. Atwater and A. Polman. Plasmonics for improved photovoltaic devices. *Nat. Mat.*, 9:205–213, 2010.

[86] P. V. Kamat and G. C. Schatz. Nanotechnology for next generation solar cells. *J. Phys. Chem. C*, 113:15473, 2009.

[87] J. Cole and N. J. Halas. Optimized distributions of tunable plasmonic nanoparticles for solar light harvesting applications. *Appl. Phys. Lett.*, 89:153120, 2006.

[88] D. J. Bergman and M. I. Stockman. Surface plasmon amplification by stimulated emission of radiation: Quantum generation of coherent surface plasmons in nanosystems. *Phys. Rev. Lett.*, 90:027402, 2003.

[89] H. Eghlidi, K. G. Lee, X. W. Chen, S. Gotzinger, and V. Sandoghdar. Resolution and enhancement in nanoantenna-based fluorescence microscopy. *Nano Lett.*, 9:4007–4011, 2009.

[90] G. Baffou, R. Quidant, and F. J. Garcia de Abajo. Nanoscale control of optical heating in complex plasmonic systems. *ACS Nano*, 4:709–716, 2010.

[91] J. R. Cole, N. A. Mirin, M. W. Knight, G. P. Goodrich, and N. J. Halas. Photothermal efficiencies of nanoshells and nanorods for clinical therapeutic applications. *J. Phys. Chem. C*, 113:12090–12094, 2009.

[92] A. W. Haes, W. P. Hall, L. Chang, W. L. Klein, and R. P. Van Duyne. A localized surface plasmon resonance biosensor: First steps toward an assay for alzheimer's disease. *Nano Lett.*, 4:1029–1034, 2004.

[93] G. P. Wiederrecht. Near-field optical imaging of noble metal nanoparticles. *Eur. Phys. J. Appl. Phys.*, 28:3–18, 2004.

[94] J. Nelayah, M. Kociak, O. Stephan, F. J. Garcia de Abajo, M. Tence, L. Henrard, D. Taverna, I. Pastoriza-Santos, Liz-Marzan L. M., and C. Colliex. Mapping surface plasmons on a single metal nanoparticle. *Nat. Phys.*, 3:348–353, 2008.

[95] U. Hohenester, H. Ditlbacher, and J. R. Krenn. Electron-energy-loss spectra of plasmonic nanoparticles. *Phys. Rev. Lett.*, 103:106801, 2009.

[96] C. Deeb, L. Huang, A. Plain, J. Bouhelier, O. Soppera, R. Bachelot, and P. Royer. Nanophotopolymerization triggered by the enhanced optical near-field of metallic nanoparticles. *Leb. Sci. J. (ISSN 1561-3410)*, 11(2), 2010.

[97] G. Wurtz, R. Bachelot, F. H'Dhili, P. Royer, C. Triger, C. Ecoffet, and D. J. Lougnot. Photopolymerization induced by optical field enhancement in the vicinity of a conducting tip under laser illumination. *Jpn. J. Appl. Phys.*, 39:98–100, 2000.

[98] W. Srituravanich, N. Fang, C. Sun, Q. Luo, and X. Zhang. Plasmonic nanolithography. *Nano Lett.*, 4(6):1085–1088, 2004.

[99] A. Sundaramurthy, P. J. Schuck, N. R. Conley, D. P. Fromm, G. S. Kino, and W. E. Moerner. Toward nanometer-scale optical photolithography: Utilizing the near-field of bowtie optical nanoantennas. *Nano Lett.*, 6(3):355–360, 2006.

[100] K. Ueno, S. Takabatake, Y. Nishijima, V. Mizeikis, Y. Yokota, and H. Misawa. Nanogap-assisted surface plasmon nanolithography. *J. Phys. Chem. Lett.*, 1(3):657–662, 2010.

[101] S. J. Orfanidis. *Electromagnetic waves and antennas.* http://www.ece.rutgers.edu/ orfanidi/ewa/, 2008.

[102] J. W. Goodman. *Introduction to Fourier Optics.* McGraw - Hill Science, 1996.

[103] P. K. Jain, W. Huang, and A. El-Sayed, M. On the universal scaling behavior of the distance decay of plasmon coupling in metal nanoparticle pairs: A plasmon ruler equation. *Nano Lett.*, 7(7):2080–2088, 2007.

[104] S. Aubert, A. Bruyant, S. Blaize, R. Bachelot, G. Lerondel, S. Hudlet, and P. Royer. Analysis of the interferometric effect of the background light in apertureless scanning near-field optical microscopy. *J. Opt. Soc. Am. B: Opt. Phys.*, 20:2117–2124, 2003.

[105] V. Sandoghdar and J. Mlynek. Prospects in apertureless snom with active probes. *J. Opt. A: Pure Appl. Opt.*, 1:523–530, 1999.

[106] E. D. Palik. *Handbook of Optical Constants of Solids.* Academic Press, Orlando, FL, 1985.

[107] C. Deeb, X. Zhou, D. Gérard, A. Bouhelier, P. K. Jain, J. Plain, O. Soppera, P. Royer, and R. Bachelot. Off-resonant optical excitation of gold nanorods: Nanoscale imprint of polarization surface charge distribution. *J. Chem. Phys. Lett.*, 2(1):7–11, 2011.

[108] J. I. Gersten. The effect of surface roughness on surface enhanced raman scattering. *J. Chem. Phys.*, 72:5779, 1980.

[109] M. B. Mohamed, V. Volkov, S. Link, and M. A El-Sayed. The lightning gold nanorods: Fluorescence enhancement of over a million compared to the gold metal. *J. Chem. Phys. Lett.*, 317:517–523, 2000.

[110] R. Bachelot, F. H'dhili, D. Barchiesi, G. Lerondel, R. Fikri, P. Royer, N. Landraud, J. Peretti, F. Chaput, G. Lampel, J. P. Boilot, and K. Lahlil. Apertureless near-field optical microscopy: A study of the local tip field enhancement using photosensitive azobenzene-containing films. *J. Appl. Phys.*, 94:2060, 2003.

[111] J. Van Bladel. *Singular Electromagnetic Fields and Sources.* IEEE, Ox-ford, 1995.

[112] B. Lamprecht, J. R. Krenn, A. Leitner, and F. R. Aussenegg. Resonant and off-resonant light-driven plasmons in metal nanoparticles studied by femtosecond-resolution third-harmonic generation. *Phys. Rev. Lett.*, 83(21):4421, 1999.

[113] A. O. Govorov and H. H. Richardson. Generating heat with metal nanoparticles. *Nano Today*, 2:30–38, 2007.

[114] O. Soppera, S. Jradi, and J. Lougnot, D. Photopolymerization with microscale resolution: Influence of the physico-chemical and photonic parameters. *J. Polym. Sci. A: Polym. Chem.*, 46:3783–3794, 2008.

Chapter Six

FRENCH SUMMARY: Propriétés Optiques de Nanostructures Métalliques sondées par des molécules photosensibles

6.1 Introduction - Objectifs de la thèse

Un nouveau concept de particules hybrides métal/polymère a été introduit par le LNIO (ICD, CNRS 2848, UTT) depuis quelques années. Celles-ci sont fabriquées par photopolymérisation locale à proximité de nanoparticules métalliques (NPM). Le champ proche exalté associé aux plasmons de surface localisés amorce la photopolymérisation. L'environnement polymère ainsi fabriqué autour de la particule dépend de la nature du champ proche initial. En particulier, l'environnement diélectrique de la particule peut être modifié de façon anisotrope, changeant ainsi le degré de symétrie du milieu à l'échelle moléculaire. Les propriétés des particules métalliques sont ainsi modifiées de façon contrôlée [20, 47, 19]. Par exemple, de nouveaux niveaux d'énergie dans la résonance plasmon peuvent apparaître, par levée de dégénérescence spectrale.

Depuis une dizaine d'années, les propriétés physiques (optiques, thermiques, etc.) des nanoparticules métalliques suscitent un intérêt croissant aussi bien dans les communautés de physiciens que celles de chimistes et biologistes. Ces propriétés sont variées, riches et complexes. Elles sont principalement régies par les oscillations collectives des électrons de conductions appelées "plasmon".

Différents types d'effets physiques, liés aux nanoparticules métalliques ont été étudiés et exploités.
Le premier effet, non résonnant, est "l'effet de pointe optique" qui correspond à l'excitation d'une singularité électromagnétique ayant lieu au niveau des faibles rayons de courbure (pointes, nanoobjets, etc.) [111]. Cet effet est associé à l'apparition d'une forte densité de charge et d'une intense nanosource optique confinée en extrémité de la nanostructure.
Le deuxième est un effet résonnant: lorsque les nanoparticules métalliques sont excitées à résonance, elles sont accompagnées premièrement d'une exaltation locale du champ électromagnétique résultant en une nanosource très intense [6, 43, 24, 54, 50] et deuxièmement, d'une augmentation localisée de température [91, 92, 4]. Ces différents effets sont exploités dans de nombreux domaines incluant le SERS [27], les panneaux solaires [86, 15], la microscopie et spectroscopie optique en champ proche [59, 51, 53, 93], les nanocapteurs [10] et la médecine pour le traitement curatif du cancer [43, 34].
Compte tenu des applications potentielles nombreuses, le contrôle et l'optimisation de ces effets représentent un challenge qui restera d'actualité encore pendant de longues années. Ainsi, deux approches ont été développées jusqu'içi. La première consiste à jouer sur la géométrie, et notamment sur la forme des nanostructures, ainsi que sur la distance entre voisins, afin de contrôler les résonances plasmons [70]. Cette approche a largement bénéficié de techniques de fabrication de pointe comme la lithographie électronique. La seconde approche consiste à exploiter l'influence de l'environnement diélectrique sur la résonance de la particule. Par exemple, l'augmentation de l'indice de réfraction de quelques dixièmes induit un décalage vers le rouge de la résonance plasmon de quelques dizaines de nanomètres [24]. Dans ce cadre, des nanoparticules hybrides métal / polymère ou métal / silice ont été ainsi synthétisées dans le but de modifier et contrôler les propriétés des nanoparticules métalliques [20, 44, 45].

Cette thèse est articulée autour de trois objectifs interconnectés: le premier est l'étude du champ proche optique des nanoparticules métalliques. Le second est la compréhension de l'interaction champ proche / matériaux polymères et enfin le dernier est la synthèse et l'étude des nanoparticules hybrides.
De plus, les nouvelles nanoparticules hybrides ainsi crées seront potentiellement intéressantes pour des applications de marquage, d'optoélectronique intégrée ou encore de sources de photons confinées ajustable en longueur d'onde [19, 20].
Ainsi, l'approche proposée dans cette thèse est originale: elle consiste à modifier à l'échelle nanométrique l'environnement physico-chimique de la nanoparticule métallique par des processus photochimiques locaux et anisotropes initiés par le champ proche optique de la particule elle-même.

La première année de la thèse était consacrée au développement et à la caractérisation de nouvelles nanosources photoniques basées sur l'exaltation du champ électromagnétique autour de nanoparticules métalliques. À travers cette partie du travail, nous avons amélioré nos connaissances sur les exaltations locales du champ électromagnétique.

Durant la deuxième année de la thèse, nous avons réussi à introduire un nouveau concept: la synthèse des nanoparticules hybrides en remplaçant les particules lithographiés par des particules colloïdales. Grâce à ce concept, nous avons synthétisé de nouvelles particules hybrides métal (colloïdes)/polymère [19]. Nous avons également fabriqué des matériaux polymères à l'échelle micrométrique [48]. A l'aide des expériences menées durant cette période, nous avons approfondi nos perceptions et compréhensions de l'interaction entre le champ proche des nanoparticules métalliques et les matériaux polymères.

La troisième année de la thèse a été dédiée à des études paramétriques qui avaient comme but de quantifier le champ proche optique de nanoparticules métalliques, notamment le facteur d'exaltation de ce type de structures et la profondeur de pénétration du champ. De plus, un spectre de diffusion en champ proche a été obtenu pour une nanoparticule colloidale unique.
En parallèle, une étude sur des nanorods d'Or a été faite en utilisant notre approche de nanophotopolymérisation en champ proche. En effet, cette technique nous a permis d'imager, avec une résolution nanométrique inédite, le champ électrique résultant des densités de charges surfaciques crées à l'interface métal / polymère. Au cours de cette étude, nous avons montré que juste les composantes du champ électrique normales à la surface et parallèles à la direction du champ incident sont capables de délivrer des intensités de champ non nulles, et donc induire la photopolymérisation.
De plus, notre approache nous a donné la possibilité de regarder les processus physico-chimiques qui gouvernent la photopolymérisation à l'échelle nanométrique. La troisième étude que nous avons faite, a remis en cause les principes valables aux échelles macro et même micro. La raison était le nombre limité des espèces en jeu dans un espace nanoconfiné, notamment quelques molécules de colorant dans la région du champ proche optique autour des nanoparticules.
Toutes ces études ont faits le sujet de publications internationales. Suite à l'incapacité de développer tout dans ce rapport, une partie des résultats sera juste présentée.

6.2 Fabrication et caractérisation de nanoparticules métalliques

Une partie importante de cette thèse a été consacrée à la fabrication et la caractérisation de nanoparticules métalliques (NPM). Plusieurs types de nanoparticules a été utilisées durant ce travail, notamment des particules fabriquées par lithographie électronique (cylindres, rods, etc.) et des particules colloidals synthétisées commercialement.

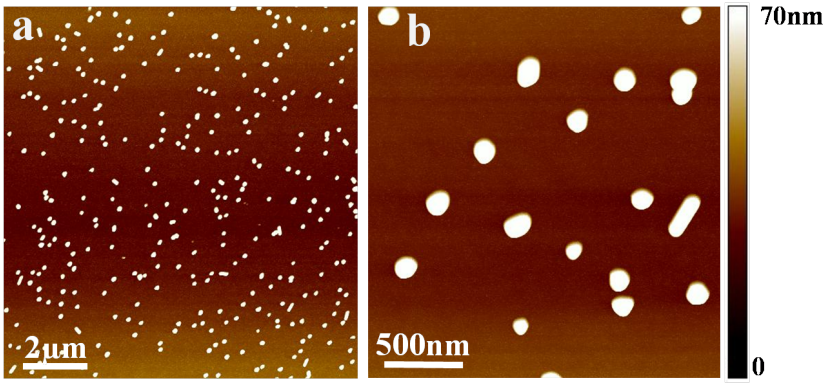

Figure 6.1: Image AFM montrant des colloides d'argent déposées sur un substrat de verre. (a) 10 x 10 μm^2, (b) 2 x 2 μm^2.

A noter que quelque soit le type de nanostructures utilisées durant notre expérience, nous les avons bien caractérisées en utilisant la microscopie à force atomique (AFM), la microscopie électronique à balayage (MEB), la spectroscopie de diffusion et d'extinction. A titre d'exemple, les Figures 6.1 et 6.2 montrent respectivement des images AFM et MEB de nanoparticules colloidales et lithographiées d'argent. Ces images permettant de déterminer le diamètre, la hauteur, et la distance interparticulaire des structures.

Pour des nanoparticules sphériques (de constante diélectrique ε), le maximum d'absorption, d'après l'équation (Eq.) 6.1, est obtenu pour la valeur minimale du terme $\varepsilon_m + 2\varepsilon_d$.

$$p_0 = r^5 \varepsilon_1 \left(\frac{\varepsilon_m - \varepsilon_d}{\varepsilon_m + 2\varepsilon_d}\right) \tag{6.1}$$

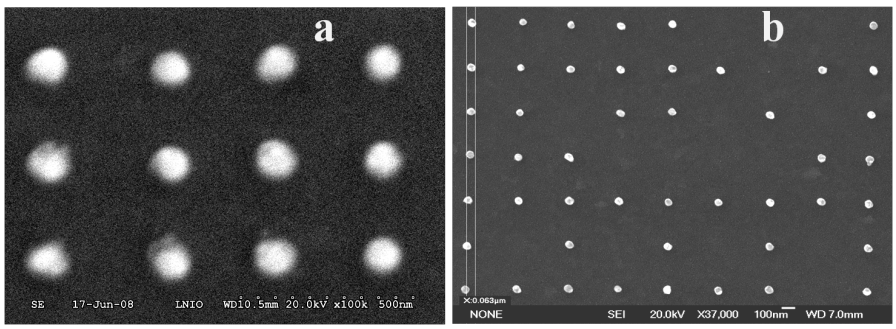

Figure 6.2: Image MEB pour un pattern ordonné de nanoparticules d'argent. (a) Image MEB faite au LNIO. (b) Image MEB faite au "laboratoire Interdisciplinaire Carnot de Bourgogne" à Dijon.

La condition de résonance de plasmon de surface (RPS) est alors: $\varepsilon_m(\omega) = -2\varepsilon_d$ où ε_d est la constante diélectrique du milieu entourant la nanoparticule métallique et ε_m est la partie réelle de la constante diélectrique du métal. La partie réelle de la fonction diélectrique étant monotone pour les valeurs positives, une seule valeur de ω satisfait la condition de résonance. Pour cette raison, une sphère d'argent ne présente qu'un seul mode dipolaire de plasmon de surface. On notera que la position du pic de plasmon est donnée par plusieurs facteurs principaux: la nature du matériau, la fonction diélectrique entourant la particule métallique, les dimensions de la structure métallique et la distance séparant deux NPM voisines.

A titre d'exemple, Figure 6.3 montre des spectres d'extinction de pattern ordonné de nanoparticules d'argent ayant différents diamètres et pour une distance interparticulaire constante, 300 nm. Cette figure confirme que le pic de résonance varie avec la taille de la nanoparticule, shiftant vers le rouge pour des nanostructures plus grandes.

6.3 Développement et caractérisation de nouvelles formulations chimiques

6.3.1 Introduction et Composition

Le système photopolymérisable utilisé dans [20, 48] est développé par nos collaborateurs, à Mulhouse (CNRS UMR 7525) et est composé d'un colorant (Eosine-Y) dont le spectre d'absorption s'étend entre 450 nm et 550 nm, un méthyldiéthanolamine

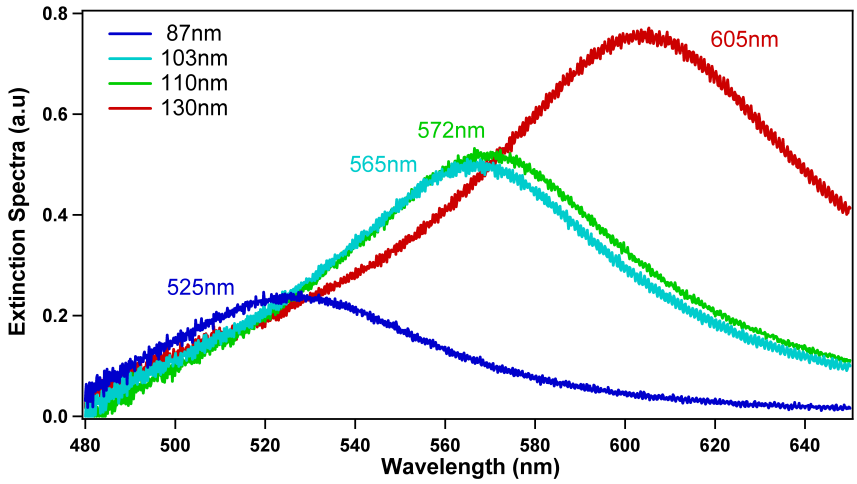

Figure 6.3: Spectres d'extinction de pattern ordonné de naoparticules d'argent ayant différents diamètres, allant de 85 à 130 nm. La distance,bord-à-bord, entre deux particules successives est de 300 nm.

amine MDEA et d'un monomère acrylate multifonctionnel, triacrylate pentaérythritol PETIA. Cette solution a fait l'histoire de plusieurs travaux publiés [73, 77, 72, 75, 114, 76].

Brièvement, l'absorption de la lumière par l'Eosine-Y fait passer le colorant à l'état excité singulier, puis triplet, qui réagit avec l'amine pour former des radicaux. Ces radicaux déclenchent ensuite la polymérisation du monomère. Des réactions faisant intervenir les radicaux sont principalement affectées par de l'oxygène (O_2), conduisant à une période d'inhibition. Au cours de cette période, les photons absorbés par les radicaux réagissent principalement avec O_2 dissous jusqu'à obtenir une concentration suffisamment faible d'O_2 qui permet à la réaction de polymérisation de se déclencher. La quantité d'énergie absorbée par la solution chimique à ce stade est définie comme le seuil d'énergie [77, 72, 114]. Les NPM d'argent ont été utilisées avec ce type de formulation, car un chevauchement entre l'absorption spectrale du colorant et la résonance plasmon de surface des NPM incorporé dans un polymère liquide, peut être atteint.

6.3.2 Caractérisation

Afin d'étudier le photopolymère et de déterminer son énergie seuil, nous l'avons entièrement caractérisé à l'aide du dispositif expérimental décrit dans la section suivante. Le diamètre du faisceau incident était de 2 μm et la longueur d'onde

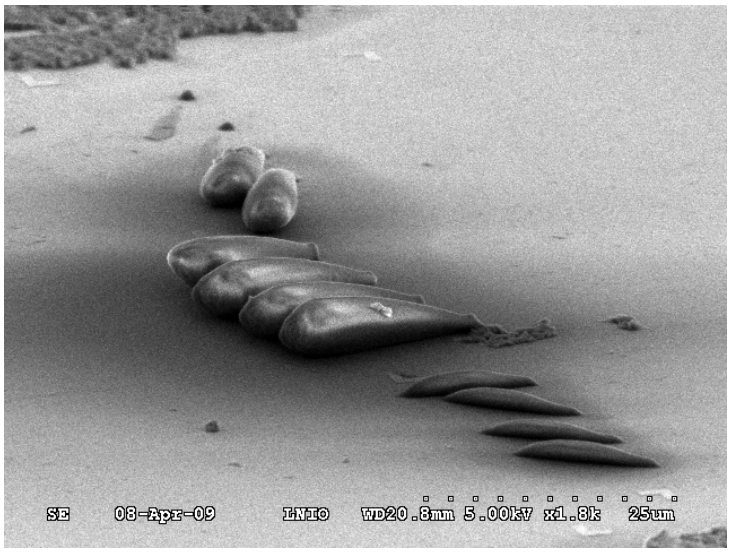

Figure 6.4: Pointes de polymère obtenues sur un substrat de verre pour des valeurs multiples de la puissance incidente pour un temps constant, 1 s. Les deux premières pointes (côté haut gauche) ont été faites avec P = 650 nW. La troisième jusqu'à la sixième pointe ont été fabriquées avec P = 500 nW, et les dernières quatres pointes avec P = 400 nW.

incidente était 514 nm.

Dans la Figure 6.4 (image Scanning Electron Microscope SEM), nous montrons des pointes de polymère obtenues pour des valeurs multiples de la puissance de la lumière verte actinique. Ces pointes sont trop longues pour se tenir debout sur la surface du verre.
Comme on peut le voir sur l'image MEB, la section de la base sur laquelle la pointe polymère repose est faible par rapport à sa hauteur, c'est la raison pour laquelle les pointes n'ont pas pu se tenir debout sur la surface du verre. Il convient de noter que le volume de la goutte est la principale raison pour laquelle la hauteur des pointes de polymère est élevée. Cela avait déjà été remarqué par Bachelot *et al.* dans le cas de l'intégration des éléments de polymère de taille micrométrique à la fin de fibres optiques par photopolymérisation radicalaire [76]. Au cours de leurs expériences, le groupe a montré que même pour les plus courtes expositions, la longueur de la pointe intégrée sur le coeur de la fibre est égale à la hauteur de la goutte. Les deux seules différences entre les expériences déjà faites et celles présentées dans ce document est le profil du champ électrique et le volume de la goutte de formulation qui est millimétrique dans notre cas (c'est pourquoi la hauteur de nos pointes polymère est plus accentuée).

Dans la Figure 6.5 (image SEM), nous illustrons l'influence de la puissance et du temps d'irradiation sur la longueur de la pointe fabriquée: chaque fois que nous augmentons l'énergie du laser, la longueur et même le diamètre de l'extrémité de polymère augmente aussi. Près de l'énergie seuil, nous sommes capables de fabriquer des pointes de polymère capable de résister et de rester en place même après le processus de rinçage.

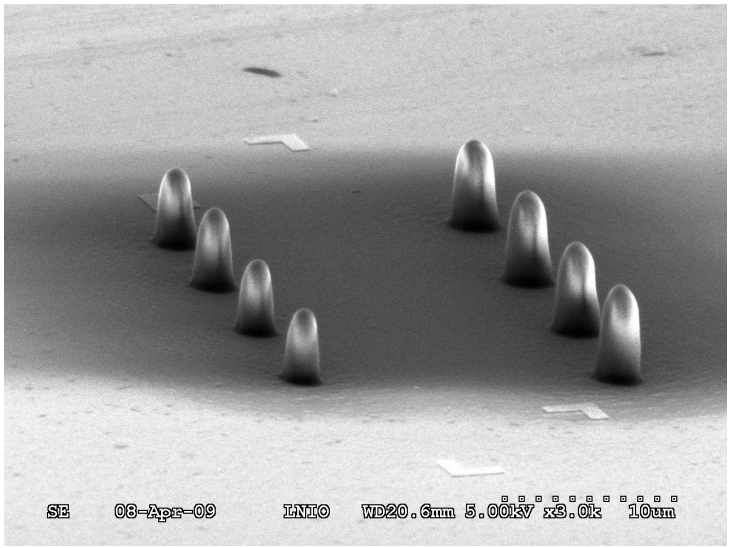

Figure 6.5: Influence de l'énergie du faisceau laser sur la longueur des pointes de polymère au voisinage de l'énergie seuil. La puissance était constante, 300 nW. Le temps était 2 s pour les pointes de droite et 1 s pour celles de gauche.

Trois illuminations ont été faites pour P = 300 nW: 2 s, 1 s et 0.5 s. Comme nous pouvons le remarquer sur la Figure 6.5, les pointes polymères correspondant à t = 0.5 s n'existent pas, ce qui veut dire que que la dose reçue par l'échantillon n'était pas suffisante pour déclencher la photopolymérization, et donc cette dose est en dessous de la dose seuil. De cette façon, nous étions capable de déterminer ce paramètre clé: P = 300 nW pour t = 1 s, ce qui signifie une dose seuil D_{th} de 7500 mJ/cm^2.

Autres formulations photopolymérisables ont été fabriquées et caractérisées durant ce travail de thèse, notamment une solution de sol-gel hybrid et une solution avec l'Eosine-Y comme colorant et une concentration de 5% d'inhibiteur. La procédure utilisée pour ces solutions ne sera pas détaillée içi par manque de place.

6.4 Montage expérimental

Une partie importante de la thèse a été consacrée au développement d'un nouveau montage expérimental avec de nouveaux appareils d'équipements dédiés au projet "Photohybrid". Cette section décrit le montage réalisé qui a été développé à partir d'un microscope optique inversé sur lequel une tête AFM a été installée. Le montage est schématisé par la Figure 6.6.

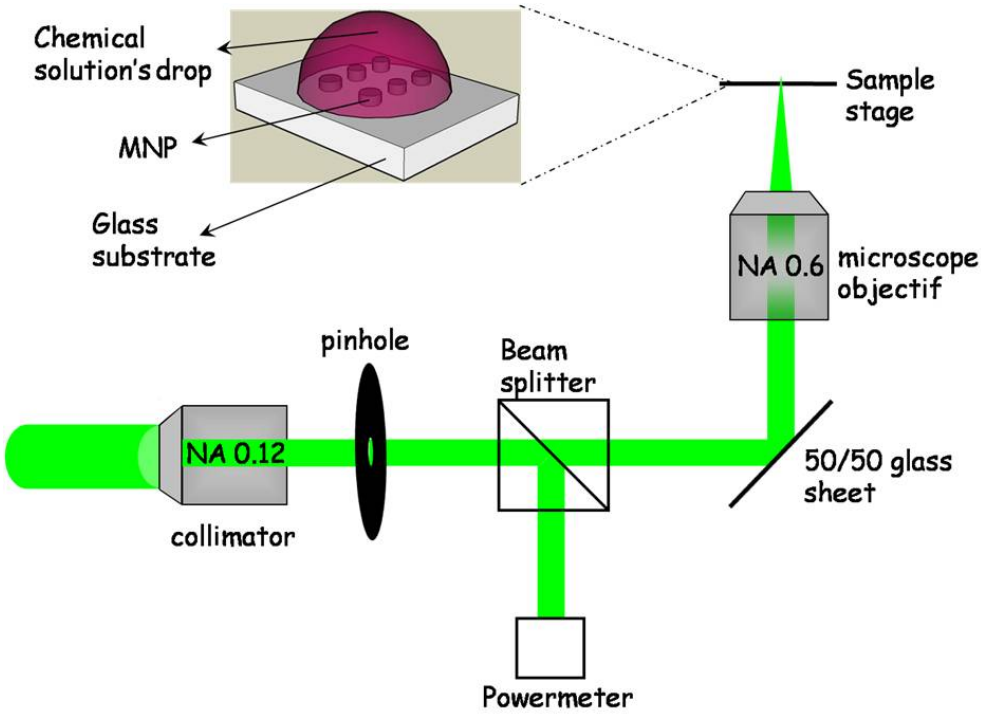

Figure 6.6: Nouveau montage expérimental.

La lumière actinique est fournie par une source laser Argon Krypton (Ar:Kr), ayant des raies allant de 485 nm à 647 nm, couplée dans une fibre optique monomode. Ce couplage garantit, à l'autre bout de la fibre optique, un faisceau filtré et présentant une répartition gaussienne d'intensité. Le faisceau est ensuite étendu spatialement à l'aide d'un objectif ayant 0.12 comme ouverture numérique. La longueur d'onde incidente choisie doit être comprise dans le spectre d'absorption du colorant de la formulation chimique.

Le faisceau est ensuite réfléchi par plusieurs miroirs, passe par un polariseur pour ajuster sa polarisation et est finalement couplé dans un microscope optique inversé Olympus Ix71. La puissance du faisceau laser est suivie en temps réel pour pouvoir détecter la moindre fluctuation. Le diamètre du spot laser peut être modifié entre 300 nm et 8 μm en jouant sur l'ouverture numérique de l'objectif du microscope et sur le diamètre d'un diaphragme placé dans le chemin optique du faisceau, comme nous pouvons le voir sur la Figure 6.6.

Un deuxième chemin optique fournit un faisceau laser homogène, monochromatique et étendu, avec un spot laser de 1-cm de diamètre. Les expositions en présence de nanoparticules métalliques ont été faites à l'aide de ce spot laser pour guarantir que toutes les particules sont irradiées avec une puissance homogène.

Nous avons aussi couplé un laser He-Ne, ayant 633nm comme longueur d'onde, dans le chemin optique du faisceau laser actinique et nous les avons exactement alignés. Ceci nous a servi comme guide afin de détecter la position exacte du faisceau Ar:Kr, même en présence de la formulation photosensible.
Le porte-objet initial du microscope optique a été remplacé par une platine motorisée d'un microscope à force atomique (AFM) Veeco Bioscope II. Ce dernier microscope est aussi couplé avec le microscope optique inversé et peut être contrôlé à l'aide d'un contrôleur Nanoscope V. La longueur d'onde du faisceau laser de l'AFM Veeco est de 805 nm ce qui évite toute influence sur l'absorption du colorant.

En utilisant ce nouveau montage, nous sommes capables de faire une exposition pour un ensemble de NPM, de déplacer la platine motorisée Veeco afin de changer la position du spot laser, et de faire une autre exposition en changeant les paramètres d'irradiation (puissance, temps d'irradiation, etc.). En utilisant un objectif de microscope approprié et avec un espacement suffisant entre les NPM, la possibilité d'irradier une particule métallique unique est largement envisageable.

6.5 Exposition en présence des structures métalliques - Etude quantitative du champ proche des NPM.

La formulation caractérisée au cours de la section 3 a été utilisée pour étudier son interaction avec le champ proche optique des NPM. Ces particules couvertes par la formulation photosensible sont illuminées avec une densité d'énergie inci-

dente plus petite que le seuil de polymérisation. En respectant ces paramètres, le champ proche optique généré par les NPM est utilisé comme source d'énergie pour induire une photopolymérisation locale, permettant ainsi la photosynthèse de nouveaux nanoobjets hybrides métal / polymère.

Nous avons utilisé deux types de NPM: les particules lithographiées déjà utilisées dans [20] et les particules colloïdales. Les études paramétriques menées sur ces colloides d'argent irradiées à leur résonance ont aboutient à une publication dans la revue ACS Nano [19]. En plus, deux autres études ont été menées: la première concerne l'étude de nanorods d'Or irradiés hors leur résonance afin de caractériser le champ électrique non-résonant existant à l'interface métal / polymère, et la deuxième étude concerne les processus physico-chimiques qui contrôllent la fabrication du polymère à l'échelle nanométrique. Ces deux études ont fait le sujet de deux revues supplémentaires.
La fabrication et la caractérisation des particules lithographiées et colloidales a été détaillée dans la section 2. En plus, la caractérisation du système photosensible a été faite dans la section 3, afin de déterminer sa dose seuil.

6.5.1 Particules lithographiées

La figure 6.7 montre une image AFM, panel (a), d'un ensemble de NPM irradiées avec une dose légèrement inférieure à la dose seuil. La lumière incidente est polarisée dans le sens de la flèche blanche indiquée sur l'image AFM (b). L'image AFM en (a) présente une pointe polymère micrométrique de diamètre environ 500 nm, qui correspond évidemment à une dose locale supérieure à la dose seuil. Le faisceau laser qui a été utilisé durant cette expérience avait un profil gaussien et un diamètre de 6 μm. Ceci signifie que seul le sommet de la gaussienne, ayant 500 nm comme taille, a dépassé la dose seuil d'où la pointe polymère micrométrique, mais le reste de la gaussienne, éclairant les NPM, avait une dose inférieure à la dose seuil.

Ce qui est le plus intéressant est de regarder les NPM qui entourent cette pointe de polymère. Ces NPM ont été irradiées avec une dose inférieure à la dose seuil mais suffisante pour faire résonner leurs plasmons de surfaces. En observant ces particules de plus près(cf. panel (b) de la Figure 6.7), nous pouvons remarquer le champ proche optique des NPM qui a été imprimé par la solution photopolymérisable le long de la direction y de la polarisation de la lumière incidente. Cette conclusion est bien confirmée par les sections faites le long des directions y et x

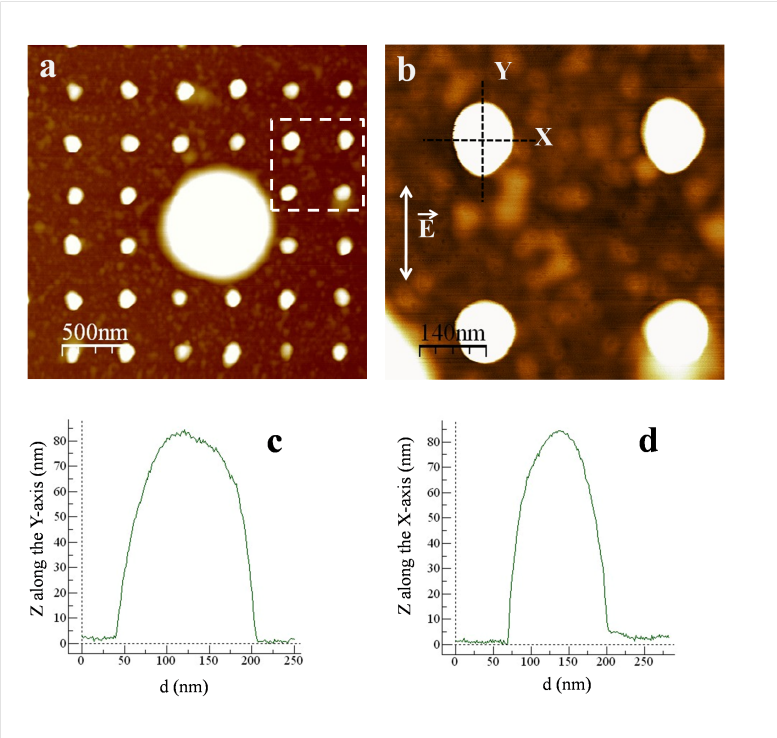

Figure 6.7: Photopolymérisation par le champ proche optique de nanoparticules lithographiées. (a) Image AFM montrant un ensemble de NPM irradiées avec une pointe polymère micrométrique. (b) Image AFM montrant un zoom sur quelques particules dans les alentours de la pointe de polymère. (c,d) Des sections le long de la direction y et x sont présentées respectivement dans les panels (c) et (d).

montrées respectivement dans les panels (c) et (d).
Ces sections montrent que seul la direction y de la NPM a subit une élongation, prouvant le fait que c'est le champ proche optique qui a assuré la dose d'énergie nécessaire pour dépasser le seuil. D'où la photopolymérisation a été initiée juste dans cette direction.

6.5.2 Particules colloidales

Pour bien répartir les particules colloïdales et éviter leurs agrégations sur les substrats, nous avons procédé à la fonctionnalisation des lames de verre par l'aminosilane, qui créée un terminus NH_3^+ sur la surface du verre. Cet ion positif est la cause de l'attraction entre les substrats et les colloïdes d'argent chargées néga-

tivement. La figure 6.1 de ce rapport a montrée une image AFM présentant des particules colloïdales bien réparties sur la surface. Ce type d'échantillon a été irradié avec plusieurs doses incidentes afin de quantifier la valeur exacte du facteur d'exaltation des colloïdes. Des images AFM sont prises pour la même zone contenant les même NPM avant et après l'exposition, ce qui signifie que notre approche a été appliquée sur les même nanoparticules.
La dose incidente a été variée entre 5% et 75% de la dose seuil, paramètre qui se détermine en se basant sur la section 2.

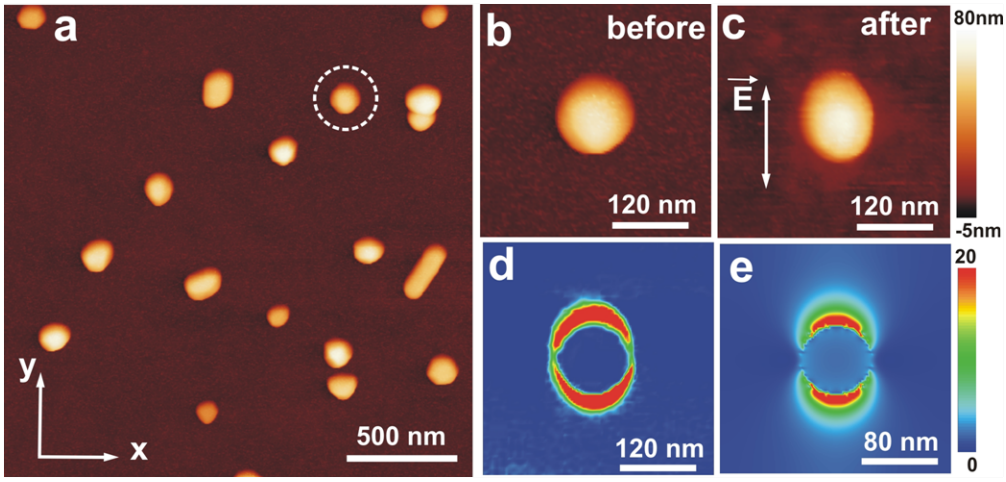

Figure 6.8: Nano Photopolymerization induite par les plasmons de surface localisés de colloides d'argent. (a) Image AFM montrant des colloides avant la procédure. (b) Zoom sur la NPM encerclée. (c) Zoom sur la NPM après la procédure. (d) Image différentielle des figures c et b. d) Intensité du champ proche calculé par FDTD.

Pour chaque valeur de dose, un scan AFM avant est réalisé pour viser une particule ayant une symmétrie sphérique parfaite. Ensuite, une goutte de solution chimique est déposée sur les colloides d'argent suivie d'une irradiation à une dose donnée, bien entendue une dose inférieure à la dose seuil. Enfin l'échantillon est rincé dans un bain d'éthanol et d'isopropanol.
L'échantillon est ensuite scanné et la même particule colloidale est comparée avant et après la procédure complète, afin de déduire la valeur de l'élongation du lobe de polymère dans la direction de la lumière incidente. Cette élongation de la nanoparticule parallèlement à la direction de la polarisation du champ incident est en fait due à l'intensité locale du profile dipolaire du champ proche optique de la NPM, qui dépasse la dose seuil localement et induit une photopolymérisation à l'échelle nanométrique. Ceci veut dire que dans le cas où la NPM n'exalte pas le champ, les lobes de polymère ne se formeront jamais parce que la dose incidente est inférieur

à la dose seuil. La procédure est détaillée dans la Figure 6.8.

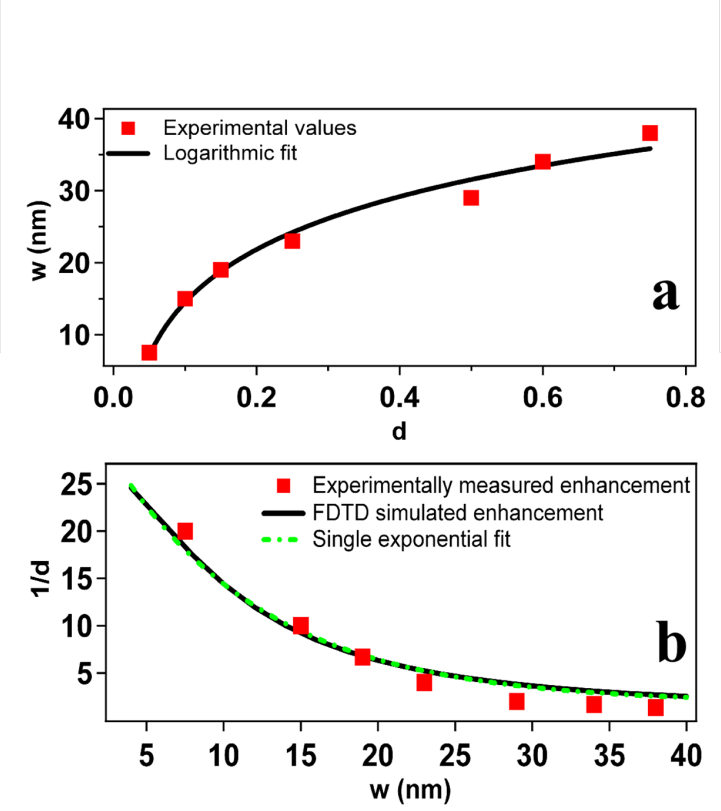

Figure 6.9: Quantification des paramètres physiques reliés aux plasmons de surface localisés. (a) Effect de la dose incidente sur l'élongation du polymère ω: Valeurs expérimentales (rouge) fittées par la fonction $y = 11\ln(39 \times d)$. (b) Valeurs expérimentales (rouge) du facteur d'exaltation des NPM tracées en fonction de l'élongation du polymère mesurée par AFM. Tracé noire correspond à la simulation, faite par FDTD, de l'exaltation et tracé verte est une fonction exponentielle de fit.

- Détermination du facteur d'exaltation et de la profondeur de champ des NPM

Figure 6.9 représente le résultat de l'étude en fonction de la dose incidente. Figure 6.9 (a) montre les valeurs expérimentales de l'élongation du polymère w, points en rouge, qui a été réticulé lors de la procédure et ensuite mesuré par AFM, en fonction de la dose normalisé d, ratio entre la dose incidente et la dose seuil

(D_0/D_{th}). Chaque point corresponds à la moyenne de trois valeurs prises sur trois nanoparticules différentes. Le graphic montre une augmentation monotone, suivant une logarithm, de w en fonction de d. On verra dans la suite que cette fonction logarithmique est la signature de la nature évanescente du champ proche optique des NPM.
Le résultat de la Figure 6.9 (a) peut être expliqué de la façon suivante, en considérant la décroissance du champ évanescent diffusé par la nanoparticule. La dose locale D engendrée par la nanoparticule métallique dans la direction y peut être exprimée par l'Eq. 6.2:

$$D = F_{max} D_0 exp(-\alpha y) \tag{6.2}$$

où F_{max} représente le maximum de l'intensité du facteur d'exaltation relié à la résonance plasmon de surface, α représente la distance de pénétration au bout de laquelle la valeur de l'intensité du champ vaut 1/e de sa valeur maximale et y est la distance de la NPM. α^{-1} est l'extension spatiale de l'intensité du champ proche optique.
Comme nous l'avons mentionné, la photopolymérisation est initiée quand D $\geq D_{th}$; En appliquant cette condition à l'Eq. 6.2, nous obtenons:

$$\exp(-\alpha y) \geq \frac{D_{th}}{F_{max} D_0} \tag{6.3}$$

Eq. 6.3 peut être réduite pour obtenir les positions auxquelles la polymérisation prend place, données par l'Eq 6.4:

$$y < y_{max} = -\alpha^{-1} \ln(\frac{D_{th}}{F_{max} \times D_0}) \tag{6.4}$$

En remplaçant D_0/D_{th} par la dose normalisée d, l'Eq. 6.4 pourrait être écrite comme:

$$y_{max} = \alpha^{-1} \ln(F_{max} \times d) \tag{6.5}$$

y_{max} est en fait l'élongation du polymère w mesurée par AFM et qui pourrait être représentée par $w = \alpha^{-1} \ln(F_{max} \times d)$. Ceci dit, nos valeurs expérimentales pourraient être fittées par la fonction logarithmique suivante:

$$y = \alpha^{-1} \ln(F_{max} \times x) \tag{6.6}$$

En fittant nos valeurs par l'Eq. 6.6, nous obtenons la tracée noire dans la Figure 6.9 (a) avec 39 et 11 nm comme valeurs de fit. ces valeurs correspondent à F_{max} et α^{-1}, respectivement.

Les résultats de la Figure 6.9 (a) pourraient être traités d'une façon differente

afin d'obtenir la variation de la valeur du facteur d'exaltation en fonction de la distance. Figure 6.9 (b) montre 1/d en fonction de w. Les points en rouge ressemblent une décroissance exponentielle qui reflète la distribution de l'intensité du champ proche optique des plasmons. Les datas expérimentales sont en très bon accord avec le calcul FDTD représenté par la courbe noire. Ce calcul a été fitté par une fonction exponentielle, montrée par la courbe verte, et les paramètres de fit de F_{max} et α^{-1} étaient 34 et 10 nm respectivement [19].

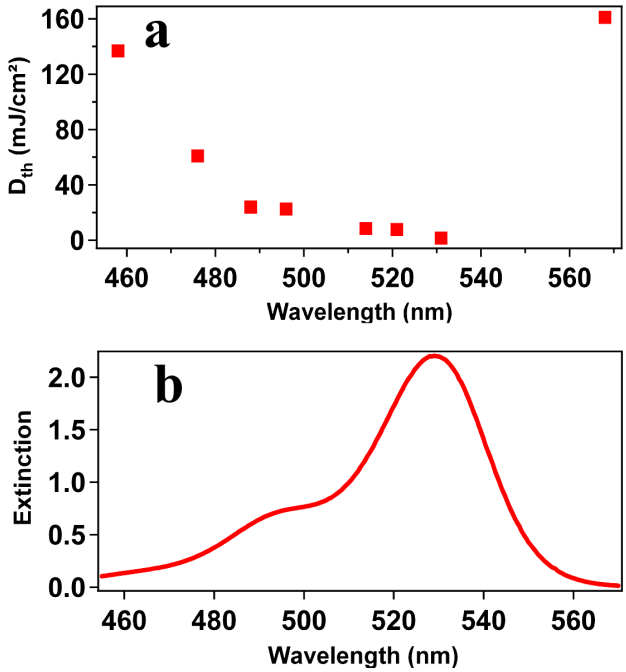

Figure 6.10: Réponse spectrale du système photochimique caractérisée en champ lointain. (a) Variation de D_{th} en fonction de la longueur d'onde incidente. (b) Spectre d'absorption de l'Eosine-Y dans le système photochimique.

Cet excellent accord entre les résultats expérimentales et le calcul FDTD soutient fermement que notre approche est capable de donner un profil quantitatif du champ proche optique d'une nanoparticule métallique unique, avec une précision nanométrique. De plus et au meilleur de notre connaissance, cette valeur de la profondeur du champ évanescent constitue la première mesure effectuée directement dans le champ proche.

- Spectre de diffusion de NPM unique en champ proche

En raison de la nature dispersive de la réponse plasmons, F_{max} est une fonction

de λ et donc la nanophotopolymérisation devrait refléter la dépendance spectrale des plasmons de surface localisés [19]. Contrairement à l'approche traditionnelle de la spectroscopie en champ lointain [13], notre approche fournit pour la première fois l'occasion d'étudier cette relation de dispersion directement dans le champ proche.

Pour illustrer cette capacité, nous avons utilisé les huit longueurs d'onde disponibles du laser Ar:Kr. La réponse spectrale du système photochimique, à savoir la fonction $D_{th}(\lambda)$, est caractérisée en champ lointain pour aboutir à la valeur de D_{th}. Figure 6.10 (a) montre la fonction mesurée D_{th} en fonction de la longueur d'onde incidente. Un minimum est clairement observée quand λ est égale à 530 nm. Ce minimum correspond au maximum du spectre d'absorption (530 nm) de l'Eosine-Y utilisé comme colorant (Figure 6.10 (b)). La connaissance de la valeur de D_{th} pour chaque λ nous permet d'établir la dose normalisée d à une valeur constante.

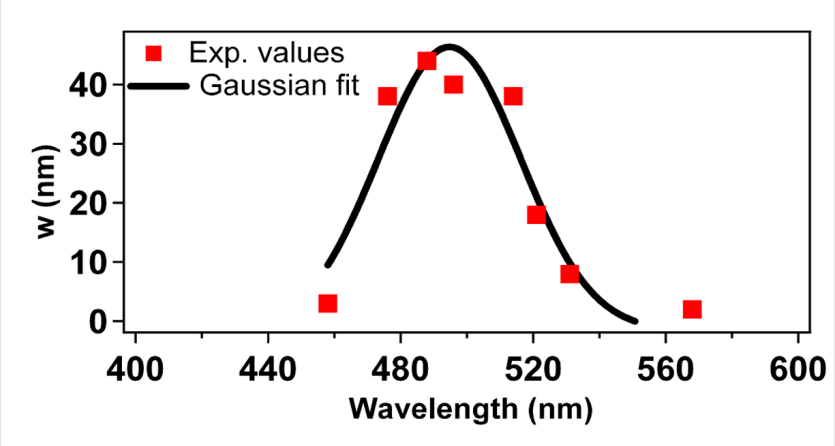

Figure 6.11: Spectre en champ proche d'une NPM unique: Effet de la longueur d'onde incidente sur l'élongation des lobes de polymère (points rouges) fitté par une fonction gaussienne (courbe noire).

Figure 6.11 montre w, lié à F_{max}, en fonction de la longueur d'onde pour une valeur constante de d, 0.75. Içi, on néglige l'influence des effets photochimiques (en particulier la diffusion de l'oxygène et du colorant) en les considérant comme des paramètres constants. Le spectre de la Figure 6.11 reflète la réponse spectrale en champ proche des NPM. Un comportement clair de résonance est observé et est attribué à la signature spectrale du mode plasmons de surface, avec un maximum à 494 nm (courbe noire). Notre approche de caractérisation est puissant parce qu'il fournit, d'une manière simple, le spectre en champ proche d'une NPM

unique ayant des informations uniques non accessibles par des mesures en champ lointain.

En conclusion, nous avons présenté dans ce rapport une approche d'interaction "métal / polymère" à l'échelle nanométrique et avons démontré notre capacité à lancer un processus photochimique à des régions précises, où un facteur d'exaltation est prévu. newline Dans un premier temps, les procédures de fabrication et de caractérisation des nanoparticules métalliques ont été discutées. Ensuite, la composition et les méthodes de caractérisation, en se basant sur le nouveau montage expérimental, de la solution photopolymérisable ont été montrées. L'approche, qui nous a permis de caractériser quantitativement le champ optique évanescent des NPM et de cartographier son profil, a été aussi détaillée.

A juste titre d'exemple, nous montrons aussi un des résultats d'une expérience menée sur des nanorods d'Or irradiés hors leur résonance, et qui avait comme but d'imager le profil du champ électrique non-résonant à l'interface métal / diélectrique. La Figure 6.12 montre l'imagerie à l'échelle nanométrique de ce type de champ électrique.

6.6 Conclusions et perspectives

Dans ce travail de thèse, nous avons mis en oeuvre une approche pour une caractérisation fiable et quantitative des champs proches de structures plasmoniques et pour la compréhension des processus physico-chimiques qui régissent la nanofabrication.

Les premières études dans ce domaine ont examiné l'interaction entre les structures métalliques et les molécules photosensibles et ont prouvé la possibilité de déclencher une photopolymérisation à l'échelle nanométrique, par le biais des plasmons de surface de ces nanoparticules. Il a été également montré que l'approche nanophotopolymérisation constitue une technique puissante pour l'imagerie du champ proche de structures métalliques et évite ainsi la perturbation de la physique de l'échantillon en apportant une sonde à proximité. Il convient de noter que cette approche de photopolymérisation à l'échelle nanométrique repose sur la réponse non-linéaire de la formulation photosensible.

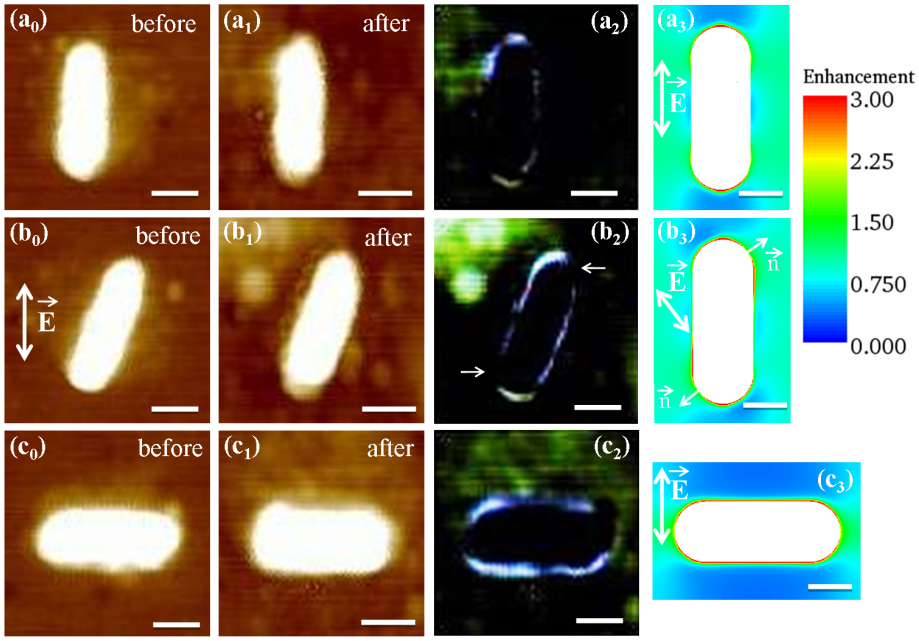

Figure 6.12: Soulignant l'élongation des axes majeurs et mineurs du nanorod. Les trois lignes de cette figure présentent trois nanorods orientés différemment par rapport à la polarisation incidente; ligne 1, 2 et 3 correspond à une orientation du nanorod de 0°, 22.5° et 90°, respectivement. La première colonne de cette figure montre l'image AFM du nanorod d'Or avant que la procédure alors que la deuxième colonne correspond aux images AFM après la procédure. La troisième colonne illustre la différence des images qui correspondent à la soustraction entre la première et la deuxième colonne. La polarisation du champ incident est représentée par la flèche blanche établie dans le panel de (b_0) et les barres d'erreur correspondent à une distance de 90 nm.

Au cours de cette thèse, nous avons tenté d'être beaucoup plus quantitative par rapport aux travaux antérieurs dans le domaine de l'imagerie en champ proche.

En irradiant les nanoparticules de métal à leur résonance, nous avons été capables de mouler le profil dipolaire du champ électromagnétique confiné par un polymère photo-actif, avec une résolution supérieure à 10 nm. Ensuite et par une caractérisation précise des moules polymères par AFM, nous avons été capables d'extraire des valeurs précises du facteur d'exaltation et de la profondeur du champ proche de nanoparticules colloïdales d'argent, qui ont été en accord avec

les simulations électrodynamique. En outre, nous avons montré notre capacité à avoir la signature spectrale de la résonance de plasmon de surface localisés d'une nanoparticule métallique unique directement en champ proche.
Ces résultats ont démontré une caractérisation quantitative, jusqu'à l'échelle du nanomètre, des champs électromagnétiques évanescents confinés qui sont indispensable pour développer des applications photoniques.

En outre, nous avons appliqué notre photopolymérisation en champ proche sur des nanorods d'or enrobés dans une solution photopolymérisable. Une fois de plus, et en éclairant ces particules d'or hors leur résonance, nous avons pu directement imager le profil du champ non-résonnant à l'interface métal / diélectrique. En fait, nous avons prouvé que la sensibilité du photopolymère est suffisamment élevée pour imprimer le champ électrique non-résonnant, permettant ainsi une visualisation directe de la distribution de densité de charge de surface avec une résolution nanométrique, 2-nm.

Notre approche en champ proche nous a aussi donné l'occasion de mettre en évidence certains phénomènes disponible uniquement à l'échelle nanométrique, à savoir la diffusion du colorant. En vérité et en observant l'étendue spatiale de la réaction de polymérisation dans des conditions d'éclairage différentes, il a été possible d'explorer les processus physico-chimiques qui régissent la nanofabrication.

Nous croyons que notre travail est d'intérêt général pour la communauté des nanosciences, en particulier pour les lecteurs dans les domaines de la plasmonique, optique en champ proche, la nanophotonique, et photochimie moléculaire. Il y a un grand potentiel pour les futurs chercheurs à utiliser les lignes directrices fondamentales développées dans cette thèse afin de concevoir et d'optimiser les nanosystèmes hybrides. Plusieurs points de vue émanant des travaux actuels et visent à comprendre la matière à l'échelle nanométrique.

En fait, nous avons récemment commencé à utiliser les nanoparticules métalliques à formes complexes, nommément nanotriangles, afin d'initier la photopolymérisation à leurs sommets. Cela nous permettra d'étudier "l'effet de pointe" qui vient de singularités géométriques ou à proximité d'une protrusion nette sur une surface métallique, où le champ électrique atteint des valeurs de haute intensité. En outre, en créant ce point polymère à l'un des sommets du triangle, sa symétrie sera brisée, et donc nous pouvons étudier les propriétés non-linéaires du

nouveau système hybride.

Nous avons également entrepris des travaux sur la variation de l'indice de réfraction de la formulation photopolymérisable, par dopage avec des matériaux luminescents, comme chromophores, des boîtes quantiques semi-conducteurs, les nanoparticules métalliques, les molécules de cristaux liquides, etc. Cette expérience va finalement engendrer deux lobes de polymère, dirigé suivant la direction de la polarisation incidente, où les molécules actives seront emprisonnés. En fait, il serait intéressant de mener une étude sur le couplage entre nanoparticules métalliques et molécules emprisonnées dans la matrice polymère, par des moyens conventionnels de spectroscopie ou par technique de spectroscopie ultrarapide.

En outre, nous pouvons étudier la propagation plasmonique en utilisant notre approche de photopolymérisation en champ proche. En faisant une chaîne de nanorods métalliques et éclairant une extrémité de ce réseau linéaire, nous allons générer des ondes de plasmons de surface délocalisés qui vont déclencher le processus chimique et, par la suite, imprimer le profil de cette onde. Ensuite et par une caractérisation précise du moule de polymère, on peut déterminer des paramètres importants liés à la propagation de ce type de plasmons de surface.